Université de Strasbourg I - Louis Pasteur
U.F.R. DE PHYSIQUE

Thèse

présentée par

Pascale Mayet

pour obtenir

Le GRADE de DOCTEUR EN SCIENCES
DE L'UNIVERSITE LOUIS PASTEUR DE STRASBOURG

Sujet :

Isomers populated by projectile fragmentation in the neutron-rich A=180-200 mass region

Soutenue le 16 novembre 2001 devant la commission d'examen :

M. Jerzy Dudek	Président
	Rapporteur interne
M. Geirr Sletten	Rapporteur externe
M. Laurent Tassan-Got	Rapporteur externe
M. Jacques Martino	
M. Jürgen Gerl	Co-directeur de thèse
M. Jean-Pierre Vivien	Directeur de thèse

Institut de Recherches Subatomiques
Unité Mixte de Recherches CNRS-IN2P3 et Université Louis Pasteur

A la mémoire de ma grand-mère Lucie

Fiat lux... (Vulgate, Genèse, Chapitre I, 3)

Remerciements

C'est à moi que revient à présent la lourde tâche d'écrire les remerciements. Voilà qui est fait. J'espère que mes collègues ne me tiendront pas rigueur de les avoir écrits dans ma langue maternelle.

Une thèse ne serait pas ce qu'elle est sans ce paragraphe, si anodin et pourtant si essentiel - il paraîtrait même que certains ne lisent que cela! Que ceux dont j'aurai, bien malgré moi, oublié de mentionner le nom veuillent bien me pardonner.

Avant toute chose, merci aux membres du jury pour l'intérêt qu'ils ont porté à mon travail. Je sais gré à Messieurs Geirr Sletten, Laurent Tassan-Got et Jerzy Dudek de m'avoir fait part de leurs commentaires et j'espère avoir répondu à leurs attentes. Je suis également infiniment reconnaissante à M. Jacques Martino d'avoir accepté de faire partie de mon jury.

Je n'aurais jamais obtenu le grade de docteur si Jean-Pierre Vivien n'avait pas accepté d'encadrer, au nom de l'Institut de Recherches Subatomiques, mon travail de thèse. Je lui en suis d'autant plus redevable que sa tâche n'a pas dû être facilitée par la distance qui nous séparait.

En effet, cette thèse s'est déroulée au GSI à Darmstadt. Je voudrais donc également remercier le GSI et, en particulier, le groupe de spectroscopie γ pour leur accueil durant ces trois années de labeur et, en premier lieu, je remercie Gottfried Münzenberg et Jürgen Gerl pour la confiance qu'ils m'ont toujours témoignée tout au long de ce travail.

Quand il est question d'accueil, je ne peux bien évidemment pas oublier de mentionner le personnel administratif qui facilite grandement l'intégration des pauvres étrangers dont je fais partie. Je pense tout particulièrement à Siggi Raiss qui a toujours fait preuve d'une grande disponibilité à mon égard.

La qualité d'une thèse relève également en grande partie de la bonne entente entre les membres d'un groupe. Ainsi je salue toutes les personnes qui font ou ont fait, à un moment ou à un autre, partie de ce groupe. Je pense, en particulier à Magda Górska, Matthias Kaspar (merci pour la compréhension des fichiers LMD), Ivan Kojouharov, Yuri Kopatch (merci de m'avoir aidée avec PAW), Samit Mandal (nous sommes passés par les mêmes difficultés...), Maurycy Rejmund (merci pour m'avoir initiée aux joies de l'électronique!), Henning Schaffner (merci pour m'avoir guidée dans le dépouillement des fichiers LMD), Christian Schlegel, Shuying Wan, Hans-Jürgen Wollersheim, sans l'aide desquels ce travail aurait sans doute été pénible. Mais aussi, je salue Armin Kleinböhl et Ingo Peter et je souhaite bonne chance à Adriana Banu et Radomira Lozeva pour leurs thèses respectives.

D'autres encore ont contribué en très grande partie à la réussite de cette thèse et je leur en suis infiniment reconnaissante. Il s'agit de Maggie Hellström (souvent dure mais toujours juste!), Marek Pfützner, Fanny Rejmund, Jose Benlliure (alias Pepe), Dolores Cortina-Gil

(alias Lola), Enrique Casajeros (dit Kike), Arnd Junghans (sans eux, jamais je n'aurais aussi bien compris le fonctionnement du FRS et le mécanisme de production des fragments), Renée Lucas et Janine Genevey (sans qui je n'aurais peut-être jamais vu de décroissances γ!). Je remercie également Paddy Regan et Zsolt Podolyák de m'avoir laissé l'opportunité d'analyser ces données et Phil Walker pour son aide bienveillante dans l'élaboration des schémas de décroissance.

Bien sûr, mes remerciements se dirigent également vers toutes les personnes sans qui l'expérience, dont ce travail est issu, n'aurait pas été possible. En particulier, je pense à l'équipe de maintenance du FRS (Adolf Brünle, Karl-Heinz Behr, Karlheinz Burkard pour leur appui technique et logistique) et à tous ceux qui ont participé à la production du faisceau et aux réglages du FRS.

En dehors du travail, il y a la vie quotidienne. Cette vie quotidienne qui peut s'avérer très difficile quand on est dans un pays étranger dont on connaît mal la langue et les habitudes. Heureusement, l'avantage de travailler dans un laboratoire international comme le GSI, c'est qu'on est rarement seul pour faire face à ces petites contrariétés. Ainsi je remercie tous mes amis et collègues du GSI et d'ailleurs pour m'avoir nourrie, aidée, consolée, secouée, soutenue, motivée, secourue. En bref, pour ne m'avoir jamais fait défaut! Merci à vous. Je pense en particulier à la sainte trinité algérienne des trois F (Farouk, Faïrouz, Faouzi), Carole (ma grande sœur), Ketel (mon ange-gardien depuis Strasbourg!), Frédéric (nous partageons bien plus qu'un patron!), Christian, Michael, Paulo, Ushasi, Aradhana, Kate, Samira, Olivier, Jason, Milou, Medhi, Beatriz, Valentina, Kerttuli, Chiara, Cristina, Ruxandra, Sacha, Lena, Sigurd, Carola et les autres. Je vous ai, pour la plupart, connus au GSI et je souhaite que notre amitié se prolonge encore longtemps et au-delà des frontières...

Je voudrais encore dire un mot sur des personnes qu'on oublie un peu trop facilement dans les remerciements : il s'agit des enseignants. Ce sont eux qui, les premiers - mais ils ne sont pas les seuls - , éveillent notre esprit critique et notre goût pour la recherche. Je les salue donc tous ici.

Enfin - last but not least! - les mots me manquent pour exprimer mon amour et ma gratitude envers ma famille. De mes parents, j'ai appris qu'il ne fallait jamais perdre courage : qu'ils sachent qu'ils ont toujours été des modèles pour moi, eux qui ont traversé les difficultés sans jamais se laisser abattre. De ma grand-mère, je tiens une volonté de fer sans laquelle ce travail n'existerait pas (c'est à sa mémoire que cette thèse est dédiée). Quant à mon grand-père, il m'a enseigné que la connaissance est la seule richesse. Tous, je les remercie aujourd'hui de m'avoir permis de réaliser mon rêve d'enfant : être chercheur.

Contents

List of Figures

List of Tables

Introduction (English)

Up to now, experimental nuclear studies have mainly focused on nuclei either in the valley of stability or near it because both beams and targets used in accelerators are most of the time composed of stable nuclei. The nuclei produced in reactions are therefore produced near stability or at the neutron-deficient side of the valley depending on the employed nuclear reaction. Consequently, there is still a large "terra incognita" of nuclei, especially on the neutron-rich side of the stability line, where nothing is known. The location of the neutron drip line itself is even not well known. Access to this region is of extreme importance since new behaviour is expected in nuclei with highly asymmetric N/Z ratios and in weakly bound nuclei near the drip line.

However it is not necessary to go very far away from stability to obtain new information, especially on the neutron-rich side. Actually, in many mass regions, even the first unstable neutron-rich nuclei remain more or less unknown. The neutron-rich region from Er to Hg is very illustrative for these difficulties. Let us mention three basic quantities of even-even nuclei, namely the energy of the first excited 2^+ state E_{2+}, the ratio $R = E_{2+}/E_{4+}$ and the $B(E2)$ values. If these quantities are systematically known for stable nuclei and exhaustively measured on the proton-rich side, there is, however, no nucleus beyond the stability line on the neutron-rich side where all three quantities have been measured [1]. Hence, even modest forays into the neutron rich side of stability would produce new information on the evolution of structure.

Access to these nuclei is now possible thanks to the development of new techniques to produce and accelerate beams of unstable nuclei on one hand and to the advances of detector performance on the other. Radioactive nuclear beams are now produced successfully but they are several orders of magnitude weaker than beams of stable nuclei. Therefore, to take advantage of these recent developments, considerable efforts have been accomplished to improve the efficiency and resolution of the instruments used in experiments.

The work presented here reports on the results of an experiment done at GSI in 1999.

This experiment combined the use of radioactive nuclear beams produced by fragmentation to very selective and efficient instruments employed for the separation and structure analysis of selected nuclei. The goal of this experiment was to get as much information as possible on the nuclear structure of nuclei in the nearly unknown A$\sim$180-200 neutron-rich mass region. To this purpose, a selective spectrometer was used to separate radioactive nuclear beams and, with the association of high purity segmented γ-ray Ge detectors, the nuclear structure of these beams was studied. In the first chapter, we come back to the reasons which have motivated this experiment and to the nuclear models describing the structure of the atomic nucleus in this region. We also discuss the various experimental techniques which can be used to populate nuclei in this region. The second chapter presents in more details the reaction mechanism used for the production of the nuclei of interest and the techniques employed to perform the experiment. The third chapter deals with the method developed for the analysis of results while in the last chapter the results are exposed and interpreted in the light of the existing knowledge in this region.

Introduction (Français)

Jusqu'à présent, les études en structure nucléaire expérimentale se sont focalisées sur les noyaux proches de la vallée de stabilité car les faisceaux et les cibles utilisés dans les accélérateurs sont la plupart du temps composés de noyaux stables. Ainsi les noyaux produits lors des réactions nucléaires se situent près de la stabilité ou du côté déficient en neutrons selon la réaction employée. En conséquence, le côté riche en neutrons de la vallée de stabilité constitue toujours une "terra incognita" dont on ignore presque tout. La limite d'existence des noyaux riches en neutrons (drip line) est elle-même incertaine. L'accès à cette région est donc d'une extrême importance puisqu'on s'attend à observer de nouveaux comportements dans les noyaux dont le rapport N/Z est très asymétrique ainsi que dans les noyaux peu liés proches de la drip line.

Pourtant il n'est pas nécessaire de s'éloigner beaucoup de la stabilité pour obtenir des informations nouvelles, en particulier pour les noyaux riches en neutrons. En effet, dans de nombreuses régions, même les premiers noyaux riches en neutrons instables nous restent inconnus. La région riche en neutrons s'étendant de l'erbium au mercure illustre parfaitement ce problème. Mentionnons trois quantités de base mesurées pour les noyaux pairs-pairs, à savoir E_{2+} l'énergie du premier état excité 2^+, le rapport $R = E_{2+}/E_{4+}$ et les valeurs de B(E2). Si ces quantités sont systématiquement connues pour les noyaux stables et exhaustivement mesurées pour les noyaux riches en protons, il n'y a en revanche aucun noyau riche en neutrons au-delà de la ligne de stabilité pour lequel ces trois quantités sont connues. Ainsi, même de modestes recherches dans les noyaux riches en neutrons produiraient de nouvelles informations sur l'évolution de la structure nucléaire dans ces noyaux.

Accéder à ces noyaux est devenu possible grâce au développement de nouvelles techniques pour produire et accélérer des faisceaux de noyaux instables, d'une part, et grâce aux avancées effectuées quant aux performances des détecteurs, d'autre part. Les faisceaux radioactifs sont désormais produits avec succès mais les intensités obtenues sont de beaucoup inférieures à celles des faisceaux stables. C'est pourquoi, pour profiter de ces récents développements,

des efforts considérables ont été accomplis afin d'améliorer l'efficacité et la résolution des instruments de détection utilisés dans les expériences.

Le travail présenté ici relate les résultats d'une expérience réalisée au GSI en 1999. Cette expérience associait l'utilisation de faisceaux radioactifs produits par fragmentation à des instruments de détection sélectifs et efficaces pour la séparation et l'analyse de la structure nucléaire des noyaux sélectionnés. Le but de cette expérience consistait à obtenir autant d'informations que possible sur la structure nucléaire des noyaux riches en neutrons de masse A$\sim$180-200. A cette fin, un spectromètre d'une grande sélectivité a été utilisé pour séparer les faisceaux radioactifs produits et, grâce à l'association de détecteurs germanium segmentés d'une grande pureté, la structure nucléaire de ces noyaux a pu être étudiée. Dans le premier chapitre, nous revenons sur les raisons qui ont motivé cette expérience et sur les modèles nucléaires décrivant la structure du noyau atomique dans cette région. Nous discutons également les différentes techniques expérimentales qui peuvent être envisagées afin de peupler les noyaux de cette région de masse. Le deuxième chapitre présente en détails le mécanisme de réaction utilisé pour produire les noyaux souhaités et les techniques employées pour réaliser l'expérience. Le troisième chapitre est consacré à la méthode développée pour l'analyse des données tandis que, dans le dernier chapitre, les résultats sont exposés et interprétés à la lumière des connaissances actuelles sur la région considérée.

1 Motivations

Since the discovery of radioactivity a century ago, nuclear physicists have been trying to probe the structure of the atomic nucleus.

With the developments of instruments, the structure of nuclei with highly asymmetric N/Z ratios has been successfully studied, especially on the proton-rich side of the valley of stability up to the dripline. The number of protons and neutrons the nuclei are composed of is restricted by the binding energy B of the nucleons. The existence of nuclei is therefore limited by the driplines on each side of the valley of stability (on the proton-rich side where B_p=0 and on the neutron-rich side where B_n=0). However, the chart of nuclides (see Fig. 1.1) gives evidence of the difficulty to reach the neutron-rich side of the valley of stability and therefore the behaviour of such nuclei is still not well understood. New techniques have been recently used to produce successfully neutron-rich nuclei and to access the structure of these exotic nuclear species.

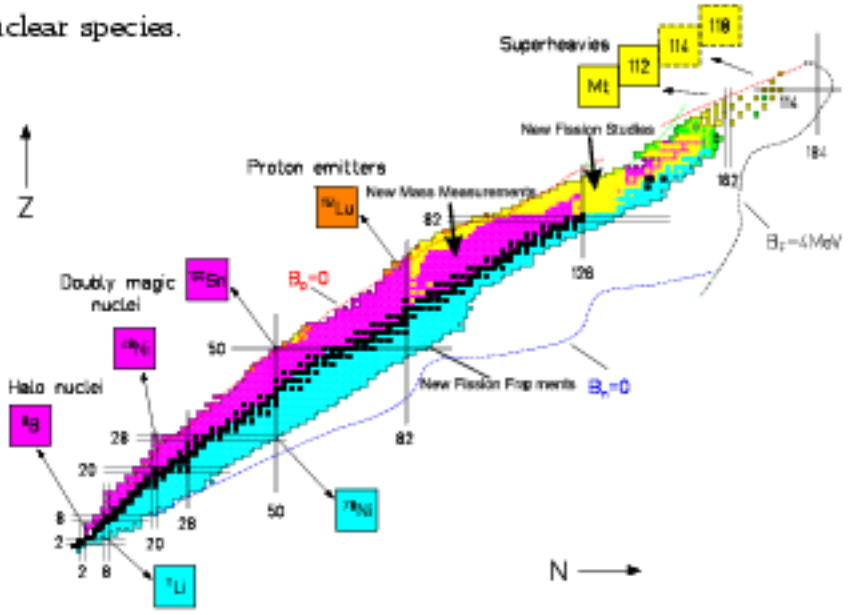

Figure 1.1: The chart of nuclides. The black squares represent the stable nuclei, the blue squares the neutron-rich nuclei and the red squares the proton-rich nuclei. The blue and red dashed lines indicate the neutron and proton driplines respectively.

Over the last century, different models have been developed to describe with more or less success the structure of nuclei. Two main kinds of models have been applied to figure out what the structure of the atomic nucleus is: microscopic models whose most popular example is the shell model and phenomenological models of which the Nilsson model is an example. The nuclear shell model is used with great success to describe the spherical nuclei at or near the shell closure (the so called magic numbers 8, 20, 28, 50, 82, 126) while collective models have been successfully developed to explain very well deformed nuclei properties away from these closed shells. Microscopic models based on selfconsistent methods such as Hartree-Fock or relativistic mean field methods are also used to treat the various observed properties of nuclei in a unified way, independently from the numbers of protons and neutrons.

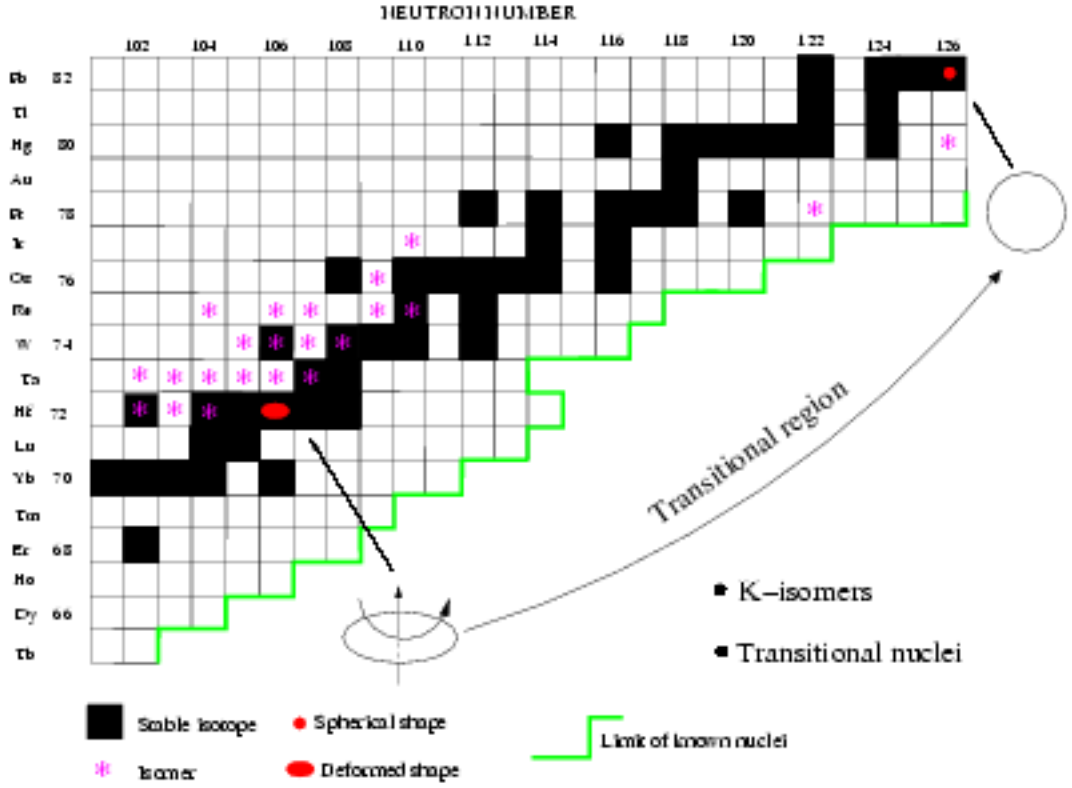

Figure 1.2: Nuclear chart of the A∼180-200 region.

1.1 Transitional nuclei

The A$\sim$190 nuclei are of particular interest since they span a gradual and complex transition region between the well deformed rare earth nuclei like ^{180}Hf and the spherical lead region, ^{208}Pb being the heaviest doubly magic nucleus known so far. This transitional region extends from the W isotopes, which have well-developed quadrupole deformation but also strong hexadecapole distortions and some degree of axial asymmetry, through the less deformed and more asymmetric Os isotopes to the weakly deformed and γ unstable Pt nuclei (see Fig. 1.2).

Below, we will come back to the various historical models used to treat the structure of such nuclei.

1.1.1 Collective models

Collective models are used to describe the behaviour of the atomic nucleus far from the shell closures and are briefly described in the following.

When the numbers of protons and neutrons are far away from the shell closure number, it becomes extremely difficult to treat the atomic nucleus in the shell model framework. A new framework has to be considered which takes into account the collective behavior of the nucleus. In this model, the nucleus is considered like a charged liquid drop whose motion may produce surface oscillations around the spherical equilibrium shape or may rotate if the nucleus is deformed in its ground state.

- Shape parameters of a liquid drop

Considering deformations from the spherical shape, one can express the radius of the nucleus R as a function of the radial coordinates θ and ϕ and develop it in terms of spherical harmonics $Y_{\lambda\mu}(\theta,\phi)$:

$$R = R(\theta,\phi) = R_0 C(\alpha_{\lambda\mu})(1 + \sum_{\lambda=1}^{\infty} \sum_{\mu=-\lambda}^{\lambda} \alpha^*_{\lambda\mu} Y_{\lambda\mu}(\theta,\phi))$$

where R_0 is the radius of the sphere. If we assume the nuclear fluid to be incompressible, we require to keep the volume V of the nucleus constant for all deformations as :

$$V = \frac{4}{3}\pi R_0^3.$$

This defines the constant $C(\alpha_{\lambda\mu})$.

The $\alpha_{\lambda\mu}$ parameters are not completely free. Reflection symmetry requires that $\alpha_{\lambda\mu} = \alpha_{\lambda-\mu}$. The terms with λ=1 correspond to a net displacement of the center of mass and do not result from the action of internal nuclear forces. The development in spherical harmonics generally starts with the quadrupole deformation λ=2, higher order terms λ=3 and λ=4 corresponding to octupole respectively to hexadecapole deformation.

Two kinds of extreme behaviours can occur :

- the nucleus vibrates around its spherical shape. The motion of vibration is described by the coefficients $\alpha_{\lambda\mu}$ as a function of time. In this case, the choice of the axes of the system is not important : since the shape of the nucleus comes back periodically to its spherical shape, no orientation is privileged.

- the nucleus has a constant deformation and rotates collectively around a defined axis. If we choose the system of axes as the principal axes of the mass distribution and if we define the orientation of the nucleus with the help of the three Euler angles, the system deformation is defined explicitly and the equations of motion contain only the rotational motion.

In the case of quadrupole deformations (λ=2), due to nucleus symmetry, the five coefficients $\alpha_{2\mu}$ reduce to two real independent variables α_{20} and $\alpha_{22} = \alpha_{2-2}$ ($\alpha_{21} = \alpha_{2-1} = 0$). Together with the three Euler angles, these coefficients give a complete description of the system. It is convenient here, following reference [2] to introduce two parameters β and γ through the relation :

$$\alpha_{20} = \beta cos\gamma$$

$$\alpha_{22} = \frac{1}{\sqrt{2}}\beta sin\gamma,$$

β being the deformation parameter and γ the deviation of the shape of the nucleus from axial symmetry.

• Symmetric rotor model

If we now consider that the nucleus has a symmetry axis and rotates around an axis perpendicular to the symmetry axis, the asymmetry parameter γ and all the deformation parameters with $\mu \neq 0$ vanish and the parameters $\alpha_{\lambda 0}$ are called β_λ. The spherical harmonics $Y_{\lambda 0}(\theta,\phi)$ then reduce to Legendre polynomials $P_\lambda(cos\theta)$ and the vector radius $R(\theta,\phi)$ can

be developed in terms of these polynomials :

$$R(\theta,\phi) = R_0 C(\alpha_{\lambda\mu}) \left[1 + \sqrt{\frac{2\lambda+1}{4\pi}} \sum_{\lambda=2}^{\infty} \beta_\lambda P_\lambda(cos\theta) \right].$$

The rotational angular momentum $\vec{R}$ is generated by the collective motion of nucleons about the rotation axis. Additional angular momentum can be generated by the intrinsic angular momentum $\vec{J}$ of any nucleons. The total angular momentum $\vec{I}$ of the nucleus is then:

$$\vec{I} = \vec{R} + \vec{J}.$$

This angular momentum coupling scheme is shown in figure 1.3.

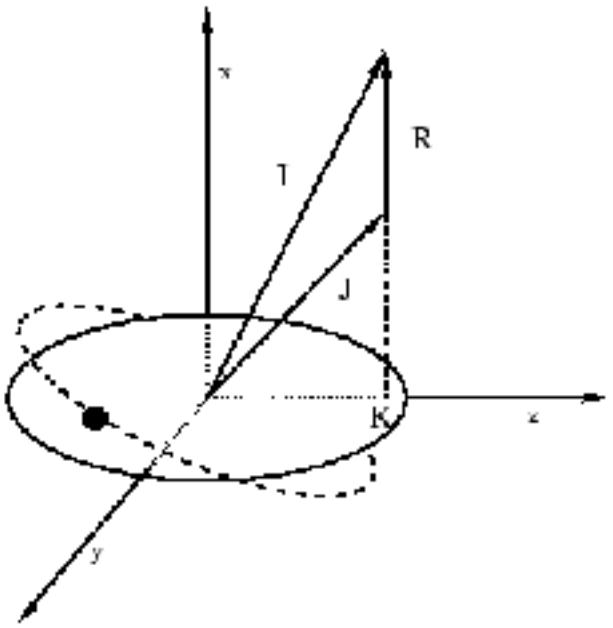

Figure 1.3: Schematic representation of coupling of the collective angular momentum $\vec{R}$ and the intrinsic angular momentum of the nucleons $\vec{J}$. K is the projection of the total angular momentum $\vec{I}$ onto the symmetry axis.

The intrinsic angular momentum of the nucleons $\vec{J}$ is the sum of the angular momenta of the individual nucleons, i.e. $\vec{J} = \sum_{i=1}^{A} \vec{j}_i$. The projection of the total angular momentum onto the symmetry axis is called K and is the same as the projection of $\vec{J}$. The projection of the angular momentum $\vec{j}$ of a valence nucleon is Ω. Thus $K = \sum_{i=1}^{A} \Omega_i$. In the ground-state rotational band of an even-even nucleus, the particles are paired at low spins so that the

intrinsic angular momentum $\vec{J}$ vanishes and the total angular momentum $\vec{I}$ is thus equal to $\vec{R}$.

We know from classical mechanics that the kinetic energy of a rotating object is $\mathcal{J}\omega^2/2$, where $\mathcal{J}$ is the moment of inertia. In quantum mechanics, the rotational Hamiltonian H of a rotating object is :

$$H = \frac{\hbar^2}{2\mathcal{J}}\mathbf{R}^2$$

where $\mathbf{R}$ is the rotational angular momentum operator. If we restrict ourselves to the study of even-even nuclei and if all the angular momentum can be ascribed to rotation, then the total angular momentum $\mathbf{J} = \mathbf{R}$ and we obtain the rotational energy expression :

$$E_{rot}(J) = \frac{\hbar^2}{2\mathcal{J}}J(J+1).$$

• Asymmetric rotor model

In an asymmetric rotor, the shape of the nucleus deviates from axial symmetry and therefore the parameter γ, also called degree of tri-axiality, does not vanish any longer. The rotational levels of asymmetric even nuclei were investigated by A.S. Davydov and G.F. Filippov [3] who proposed a macroscopic model to explain the behaviour of such nuclei. This model assumes that in a first approximation the equilibrium shape of the nucleus can be represented by a triaxial ellipsoid having different elongation along the three principal axes. In this case, the Hamiltonian of an axially asymmetric nucleus is written as :

$$H = \sum_{i=1}^{3} \frac{R_i^2}{2\Theta_i},$$

where R_i $(i = 1, 2, 3)$ are the components of the angular momentum operator of the rotor in the body fixed system and Θ_i are the corresponding moments of inertia obtained by considering the nucleus as irrotational. They are expressed as :

$$\Theta_i = 4B\beta^2 sin^2(\gamma - \frac{2\pi}{3}i),$$

with γ varying between 0 and $\pi/3$ and B is a mass parameter.

In this description, it is considered that rotation of the nucleus takes place without a change of its intrinsic state. Assuming now that the shape of the nucleus may change during rotation, one has to include new parameters to describe the shape modifications. Therefore, a new parameter taking into account the "non-adiabaticity" of the nucleus is included. Finally, one finds that for certain values of K and I, the energy of collective excited states

will be expressed only through two parameters, the "non-axiality" parameter γ and the "non-adiabaticity" parameter μ.

• **The Nilsson model**

As previously mentioned, the spherical shell model provides an excellent description of nuclei near closed shells. However, the existence of deformed nuclei implied the introduction of a model that used a deformed nuclear potential: the modified harmonic oscillator potential, which was first used by Nilsson [4] to investigate the effect of deformation on the single-particle orbits. The Hamiltonian in the case of a modified harmonic-oscillator potential can be written:

$$H_{Nil} = -\frac{\hbar^2}{2m}\nabla^2 + \frac{m}{2}(\omega_x^2 x^2 + \omega_y^2 y^2 + \omega_z^2 z^2) - 2\kappa\hbar\omega_0 \left[\vec{l}\cdot\vec{s} - \mu\left(l^2 - < l^2 >_N\right)\right],$$

where the $(\vec{l}\cdot\vec{s})$ term represents the spin-orbit force, first introduced by Haxel, Jensen and Suess [5] and the term $l^2 - < l^2 >_N$ was introduced by Nilsson to simulate the flattening of the nuclear potential at the centre of the nucleus. The factors κ and μ determine the strength of the spin-orbit and l^2 terms, respectively. The $\omega_{x,y,z}$ terms are the one-dimensional oscillator frequencies which can be expressed as functions of the deformation. In the axially-symmetric case:

$$\omega_x^2 = \omega_y^2 = \omega_0^2\left(1 + \frac{2}{3}\epsilon\right), \omega_z^2\left(1 - \frac{4}{3}\epsilon\right),$$

where ϵ is the deformation parameter and ω_0 is the oscillator frequency ($\hbar\omega_0 = 41A^{-1/3}$ MeV) in the spherical potential with $\epsilon = 0$. Using this deformation-dependent Hamiltonian, the single-partice energies can be calculated as a function of ϵ. A plot of single-particle energy against deformation is known as a Nilsson diagram.

The Nilsson orbitals can be characterised by the so-called asymptotic quantum numbers :

$$\Omega^\pi\left[Nn_z\Lambda\right],$$

where N is the principal harmonic oscillator quantum number, Ω is the projection of the single-particle angular momentum onto the symmetry axis z, Λ is the projection of the orbital angular momentum onto the symmetry axis and n_z is the number of oscillator quanta along the symmetry axis. The parity of the state π is determined by $(-1)^N$. The projection of the intrinsic spin of the nucleon onto the symmetry axis is $\Sigma\left(= \pm\frac{1}{2}\right)$, thus we can define $\Omega = \Lambda \pm \frac{1}{2}$. We note also that there is a relation between the permissible values of n_z and Λ

such that their sum must be even if N is even (positive parity) and odd if N is odd (negative parity).

Notion of quasiparticle

In the model considering the nucleus as a liquid drop, the binding energy due to the pairing force (B_p) is accounted for by the following equation:

$$B_p = \left[\frac{(-1)^N + (-1)^Z}{A^{1/2}}\right]\delta$$

where $\delta \approx$12 MeV. Such a pairing force favours even-even nuclei over odd-N and/or odd-Z nuclei. As a result, the binding energy due to the pairing is higher for even-even nuclei making them more stable. Nilsson model calculations treat this pairing effect as a perturbation of the mean field Hamiltonian of the nucleus.

The probability amplitudes for the k^{th} orbital being occupied and unoccupied by a pair of particles are v_k and u_k respectively such that:

$$v_k^2 + u_k^2 = 1.$$

For a nucleus in its ground state pairs of nucleons occupying orbitals close to the unoccupied levels can *scatter* to the "empty" single-particle states. However, when a particle is *excited* to a previously unoccupied single-particle level, the energy ϵ_k is changed because pairs of particles cannot scatter to singly occupied orbitals (this effect is called blocking). The state at the new energy is now called a single quasiparticle state with an energy:

$$E_k = \sqrt{(\epsilon_k - \mu)^2 + \Delta^2}$$

where μ is the Fermi energy lying in the region between the occupied and unoccupied levels. Δ is the pair gap given by:

$$\Delta = G\sum_{k\neq k_j} u_k v_k$$

where k_j represents the indices of the singly occupied orbitals. G is called the monopole pairing strength and is the strength with which a pair of particles, in time reverse orbits, interact.

From the definition of v_k^2, the total number of particle is:

$$n = 2\sum_k v_k^2$$

and the probability of a state being occupied:

$$v_k^2 = \frac{1}{2}\left[1 - \frac{(\epsilon_k - \mu)}{E_k}\right].$$

The last two equations define the Fermi surface μ.

With the work of Ginocchio and Kirson [6] and, simultaneously, of Dieperink, Scholten and Iachello [7] a connection was established between the geometrical models for collective excitations in nuclei and the interacting boson model of Arima and Iachello [8]. Therefore a particular reason for interest in this region stems from the development of the interacting boson model of Arima and Iachello which shows promise of offering a unified description of a broad range of heavy nuclei.

1.1.2 Interacting Boson Model

The interacting boson model originated from early ideas of Feshbach and Iachello [9, 10, 11], who in 1969 described some properties of light nuclei in terms of interacting bosons, and from the work of Jansen, Jolos and Dönau [12], who in 1974 suggested a description of collective quadrupole states in nuclei in terms of the group theoretic language of SU(6).

In its simplest form, the Interacting Boson Model assumes that an even-even nucleus consists of an inert core plus some valence particles. Furthermore, the valence particles, which are those outside the major closed shells at 50, 82, 126, tend to pair together in states with angular momentum L=0 and 2. These pairs are treated as bosons. The pairs with angular momentum L=0 are called s-bosons, those with angular momentum L=2 are called d-bosons. An appropriate formalism to describe the situation is provided by the second quantization technique. One thus introduces boson creation and annihilation operators of multipolarity L and z-component M, $b^\dagger_{L,M}$ and $b_{L,M}$ respectively. Thus the building blocks of this model are :

$$\begin{cases} b^\dagger_{0,0} = s^\dagger,\ b^\dagger_{2,M} = d^\dagger_M\ (M = 0, \pm 1, \pm 2) \\ b_{0,0} = s,\ b_{2,M} = d_M\ (M = 0, \pm 1, \pm 2) \end{cases}$$

The model was further expanded by introducing explicitely unpaired fermions, thus allowing one to treat odd-even [13] and odd-odd nuclei [14, 15]. Hence nuclei with continuous range of properties can be treated by the model. However, three particular limiting cases can be distinguished in the language of group theory. These three limits correspond to specific

nuclear symmetries. Two of them, the harmonic vibrator SU(5) and the symmetric rotor SU(3) have long been known as are nuclei empirically approximating each. The third symmetry, the O(6) limit, was up to now recognized only in ^{196}Pt [16]. This recognition allows a new interpretation of the complex transitional region that does not require to introduce degrees of freedom such as β and γ.

1.1.3 Microscopic models

Whereas the models using mean potentials, such as the Nilsson model, consider as fixed the deformed field in which the nucleons are moving freely, the microscopic approaches, such as Hartree-Fock methods, deduce the mean field from the actual nuclear interaction.

Nowadays the determination of this interaction is of first importance in nuclear structure theory. There exist various phenomenological interactions. The most used interactions are the zero range Skyrme type interaction and the short range Gogny type interaction. Though microscopic methods are known since the 1930's, they have been used only recently since they need powerful computers.

If the understanding of the nuclear structure of very neutron-rich transitional nuclei is of first interest, it represents only part of the interest brought to the A$\sim$180-200 mass region. Indeed, this region is also remarkable for the study of long-lived K-isomers.

1.2 K-isomers

Before going into more details on K-isomers, we briefly review here the definition of an isomer as well as the different kinds of isomers which can be encountered in nature [17].

1.2.1 What is an isomer?

In chemistry, two isomers are composed of the same particles disposed in two different physical configurations. Similarly, a nuclear isomer is composed of the same number of protons and neutrons as the nucleus in its ground-state but the arrangement and properties of nucleons of this metastable excited state may differ considerably from the ground state configuration. Therefore, a nuclear isomer is a quantum state lying at high excitation energy relative to the ground state and whose half-life can be measured. Indeed there is no strict

definition of the minimum half-life an excited state should have in order to qualify as an isomer. Generally speaking, the half-life should be longer than most other excited states. It means that the half-life of an isomeric state is typically longer than one nanosecond.

Various kinds of isomers may occur in nuclei, depending on the structure of the neutron and proton orbits in each nucleus.

1.2.2 What kind of isomers can we encounter in nature?

Nuclear isomers occur under distinct conditions that have been summarized in the following lines.

- Shape isomers

Shape isomers occur when there is a secondary energy minimum at large elongation of the nucleus, the primary minimum corresponding to the ground-state. In this case, it is difficult for the isomer to change its shape to match the states to which it is decaying. Fission isomers in heavy nuclei illustrate this situation. For these isomers, decay back to the ground-state by γ-ray emission even competes with fission into two lighter nuclei.

- Spin isomers

Spin isomers arise from the difficulty in meeting spin selection rules which embody conservation of angular momentum. The decay path to lower energy states requires a large change in nuclear spin and therefore the emission of radiation with high multipole order to match the spin change. The extreme improbability of such a decay is reflected in the half-life of the isomer which might form a "spin trap".

- K-isomers

The third type of isomer, known as the "K-trap" is a kind of spin trap whose existence depends not only on the magnitude of the nuclear spin vector, but also on its orientation. This type of isomers occurs normally in axially symmetric, deformed nuclei that are found well away from the closed shells that favour spherical shapes.

1.2.3 K-isomers in the transitional region

One main interest in the A∼180-200 neutron-rich nuclei region lies in the presence of a large number of K-isomeric states. Actually, the existence of K-isomers with lifetime within the μs range has already been observed in the more stable region (see Fig. 1.2) and is also predicted in the neutron-rich region [18] where the decoupling of nucleons is favoured. The K quantum number is defined as the projection of the total angular momentum of the nucleus on its symmetry axis (see Fig. 1.4). In the ground state band, K is identical to the angular momentum of the ground state whereas it corresponds to the decoupling of pairs of nucleons to form quasi-particles in the case of excited states.

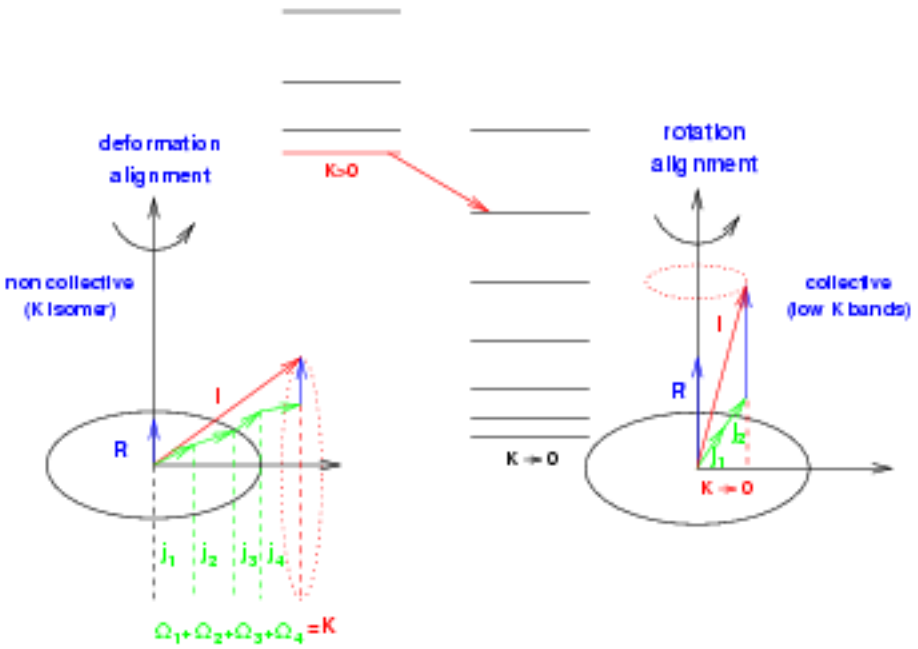

Figure 1.4: Coupling schemes in the particle+rotor model: deformation alignment (strong coupling case), rotational alignement.

Like every quantum number, K is supposed to follow some rules. One of these rules puts conditions on the transition to lower spin states and specifies that the decay to lower lying states is permitted only if :

$$\Delta K \leq \lambda,$$

where λ is the multipolarity of the transition and ΔK the difference in K between two states. Consequently, when ΔK is large, the transition of the isomeric state to lower excited states is strongly hindered and the resulting K isomer may have half-life as long as years. However,

the K quantum number may lose its validity and K isomers may have lifetime significantly shorter. This is namely the behaviour which is expected in the transitional region where nuclei may deviate from axial symmetry. Therefore, when the law in ΔK is not any more respected, K is no longer a "good" quantum number and it may indicate that the nucleus is not a prolate rigid rotor but rather a triaxial rotor. The first example of a K-isomer violating this rule is the $K^{\pi}=35/2^{-}$ isomer in ^{179}W. It was first observed in 1983 by J. Pedersen et al. [19] and was later explained by P.M. Walker et al. [20]. Thus K-isomers with lifetime in the μs range provide information about the validity of the K quantum number in axially asymmetric nuclei. The Hf-W-Os region appears like an ideal testing ground for the study of the K quantum number. Many K-isomers with lifetimes in the μs range have been already observed in stable nuclei and are predicted to occur on the neutron-rich side of the valley of stability in this region.

When these μs isomers decay to lower states, one can expect to study the unknown properties of nuclei whose structure was hardly studied before due to the experimental difficulty of populating nuclei in this transitional region. Thus the γ-decay studies of K-isomers would provide critical information about the evolution of the nuclear structure from prolate to spherical shape in the transitional region.

1.2.4 Blocked BCS theory

For several nuclei presented in this work, "blocked BCS" calculations as described by K. Jain et al. [18] have been performed to estimate the energies of multi-quasiparticle configurations for further comparison with the experimental data. We give here the principle of the calculations outlined in reference [21].

BCS theory [22] was first used to treat superconductivity in metals (which are macroscopic systems). A. Bohr, B.R. Mottelson and D. Pines [23] then suggested that the energy gap observed in the electronic excitation of superconductors is analogous to the energy gap observed in the excitation spectra of even-even nuclei. Therefore a pairing force between nucleons in time reversed orbits can reproduce the energy gap between the ground state and the first excited intrinsic states in nuclei.

• **Pairing and blocking**

BCS theory treats the pairing effect as a perturbation of the mean field Hamiltonian of the nucleus. To calculate the energy of a quasiparticle from the single-particle (Nilsson) energies, only the orbitals closest to the Fermi level need to be considered. Actually, the probability of excitations and scattering (see Section 1.1.1) to an unoccupied state is highest for particles near the Fermi surface. The quasiparticle energies for a state k are given by:

$$E_k = \sqrt{(\epsilon_k - \mu)^2 + \Delta^2}$$

with the pairing gap:

$$\Delta = G \sum_{k \neq k_j} u_k v_k.$$

Δ is proportional to the monopole pairing strength G. In the A$\sim$180-200 region, it is possible to treat neutrons and protons separately since they occupy different shells. Hence, the neutron pairing strength G_ν and the proton pairing strength G_π are treated independently.

To calculate Δ involves a sum over single-particle states k. However, some of these states may be occupied by quasiparticles and, as a result, these states must be removed (or *blocked*) from the sum since paired particles cannot scatter to singly occupied orbitals. Therefore the pairing energy is reduced and produced an accurate multi-quasiparticle energy spectrum. It constitutes the main difference between blocked BCS theory and usual BCS theory. The latter approximates the multi-quasiparticle energies by summing over all the single-quasiparticle states, which does not yield an accurate energy spectrum.

• **Multi-quasiparticle calculations**

To perform the calculations for a given nucleus $^{A}_{Z}$X, the deformation parameters ϵ_2 and ϵ_4 along with N, Z, G_ν and G_π are required. The Nilsson single-particle energies, ϵ_k, are calculated and those near the Fermi surface can be adjusted to produce the correct single-quasiparticle energy differences E_k (see section 1.1.1) in the neighbouring odd-mass nuclei. To obtain the multi-quasiparticle energies, E_{mqp}, it is necessary to calculate Δ for each configuration of protons and neutrons, blocking the appropriate orbitals. Since the occupation amplitudes v_k and u_k are dependent on Δ, it is an iterative process. Finally, the neutron and proton configurations are combined yielding:

$$E_{mqp} = \sum_{k_\nu} E^{\nu}_{k_\nu} + \sum_{k_\pi} E^{\pi}_{k_\pi}.$$

1.3 Projectile fragmentation technique: Why this method?

The exploration of the neutron-rich transitional A$\sim$180-200 nuclei was hardly possible to date because of experimental difficulties.

• **Fusion evaporation reactions**

Actually, the use of stable beam/target fusion-evaporation reactions does not lead to heavy, neutron-rich transitional nuclei. With this technique, two stable nuclei are fused together at an energy slightly above the Coulomb barrier and the resulting compound system evaporates nucleons before decaying by γ-ray emission. However, using such a process, one populates mainly nuclei in the neutron-deficient side of the valley of stability. The reason is that both stable projectile and target have a lower N/Z ratio compared to the heavy stable nuclei. In addition, due to the effect of the Coulomb barrier, the compound system preferentially emits neutrons, leaving a neutron-deficient nucleus.

• **Induced fission**

The fission of heavy nuclei can populate very neutron-rich nuclei but fission produces nuclei with significantly lower masses (A$\sim$100) than those studied here.

• **Deep inelastic reactions**

Deep inelastic reactions have been quite widely exploited to access high spin states in nuclei with a few neutrons more than the most neutron-rich stable isotopes [24, 25] but this technique suffers from a lack of selectivity. Here, at energies above the Coulomb barrier, nucleons are transferred between the target and projectile with a tendancy to equalise the N/Z ratio of the system. By using the most neutron-rich target and projectile combination in the relevant mass region, excited states of neutron-rich nuclei can be populated. One of the experimental problems with this method is the difficulty of identifying isotopes produced by transfer if the knowledge of the region of study is insufficient to use γ-ray cross coincidences with known transitions. Selective ancillary detectors are required with these reactions due to the large angular spread in the product nuclei.

• **Fragmentation reactions**

Fragmentation reactions involve relativistic projectiles being broken up on a target into lighter products. Such reactions produce a wide range of nuclei which have to be separated and identified by a spectrometer. The principal advantage of these reactions for our purpose is their ability to produce neutron-rich nuclei in the A=180-200 region. However, it is impossible to collect prompt γ-rays at the exit of the fragmentation target and only isomeric states of fragments being transported through the spectrometer can be efficiently studied.

The aim of this work was to study the nuclear structure of very neutron-rich nuclei in the transitional region (A$\sim$180-200) in general as well as the properties of K-isomers in particular. Projectile fragmentation reactions were thus performed to populate efficiently high spin isomeric states in these nuclei. The combination of a highly selective spectrometer, providing a clean identification of the nuclei, with a very efficient γ-ray set-up allowed us to collect new information about this challenging region.

2 Experimental techniques

The nuclei of interest are produced by projectile fragmentation, then separated and identified by the FRagment Separator (FRS) at GSI and finally implanted for further γ-spectroscopy studies. In the following chapter, the experimental technique is described step by step, from the primary beam acceleration to the γ-ray spectroscopy set-up.

2.1 Primary beam

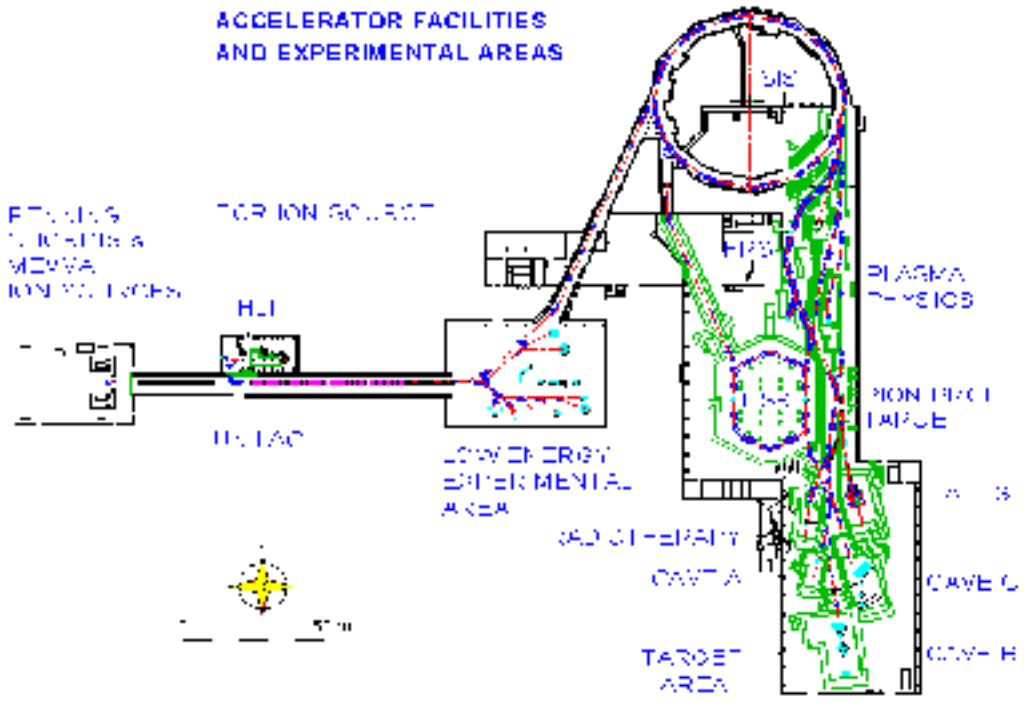

Figure 2.1: Overview of the accelerator facilities and experimental areas available at GSI.

The GSI heavy ion synchrotron SIS accelerates ions from ^{1}H to ^{238}U with energy ranging

from 50 up to 4545 MeV/nucleon and 50 to 1350 MeV/nucleon respectively [26, 27]. The beam characteristics are given in table 2.1.

Ions	all ions from H to U
$B\rho_{max}$	18 Tm
Energy	50 - 1350 MeV/nucleon for ^{238}U
	50 - 2000 MeV/nucleon for ^{20}Ne
Momentum spread	$\leq 10^{-3}$
Intensity	2.10^{11} ions/spill (Ne^{10+})
	4.10^{8} ions/spill (^{238}U)
Emittance	$\epsilon_x = \begin{cases} 1-5 & \pi$mm mrad (slow extraction) $\\ 5-20 & \pi$mm mrad (fast extraction) $\end{cases}$
	$\epsilon_y = 5-20\ \pi$ mm mrad
Cycle length	1 to 10 s
Time structure	10-8000 ms (slow extraction)
	20-50 μs (fast extraction)

Table 2.1: SIS beam characteristics[26].

A primary beam can either be directly directed to experimental areas or focused on a thick production target at the entrance of the FRagment Separator in order to generate secondary Radioactive Ions Beams (RIB) after fragmentation or fission reactions. Once separated and selected by the FRS, these RIBs can be investigated at the different FRS focal planes or injected either to the Experimental Storage Ring (ESR) or to any experimental area in the target hall as shown in figure 2.1.

For the experiment described here, after production by an ion source and first acceleration by the UNILAC (GSI linear accelerator), a primary beam of ^{208}Pb at 1 GeV/nucleon was delivered by the GSI Synchrotron SIS with an intensity of about 2×10^{8} particles per 12 second beam spill. The beam, sent to the FRS target chamber, impinged on a 1.6 g/cm^2 ^{9}Be target inducing fragmentation of the ^{208}Pb beam nuclei.

2.2 Projectile fragmentation

The nuclear fragmentation reaction is an important production mechanism for secondary beams. Different models can be used to describe the two steps of the reaction. The abrasion-ablation model is shortly examined in the lines below. Then the angular momentum distribution of the fragments is considered.

2.2.1 The fragmentation reaction : a two-step process

The reaction consists in the formation of projectile-like or target-like fragmentation products in more or less peripheral heavy-ion collisions at relativistic energies. A schematics of the reaction mechanism is drawn in figure 2.2.

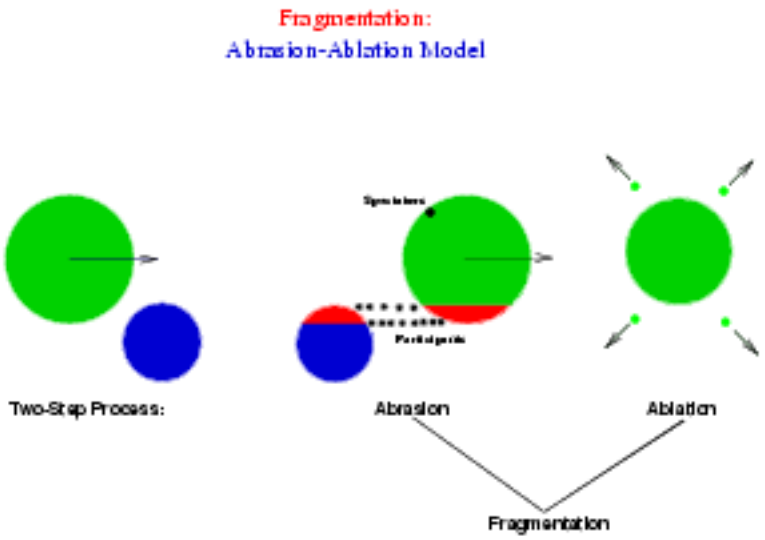

Figure 2.2: The abrasion-ablation model describes the projectile fragmentation reaction as a two-step process.

The reaction can be described in two steps which occur in two distinctly different time scales. The first step is described by a geometrical model called abrasion whereas the second reaction step consists in a statistical evaporation model called ablation [28].

The characteristic time of the abrasion is several times 10^{-23}s. In this first step, the beam colliding on the target abrades some nucleons, called participants, belonging to the overlapping part of projectile and target, whereas the other nucleons are considered to be only spectators. Both projectile and target have lost some nucleons and the resulting prod-

ucts of the reaction, called prefragments, have an excitation energy proportional, in a first approximation, to the number of abraded nucleons. According to the model, the main part of this excitation energy can be considered as an excess of surface energy due to the shape of the abraded fragment after collision.

In the second phase called ablation, the prefragments thermalize and de-excite by evaporating neutrons, protons and light nuclei as well as by fissioning and emitting γ-rays, within a time period of about 10^{-21}s which is very large compared to the interaction time (about 10^{-23}s). This is why the reaction is considered as a two-step process.

For a more complete understanding of the fragmentation process and its value for γ-ray spectroscopy, a consideration of the angular-momentum effects is needed.

2.2.2 Predicted angular momenta

With a statistical approach, similar to that proposed by Goldhaber [29] for the linear momentum of the fragmentation products, it is possible to estimate the angular momentum of the prefragment. This approach shows that the angular momenta introduced by the abrasion step in fragmentation reactions are of the order of (3-10)$\hbar$ for the prefragments [28]. As the evaporation of particles with low angular momenta is favoured during the ablation step, these values are essentially preserved up to the end of the deexcitation cascade. Thus the angular momentum distribution of a final fragment (see fig. 2.3) is the superposition of the angular momenta of the prefragments contributing to the considered fragment in the different evaporation chains and can be estimated by the following formula [30]:

$$P(J) \propto \frac{2J+1}{2\sigma_f^2} exp\Big(-\frac{J(J+1)}{2\sigma_f^2}\Big)$$

with the spin-cutoff parameter σ_f^2 given by :

$$\sigma_f^2 = \langle j_z^2 \rangle \frac{(A_p - A_f)(\bar{\nu} \cdot A_p + A_f)}{(\bar{\nu}+1)^2(A_p - 1)}.$$

A_p and A_f denote the projectile and fragment mass numbers respectively, $\bar{\nu}$ is the mean number of evaporated nucleons per abraded mass unit and $\langle j_z^2 \rangle$ is the average square of the angular-momentum projection of a nucleon in the nucleus. The value of $\bar{\nu}$ may be estimated to be about 2 by assuming that the excitation energy decreases by about 13 MeV per evaporation step (excitation energy induced in the abrasion stage is evaluated to 27 MeV per abraded nucleon)[31]. Values of $\langle j_z^2 \rangle$ are estimated on the basis of a semi-classical

consideration of the angular momentum distribution in the Woods-Saxon potential [31] and are written as :

$$\langle j_z^2 \rangle = 0.16 \cdot A_p^{2/3}(1 - \frac{2}{3}\beta),$$

where β is the quadrupole deformation parameter.

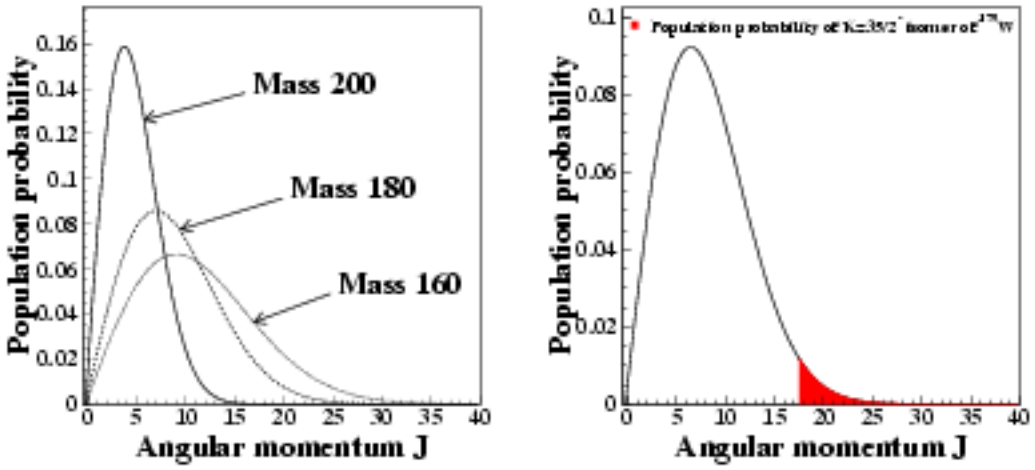

Figure 2.3: Population probability as a function of angular momentum for different masses. (left) and in the case of ^{179}W(right). Angular momentum values are higher for the lighter fragmentation products.

2.3 The FRagment Separator at GSI

Fragmentation reactions produce all kinds of fragments. To select certain species as secondary beams, a spectrometer called FRagment Separator (FRS) is used. The FRS is a high-resolution zero-degree spectrometer consisting mainly of 4 dipole sections disposed symmetrically with respect to a dispersive intermediate focal plane [26]. Table 2.2 gives the FRS main characteristics.

The separation of fragments is based on specific magnetic rigidities in front and behind an energy degrader mounted in the central plane. Thus the separation can be described in three steps :

- In a first stage, the ions produced by fragmentation at the entrance of the FRS are deflected and roughly separated according to their A/q ratio.

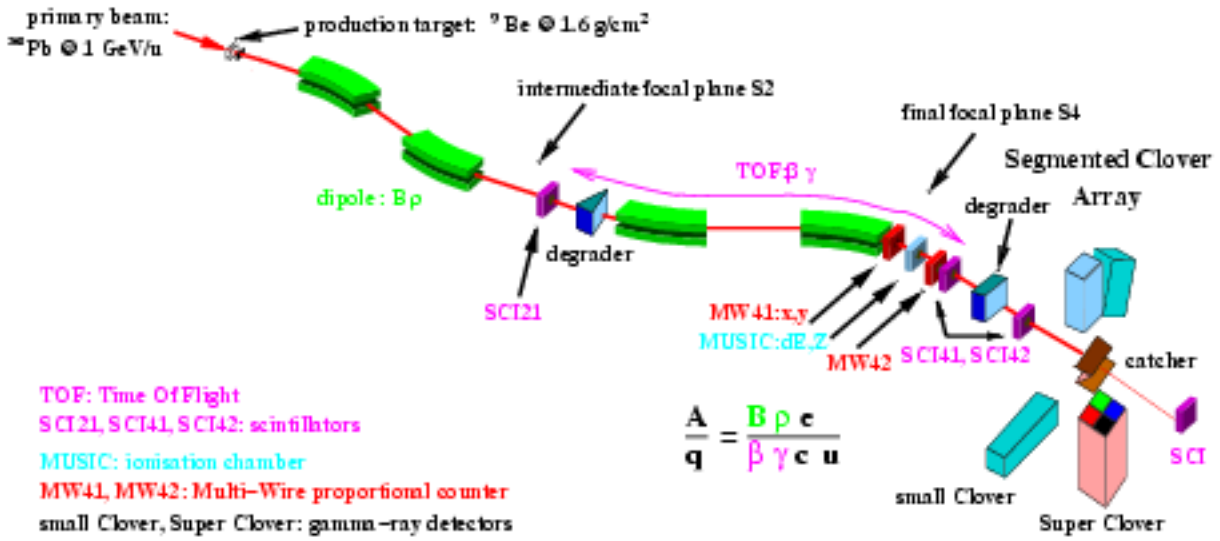

Figure 2.4: The FRagment Separator used to separate and identify the ions produced by projectile fragmentation at GSI coupled with the γ detector array.

- In a second stage, a shaped degrader situated in the middle focal slows down the fragments following their nuclear charge Z.
- Finally, the ions are again deflected and separated according to their nuclear charge Z and A/q ratio.

2.3.1 First magnetic selection

In the first stage (figure 2.4), the fragmentation products with a momentum p and an ionic charge q are sorted according to their magnetic rigidity ($B\rho$) and velocity v in the first section of the spectrometer.

$$\frac{A}{q} = \frac{p}{q} = \beta\gamma\frac{mc}{q} = \frac{(B\rho)}{\beta\gamma}\frac{e}{c\cdot u},$$

with the relativistic parameters $\beta = \frac{v}{c}$ and the Lorentz factor $\gamma = \sqrt{1/(1-\beta^2)}$, the speed of light c, the elementary charge e and the atomic mass unit u. In our experiment, a niobium foil placed just after the target ensured that the fragments were fully stripped so that we can assume $q = Z$ in the first stage of the FRS. Despite this foil, there was still a small probability to get hydrogen-like or helium-like fragments behind the target. Since the velocities βc of all fragments are approximately equal at the output of the target, the horizontal position at the central focal plane is directly correlated to the ratio A/q. Actually, the position x of

Magnification	V_1 = 0.79 (first stage)
	V_2 = 1.26 (second stage)
Dispersion (cm/%)	D_1 = -6.81 (first stage)
	D_2 = 8.62 (second stage)
Acceptance	In momentum : $\Delta p/p = \pm$ 1 %
	Angle : $\Delta\theta = \pm$ 10 mrad
Maximum magnetic rigidity	$B\rho_{max}$ = 18 Tm
Resolution of the first stage	$B\rho_1/\Delta B\rho_1$ = 1600
FRS length (target - final focal plane)	$\approx$ 74 m

Table 2.2: FRS parameters [26].

the fragments in the direction of the dispersion D_1 in the first section of the spectrometer is a measure of the relative deviation of their magnetic rigidity $(B\rho)_x$ compared to the value $(B\rho)_1$ on the ion-optical axis [34]:

$$\frac{(B\rho)_x - (B\rho)_1}{(B\rho)_1} = \frac{x}{D_1}.$$

As a consequence :

$$\frac{A}{q} \equiv (B\rho)_x \equiv x.$$

At this stage, many different fragments with approximately the same A/q ratio are transmitted (see Fig. 2.5). This is why a second selection is absolutely needed.

2.3.2 The shaped degrader

The energy degrader system, which is positioned in the dispersive intermediate focal plane of the FRS (see Fig. 2.4), consists mechanically of three different parts [32]:

- a set of 5 plane plate degraders,
- a wedged disc degrader pair,
- a wedged plate degrader pair.

These parts altogether form a wedge of aluminum with adjustable slope and thickness (see Fig. 2.6).

By adjusting the slope of the wedge, different ion-optical conditions can be fulfilled which result in two operation modes : the achromatic mode and the monoenergetic mode [33].

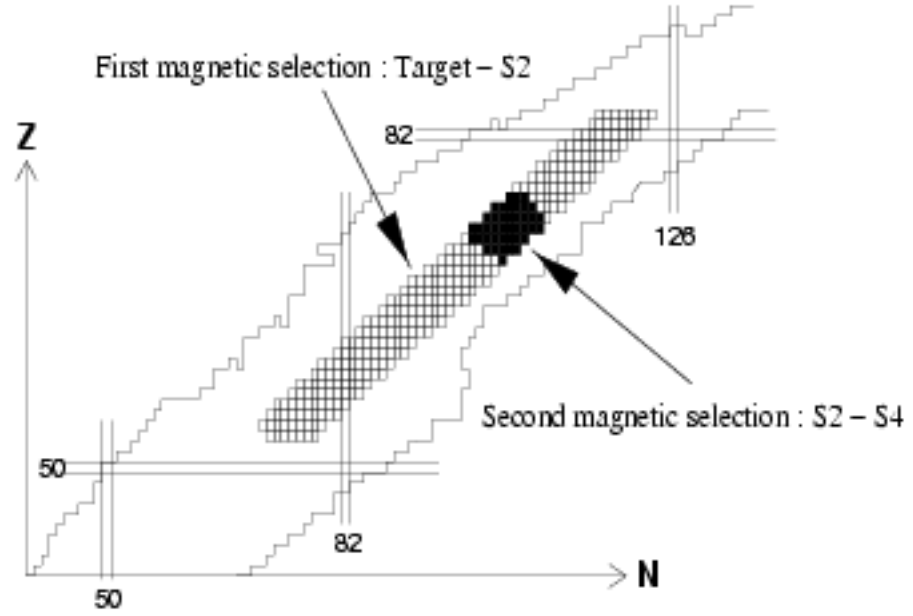

Figure 2.5: The effect of the two magnetic selections after the FRS obtained for a setting centered on ^{177}Ta (product of ^{208}Pb fragmentation). The white squares represent the fragments which are selected in the first part of the FRS whereas the black squares represent the fragments finally transmitted to the final focal plane.

• **The achromatic mode**

In the intermediate focal plane, the momentum distribution of the produced fragments is dispersed along the wedge. If the slope of the wedge is adjusted in such a way that the momenta of the selected fragments decrease by a constant factor due to their energy loss in the wedge, then the resulting momentum distribution of the fragments behind the degrader is refocused on a small spot at the exit of the degrader : this is the achromatic mode.

• **The monoenergetic mode**

If the slope of the wedge is adjusted in such a way that all the different momenta of the selected fragments in front of the degrader are exactly compensated by their different path-lengths through the wedge, then the degrader acts in the monoenergetic mode. In this case, all fragments are deflected by the second dipole stage in the same way and their spatial distribution at the exit of the separator stays the same as in the intermediate focal plane.

In our experiment, we used the achromatic mode to get the best separation of the selected

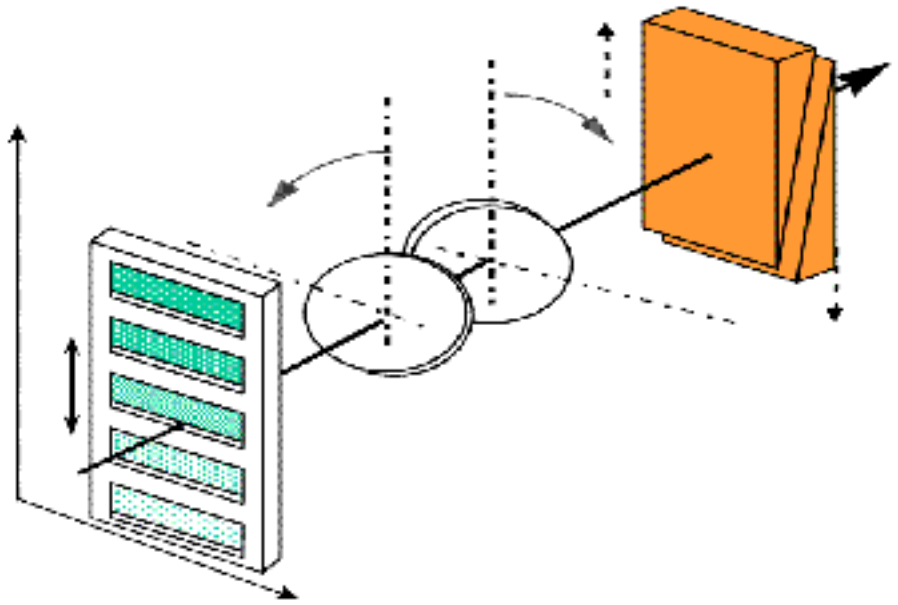

Figure 2.6: Schematic view of the degrader system.

fragments at the exit of the degrader. The degrader thickness was set to 5547 mg/cm^2 and corresponded roughly to 50% of the range of the selected fragments.

Then a second magnetic selection separates completely the fragments according to both A/q and Z (the energy loss in the degrader depends on the nuclear charge Z). Despite the presence of a niobium foil at this stage to have fully stripped ions, some fragments capture electrons when passing through the degrader and different low charge states are observed at the final focal plane.

2.3.3 Second magnetic selection

The fragments are again deflected according to their magnetic rigidity $(B\rho)_2$ in the second half of the spectrometer (see figure 2.4). The horizontal position in the final image plane is a measure of the relative loss of momentum in the intermediate energy degrader. This gives access to charge information of the fragment.

2.3.4 Identification

The identification set-up associated to the FRS is in charge of recording the fragment parameters: position, energy loss and time of flight. Different kinds of detectors are used for

this purpose : the x position of each fragment is deduced at each focal plane using plastic scintillation detectors, whereas the combination of the two scintillator time signals gives the Time Of Flight (TOF) between the two focal planes [34]. The energy loss information was obtained from an ionisation chamber called MUSIC [35]. Two x-y position sensitive Multi Wires chambers [36] were placed in front and behind MUSIC to correct the energy loss of each fragment using the position information. These parameters are, in principle, sufficient to determine completely the mass A and charge Z of each ion reaching the final focal plane.

The Multi Wire chambers : beam tracking

Multi-Wire Proportional Counters (MWPC) have been developed at GSI for the detection of heavy ions at relativistic energies and for beam tracking. In our experiment, an ensemble of six MWPC was used to track the beam along the FRS and give the beam position at each focal plane when setting up the beam line. They have a size of 20×20 cm^2 and a thickness of 10 cm. A schematic layout of a two-stage MWPC is shown in fig. 2.7.

The planar anode A consists of 20 μm gold-plated tungsten wires with a pitch of 2 mm while the cathodes X and Y are made of 50 μm gold-plated tungsten wires with a pitch of 1 mm. The wire directions in X and Y are orthogonal to each other, while the wires of plane A are diagonal to them. Furthermore, a planar electrode structure is added consisting of two meshes labeled G and T with a spacing of 6 mm. Typical potentials applied to the electrodes are indicated in fig. 2.7. The readout planes X and Y are at ground potential. The detector was filled with a gas mixture of 80% argon, 19% CO_2 at a pressure of 1 atmosphere during the experiment.

The electron avalanche caused by the passage of a charged particle through the detector is collected on the anode A and induces positive signals on the adjacent wires in the X and Y cathodes. These signals are used to determine the x and y positions of the incident fragment by the delay-line readout technique. Each wire of the planes X and Y is connected to a tap of a delay line with a delay of 4 ns per tap. The signal propagates through the left and right side of the delay line. At the end of the delay line, the signals are amplified and fed in the STOP of a TDC while the START signal is derived from the anode. The time difference between the left and the right side of the delay line is a measure of the position with a resolution better than 1 mm whereas the sum of left and right should be a constant, namely the total length of the delay line ($\sim 1\mu$s in our experiment). To avoid pile up, the particle rate should be kept below 100 kHz.

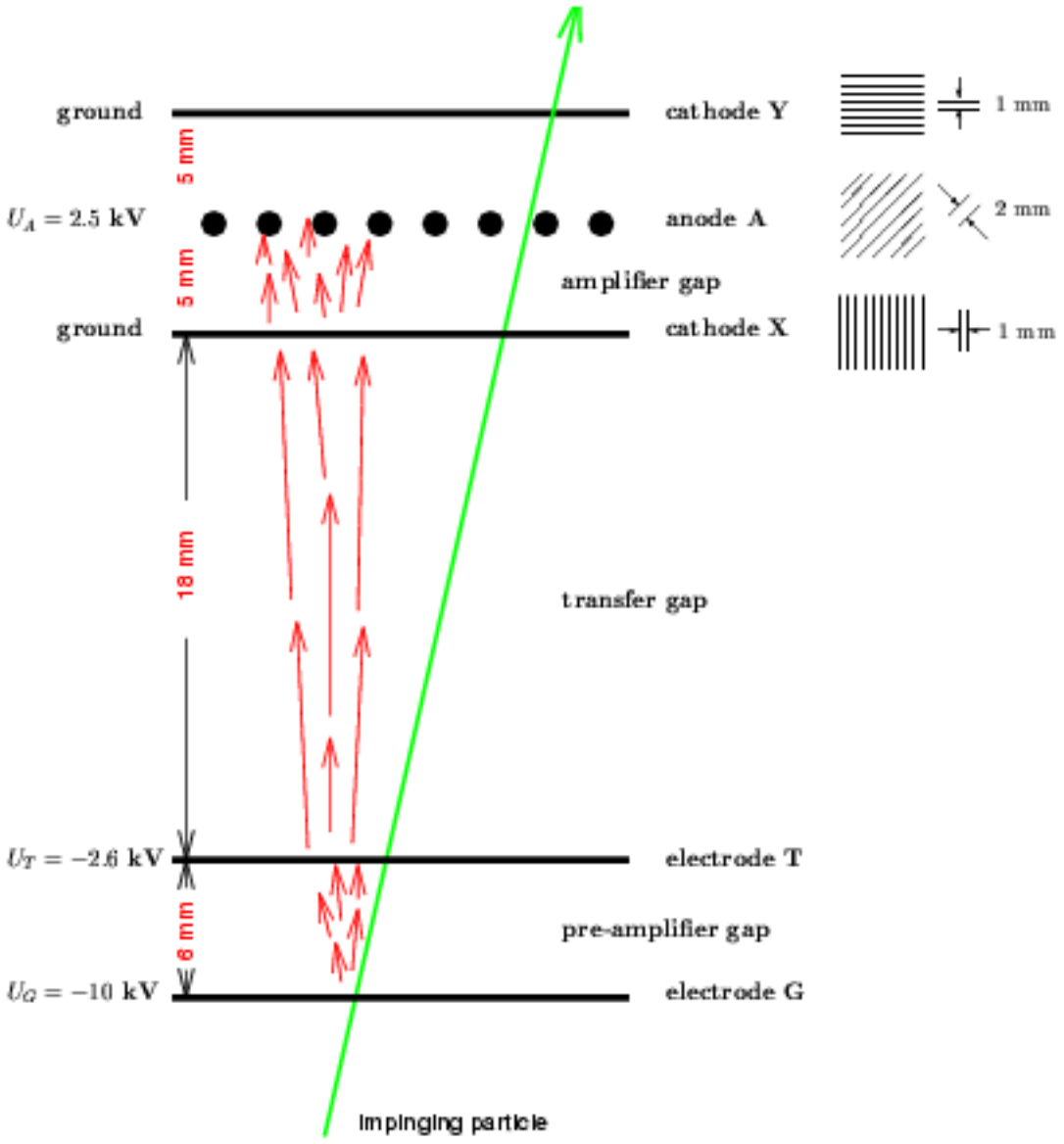

Figure 2.7: Two-stage Multi-Wire Proportional Counter (MWPC) developed for the detection of heavy ions at relativistic energies and for beam monitoring [36]. The green arrow represents the trajectory of the heavy ion traversing the counter while the red arrows represent the electron avalanche.

The inhomogeneities of these detectors can perturb the FRS resolution and the chambers have to be taken away once the FRS has been tuned. Only the two MWPCs at the final focal plane S4 are kept to give position information for further corrections in the MUSIC. Therefore a plastic scintillation material was used to track the fragments during the experiment.

The scintillators : position and time of flight

A combination of two plastic scintillators SCI21 and SCI41 (see Fig. 2.4) is used to measure the fragment positions at intermediate and final focal plane respectively as well as the Time of Flight (TOF) between these two planes. The organic scintillation material BC420 (Company Bicron) provides high light output and a fast signal rise time (0.5 ns). According to the size of the central image plane of the FRS, the scintillation plates cover an active area of 80 mm (vertically) $\times$ 200 mm (horizontally) with thicknesses of 3 mm for SCI2 and 5 mm for SCI4.

On the sides of each scintillator multi-strip lightguides are coupled to photomultipliers. Due to the restricted available space, the detector mounted in the central image plane was only read out in the horizontal direction whereas the detector at the final image plane was read out in both horizontal and vertical directions. The anode signals of the photomultipliers were fed into constant fraction discriminators (CFD). The digital outputs of these units served to start and stop a time-to-analog converter (TAC) delivering information on the position of the particles from the time difference of the signals of each detector.

The TOF was measured by the time difference of the signals of the corresponding left and right photo-multipliers of both detectors, respectively. The spatial resolution obtained is about 1 mm and the TOF, measured over a length of about 36 m (distance between S2 and S4), has a time resolution of about 180 ps. Due to its fast response time, the scintillator placed at the final focal plane was used as the main trigger of the full data acquisition.

The MUSIC : energy loss

A MUlti Sampling Ionisation Chamber (MUSIC) installed at the exit of the separator is used to measure energy loss of the fragments. The chamber, shown in figure 2.8, consists of a cathode, a Frisch grid and an anode plane divided into four independent volumes of gas with a total efficient length of 40 cm. It covers an area of 200 $\times$ 200 mm^2 and was operated sustaining a constant flow of a mixture of 90% argon and 10% methane gas at atmospheric pressure. Entrance and exit windows were made of 25 μm Kapton foil covered

by an aluminum layer of 40 $\mu g/cm^2$. The electric field was horizontal, perpendicular to the direction of the heavy-ion beam.

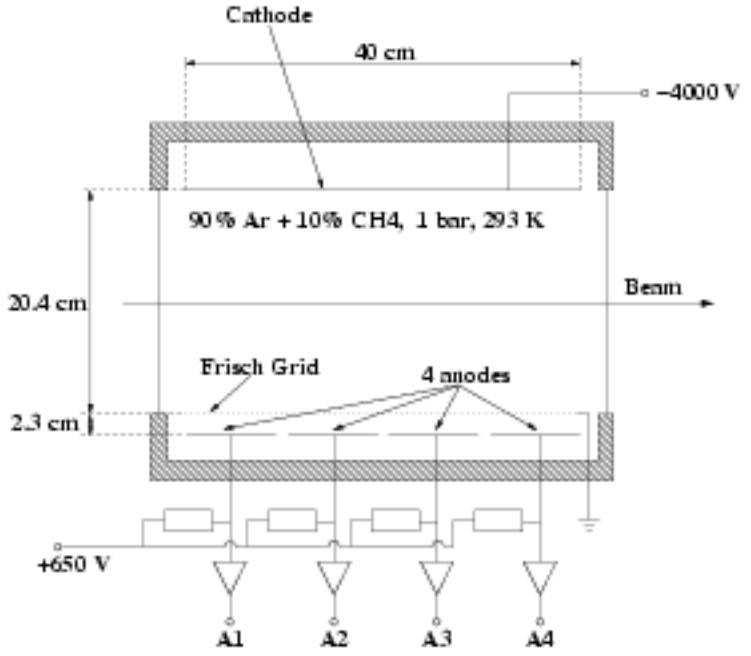

Figure 2.8: Schematic view of the Multi-Sampling Ionisation Chamber (MUSIC) developed for the charge determination of heavy ions at the FRS [35].

The four sections of gas volume deliver four energy loss signals through four anodes, each coupled to a charge sensitive preamplifier. Taking the average of the energy-loss signals of all anodes,corrected for position dependence by using the multi-wire chambers, the nuclear charge of the fragments could be determined with a resolution of 0.3 to 0.5 charge units.

2.4 Implantation

At the final focal plane, the fragments are again slowed down by a second degrader and finally stopped in a 4 mm thick Al catcher. According to the large beam spot size, the stopper covers an area of about 80 mm (vertically) × 200 mm (horizontally). Its thickness has been chosen in order to stop fragments with a maximum incident energy of 100 MeV/nucleon. Actually, the range of ^{208}Pb at 100 MeV/nucleon in silicon is estimated to be 2 mm (ref. [37], p.156). The ions which have broken up before reaching the Al stopper are recorded by a third scintillator placed just behind the second degrader. Furthermore, a fourth veto scintillator

placed behind the stopper detects the ions which do not stop in the catcher.

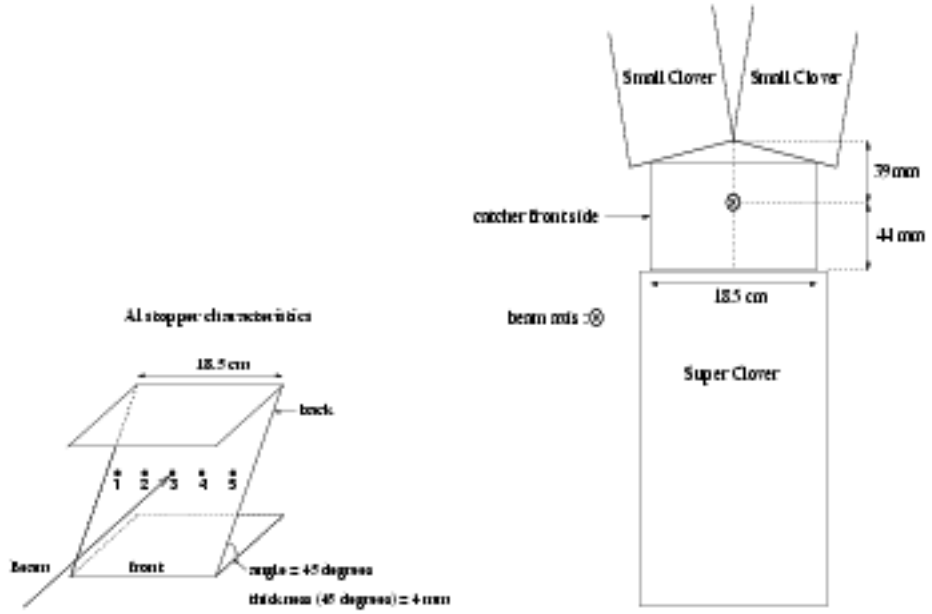

Figure 2.9: Characteristics of the stopper and scheme of the Clovers set-up.

2.5 Gamma-ray detectors

To study the γ spectroscopy of the finally selected fragments, the implantation area was surrounded by an array of three Segmented Clover and one Super Segmented Clover Ge detectors [38] arranged in a packed geometry (see Fig. 2.9). All four Clover detectors were placed in a plane perpendicular to the beam line. Each Segmented Clover detector consisted of an ensemble of 4 Ge-crystals of 7 cm length and 5 cm diameter whereas the Super Segmented Clover detector consists of four coaxial Ge detectors of 14 cm length and 7 cm diameter. Each crystal provided one energy signal and was thus used as an independent Germanium detector. Since no Doppler shift correction was required in our experiment, the position information provided by the different segments was not used.

2.6 Electronics and Data Acquisition

The electronics consisted of two main parts : the standard FRS branch and the user branch. The standard FRS electronics processed mainly signals related to :

- the positions and time of flight coming from the scintillators at the intermediate focal plane S2 (SCI21) and at the final focal plane S4 (SCI41),
- the x and y positions measured in the MWPCs placed before (MW41) and behind (MW42) the MUSIC chamber,
- the four energy loss signals in the MUSIC chambers as well as the time signals, temperature and pressure,
- the energy loss signals of the scintillator SCI42 located behind the degrader at the final focal plane,
- the energy loss signals of the veto scintillator SCI43 located after the implantation set-up,
- some scalers to read the number of free triggers, accepted triggers, spills, fragments produced at the target as well as a 1 Hz clock.

A user branch is associated to this standard branch and consisted of the electronics for γ spectroscopy :

- 16 γ-ray energy signals of the 16 crystals,
- 16 time signals with time range from 0 to 8μs (TDC),
- 16 time signals with time range from 0 to 80μs (TAC).

The electronics of the Segmented Clover Array is shown in figure 2.10. Each individual Ge crystals gave one signal to an ADC from which we got the energy information. Another signal went to a CFD. Each CFD had two outputs. All first CFDs outputs mixed together into an OR gate generating the Ge-OR trigger whereas the second output fed in a coincidence module. The coincidence, built from the Ge time signal and the Master Trigger, fed in the START of a TAC and the STOP of a TDC. All the TDCs had a common START given by the Master Trigger and all TACs had a common STOP which was given by the delayed Master Trigger.

The full acquisition was started using the scintillator SCI41 as a trigger. The electronic logical gate was opened for a period of 80 μs after implantation of a heavy ion (SCI41 trigger) and all subsequent signals from particle and gamma detectors which were read in this time

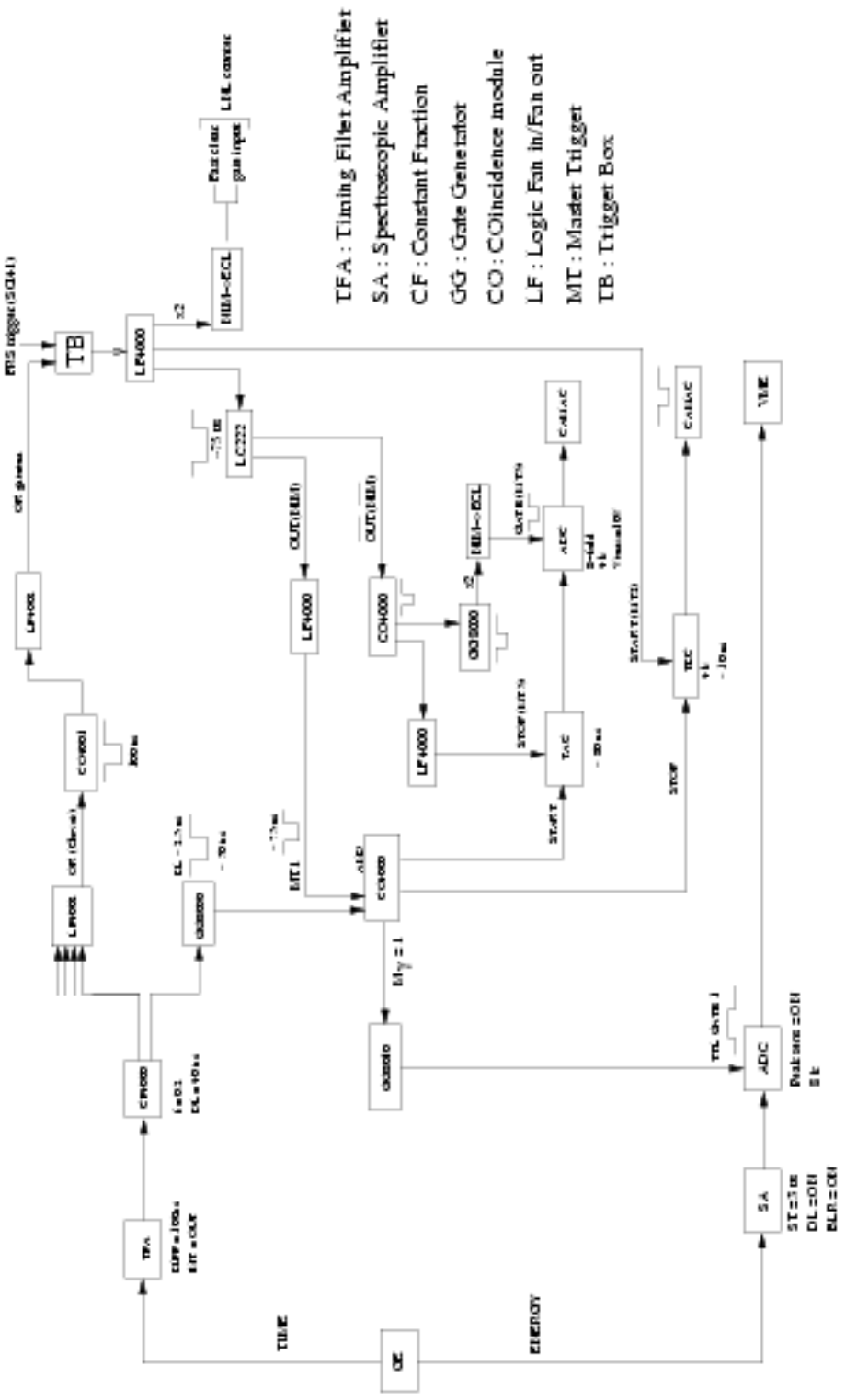

Figure 2.10: Electronics scheme of the γ-ray acquisition

period were stored as a single event. Thus one event consisted of the FRS subevent (48 parameters described previously) and the γ-ray subevent (48 parameters described above). Each time the acquisition started, the 48 parameters of the FRS subevent were recorded wheras only a part of the γ-ray subevent was recorded. Actually, the gamma-ray subevent is of variable length. Only the data from crystals which have effectively fired were recorded whereas "empty" crystals were suppressed (zero suppression). For each gamma detector, the time between the implantation and an associated detected γ-ray (either prompt or delayed) was recorded over two time ranges : 0$\rightarrow$8 μs (TDC) and 0$\rightarrow$80 μs (TAC). This technique allowed a correlation of isomeric γ-rays with the identified ion, while room background and radiation from other nuclei are strongly suppressed.

The total transmitted ion rate was kept below 1 kHz in order to minimise dead-time losses. As a consequence, the average time between consecutive ions was larger than 1 ms. The data were finally saved to List Mode Data (LMD) files and analysed on an event-by-event basis using APE (Analysis in PAW [39] Environment) software package.

To summarize, the ions produced by fragmentation are separated with the help of two main devices : magnets which provide a dispersion following magnetic rigidity and a degrader slowing down the fragments according to their nuclear charge. Fragments reaching the final focal plane are identified in nuclear charge (MUSIC) and mass-to-atomic-charge ratio (Scintillators), implanted into a thick catcher and γ-rays in coincidence with the implanted fragments are recorded. the germanium detectors (Clover Array). The following chapter will describe in more details the procedure used to identify fragments and their related γ-rays.

3 Data analysis

Very neutron-rich nuclei as well as stable isotopes in the A$\sim$180-200 region were successfully populated in the ^{208}Pb beam fragmentation and identified using the experimental techniques described previously. This chapter reviews the off-line analysis procedure used to observe and study these nuclei.

3.1 Settings

During the experiment, eight different nuclei regions were scanned. Each setting corresponds to a particular fully stripped isotope centered at the final focal plane S4 of each region. Table 3.1 gives details about magnetic rigidities, degrader thicknesses and number of recorded events obtained for each setting. The number of recorded events includes only the total number of projectile fragments which were recorded and analyzed. Fission fragments are not taken into account. The rate is just the ratio of this number to the data collection time of a setting. As the spill structure varied considerably during the experiment, no rate per spill is given.

Setting	$(B\rho)_1$ (in Tm)	$(B\rho)_2$ (in Tm)	S4 degrader thickness	Collection time	Number of recorded events	Rate (ions/sec)
^{177}Ta	12.609	9.2029	2890 mg/cm^2	39 h 13 min	15 956 217	113
^{170}Dy	13.476	10.491	5290 mg/cm^2	36 h 35 min	52 607	0.4
^{191}W	13.721	10.049	3540 mg/cm^2	65 h 19 min	3 578 216	15
^{184}Lu	13.542	10.289	4330 mg/cm^2	52 h 54 min	1 070 261	5.6
^{180}Ta	12.836	9.4426	3320 mg/cm^2	10 h 4 min	2 687 378	74
^{159}Tb	11.044	8.0190	3050 mg/cm^2	14 h 39 min	639 346	12.1
^{140}Dy	10.947	7.8558	2750 mg/cm^2	15 h 41 min	58 527	1.0

Table 3.1: Parameters of the experiment for the different settings in their chronological order.

3.2 FRS detector calibration

For the set-up and tuning of all identification detectors and the spectrometer itself, a set of measurements with low intensity primary beams of different energies was performed prior to the main experiment runs. This procedure allowed an absolute calibration of the TOF and energy loss, as well as the horizontal positions at the intermediate and final focus. The following section describes in some detail the calibration procedure followed for each detector.

3.2.1 The scintillators : position and time of flight

A combination of two plastic scintillator signals is used to determine the Time Of Flight (TOF) of the fragments. The first scintillator is placed at the intermediate focal plane and gives the *stop* signal for the TOF measurement whereas a second scintillator at the final focal plane gives the *start* signal. The TOF was calibrated by focusing the primary ^{208}Pb beam with 3 different thicknesses of the S2 degrader. The calibration is linear :

$$TOF(ns) = c_2 + c_1 \cdot T_{channel}.$$

The slope c_1 is given by a clock calibrating the TAC signal of each scintillator. The offset c_2 is deduced from the three calibration points as follows.

For each different degrader thickness, the beam is focused with different magnetic rigidities $(B\rho)_2$. Furthermore, the A/q ratio is known. By using the formula :

$$\beta\gamma = (B\rho)_2 \cdot \frac{q}{A} \cdot \frac{c}{u}$$

with A = 208, q = Z = 82, $u \sim 931.4\,\mathrm{Mev/c^2}$ the atomic mass unit, c the velocity of light. We can then deduce the velocity v of the fragments :

$$\frac{v}{c} = \frac{\beta\gamma}{\sqrt{1+(\beta\gamma)^2}}.$$

The offset c_2 is extracted from the linear calibration of $\beta \cdot TOF$ (see Fig. 3.1).

Moreover, the scintillators are also used as position-sensitive detectors. The position is determined by the time difference of the TAC signals between left and right sides of each detector. The calibration is obtained by defocusing the primary beam of ^{208}Pb in order to cover completely the scintillators in horizontal position x. In our case, the range of both scintillators was $\pm$ 8 cm. The linear calibration of the positions in scintillators at S2 and S4 is obtained by using the Multi-Wire Chambers at S2 and S4 respectively (see Figure 3.2).

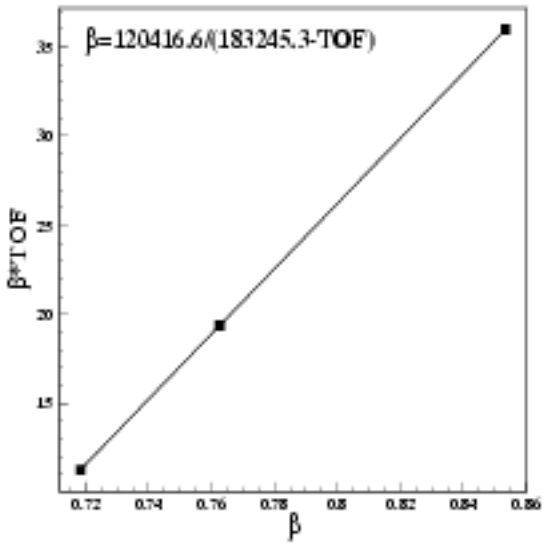

Figure 3.1: Determination of the velocity as a function of TOF. The fit function is deduced from the linear fit of $\beta \cdot TOF$ as a function of β. The three calibration points correspond to three different thicknesses of the S2 degrader.

The position information is then used to achieve the proper geometrical corrections to the magnetic rigidity of each fragment in the second FRS stage :

$$B\rho_{2cor} = (B\rho)_2(1 - \frac{x_4 - V_2 x_2}{D_2}),$$

where $(B\rho)_2$ is the magnetic rigidity of the fragment at the ion-optical axis, given by the magnetic fields of the dipole magnets and their radii (see Table 3.1), x_2 and x_4 are the positions of the fragment at the intermediate and final focal planes, given by the two scintillators. $V_2 = 1.094$ and $D_2 = 6969$ mm are respectively the magnification and the dispersion of the FRS second stage.

Combining the TOF and $B\rho_2$ information, the mass-to-charge ratio A/q corrected for position is finally deduced :

$$\frac{A}{q} = \frac{e}{cu}\frac{B\rho_{2cor}}{\beta\gamma} = \frac{e}{cu}\frac{(B\rho)_2}{\beta\gamma}(1 - \frac{x_4 - V_2 x_2}{D_2}).$$

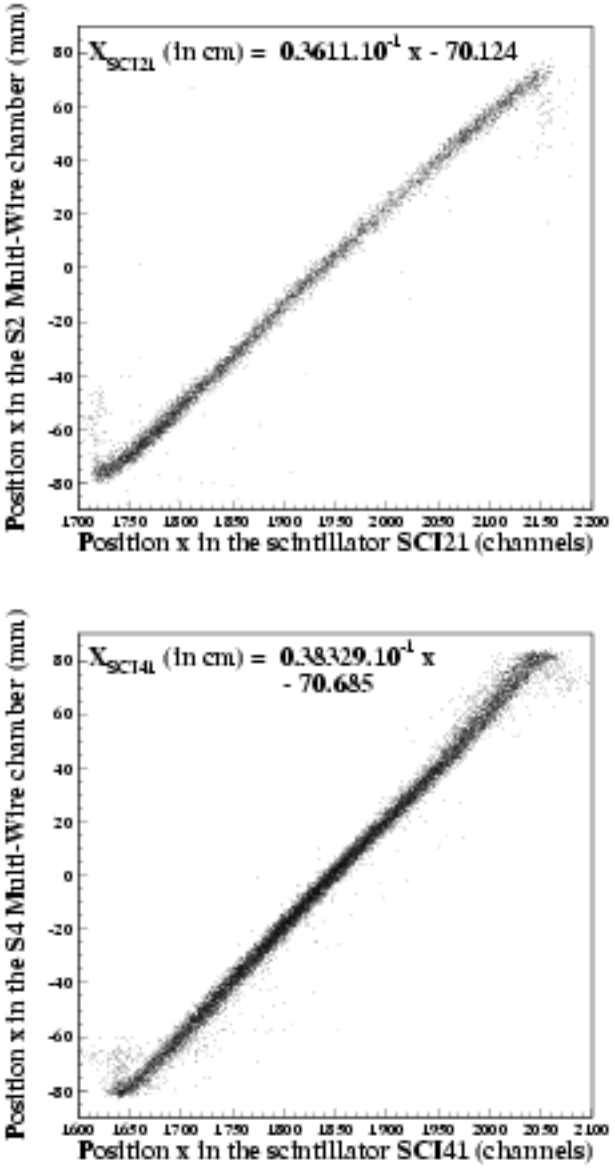

Figure 3.2: The position of the defocused beam in the Multi-Wires chambers used to calibrate the corresponding position in the scintillators. Top : calibration of the scintillator SCI21 with the Multi-Wire chamber MW21. Bottom : calibration of the scintillator SCI41 with the Multi-Wire chamber MW42.

3.2.2 The MUSIC : energy loss and charge

A MUlti Sampling Ionisation Chamber (MUSIC) located at the final focal plane is used to measure energy loss of fragments and deduce the nuclear charge of the fragment. It is an ensemble of four independent volumes of gas with a total efficient length of 40 cm. These four sections deliver four independent energy loss signals through four anodes as well as four x position signals obtained by measuring the drift time of electrons. The energy loss signals combined together allow to separate fragments with the same velocity but different Z with a resolving power of $\Delta Z/Z \leq 1/100$. The energy loss is obtained from the algebraic mean of the four signals.

As already mentioned, MUSIC position correction is obtained from the MWPCs located upstream and downstream MUSIC. Actually, the position of the fragments in the MWPCs, x_{MW41} and x_{MW42}, associated with the distance between these two MWPCs, DIST(MW42-MW41), gives the exit angle of the fragment via the formula (see Fig. 3.3):

$$\tan\alpha = \frac{x_{MW42} - x_{MW41}}{DIST(MW42 - MW41)} \sim \alpha$$

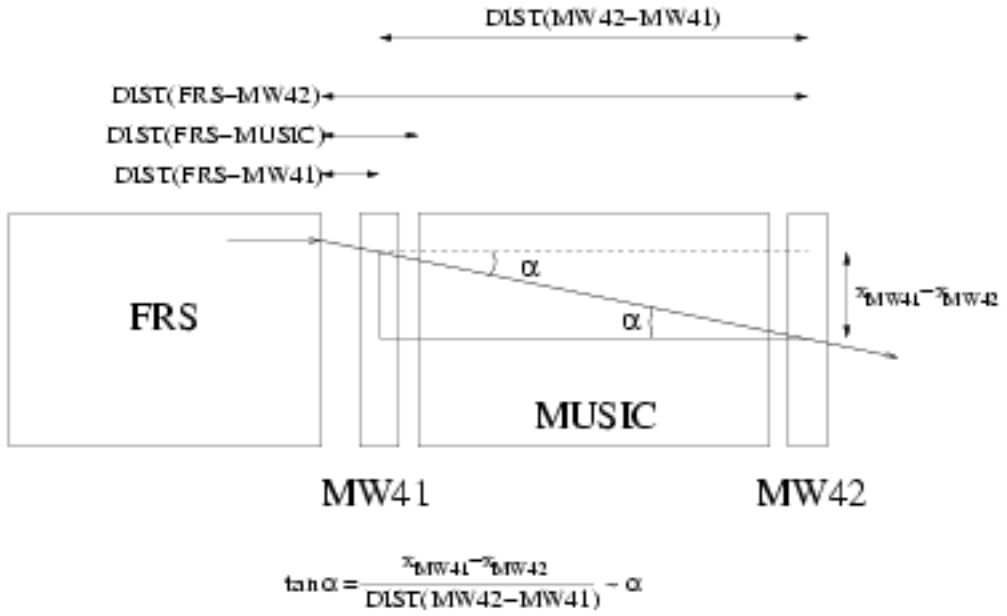

Figure 3.3: The angle α of the fragment at the exit of the FRS is obtained from the measured distances between each detector and the end of the FRS and the fragment positions in MW41 and MW42.

From this angle, the position of the fragment in the MUSIC,x, is reconstructed :

$$x = x_{MW42} - DIST(MUSIC - MW42) \cdot \alpha$$

and the energy loss is corrected (see Fig. 3.4):

$$\Delta E_{cor} = \Delta E \cdot \frac{\Delta E_0}{\Delta E_0 + a \cdot x + b \cdot x^2 + c \cdot x^3}$$

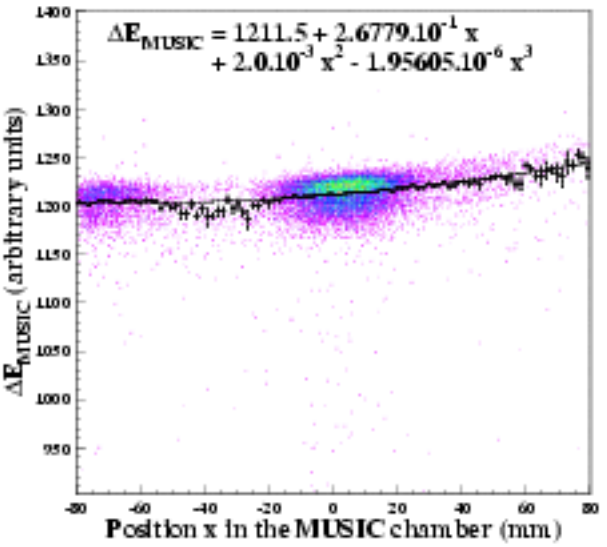

Figure 3.4: Correction of the drift of the energy loss ΔE_{MUSIC} in the MUSIC chamber as a function of the horizontal position x using a polynomial function of order 3.

Then the energy loss can be expressed as a function of β and nuclear charge Z as follows :

$$\Delta E = \frac{Z^2}{f(\beta)}$$

The function $f(\beta)$ is deduced from different settings using the primary beam with different energies (see Fig. 3.5).

3.3 Gamma-ray detector calibration

Germanium detectors have been calibrated using a mixed source whose characteristics are listed in table 3.2.

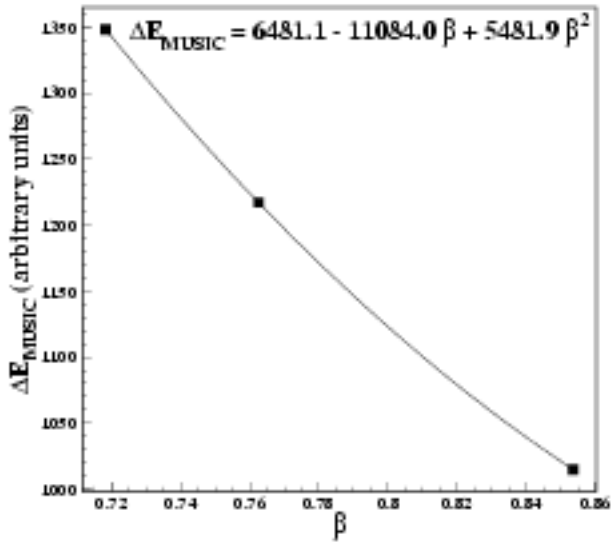

Figure 3.5: Fit of the MUSIC energy loss as a function of β. The three calibration points correspond to three different thicknesses of the S2 degrader.

Nuclide	γ-ray energy (in MeV)	γ-rays produced in the source (s^{-1})	Half-life
^{241}Am	0.060	583	432.2 years
^{109}Cd	0.088	112	462.6 days
^{57}Co	0.122	50	271.79 days
^{139}Ce	0.166	10	137.6 days
^{113}Sn	0.392	15	115.1 days
^{137}Cs	0.662	1238	30.17 years
^{88}Y	0.898	32	106.6 days
^{60}Co	1.173	1321	5.272 years
^{60}Co	1.333	1321	5.272 years
^{88}Y	1.836	33	106.6 days

Table 3.2: γ-rays used for photopeak efficiency calibration from the mixed source.

For photopeak efficiency calibration, data were recorded for five different points on both sides of the catcher. The photopeak efficiency was equal to 5.1% at 1.33 MeV for the central position of the catcher. The function used to perform the efficiency calibration is the exponential of a polynom of logaritms of the form :

$$\epsilon_{E_\gamma} = exp\left(\sum_{i=1}^{4}\left[a_i \cdot ln(E_\gamma)^i\right]\right)$$

The dependence of efficiency on position was interpolated from the efficiency curves obtained for these different source positions (see Fig. 3.6).

The intrinsic time resolution of the detectors was about 8 ns at 1.3 MeV and 20 ns at 0.1 MeV. The energy resolution was 3.7 keV at 1.3 MeV. Different energy calibration were performed between the different settings of the FRS in order to correct the eventual drifts of the detectors.

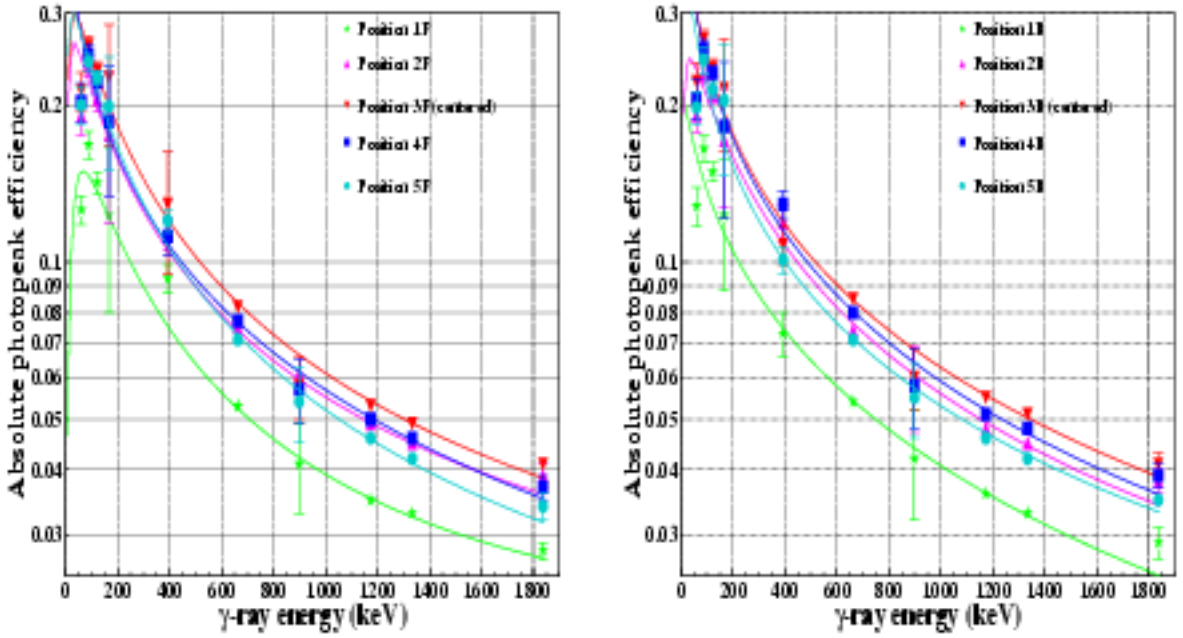

Figure 3.6: Results of the photopeak efficiency calibration of the Segmented Clover array. The right graph corresponds to calibration with the source on the side where the beam is entering the catcher. The left graph corresponds to calibration with the source on the side where the beam would leave the catcher. More details about source positions are given in figure 2.9.

3.4 Identification procedure

To identify the fragments implanted in the catcher, the information obtained from scintillators, MWPCs, MUSIC chamber as well as Segmented Clover Array was used. A step-by-step procedure allowed to select projectile fragments whereas events produced by other reactions along the FRS were rejected.

3.4.1 Selection of projectile fragments

At the primary target, projectile fragmentation was mainly in competition with fission. As a result, many fission contaminants with low Z but similar A/q ratio were also selected by the FRS. These contaminants could only be suppressed during off-line analysis by using the MUSIC chamber. Since the energy loss in the MUSIC depends mainly on Z, ions with very different Z produce very different energy loss signals in the MUSIC. Therefore two groups of ions are clearly seen in the MUSIC chamber (figure 3.7) and only fragmentation products are selected.

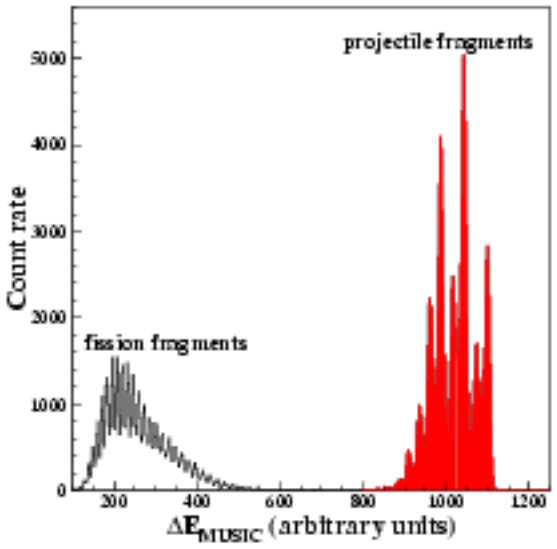

Figure 3.7: Rejection of fission events using the energy loss in the MUSIC chamber. Two groups of ions can be seen : fission fragments and projectile fragments.

3.4.2 Break-up events

Before implantation, fragments are slowed down by a thick Al degrader. A scintillator placed after this degrader detects the energy loss of the fragments which broke up before reaching the stopper. By plotting the energy loss in the SCI42 scintillator versus the energy loss in the MUSIC, one can suppress the break-up events easily. At this stage of the analysis, only a general gate on the group of "good" heavy ions is set (Figure 3.8). A later selection will be needed to proceed with the fine analysis of the nuclides.

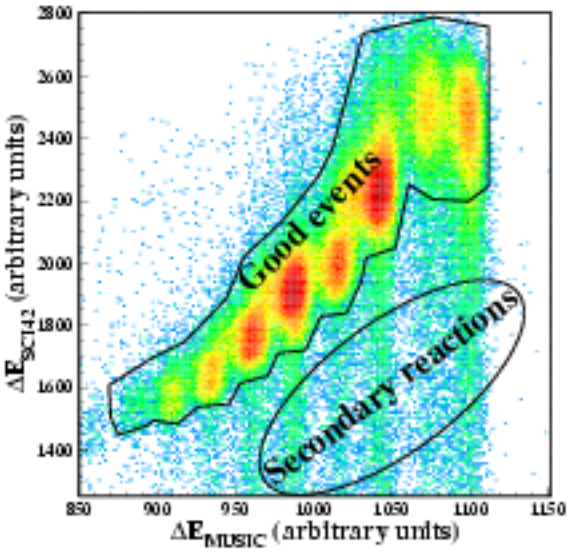

Figure 3.8: Rejection of break-up events using the energy loss in the SCI42 scintillator plotted versus the energy loss in the MUSIC chamber. The main group of ions is selected.

3.4.3 The charge state spectrum

Due to ionic charge-changing processes in the intermediate degrader, the different fragments will not reach the final focal plane with the same charge state. The different charge states are clearly identified by plotting the position of fragments at the intermediate focal plane versus the A/q ratio in the second stage of the FRS as described by M. de Jong et al. [40]. In figure 3.9 (left part), three different groups of ions appear. The ions on the left hand-side are the fragments which did not change their charge state between the first and the second half of the spectrometer. The middle one represents ions which have gained one electron between

the first and the second stage of the FRS whereas the last group on the right hand-side are the ions which have gained two electrons. This plot is used to select the charge state in order to have a clean spectrum for isotopic identification which takes place at the final focal plane S4 (right part of fig. 3.9). For convenience, in the following, the ions with $\Delta q=0$ are called fully-stripped ions, the ions with $\Delta q=1$ are called H-like ions and the ions with $\Delta q=2$ are called He-like ions and we may refer to the Δq difference as charge state.

At this stage, it is important to notice that, on the contrary of fragmentation cross-section measurements, the charge state of the ions does not affect the spectroscopic study of the nuclei we are interested in. Consequently, each fragment, as soon as its charge and mass was clearly determined, could be studied, whatever its charge state history was.

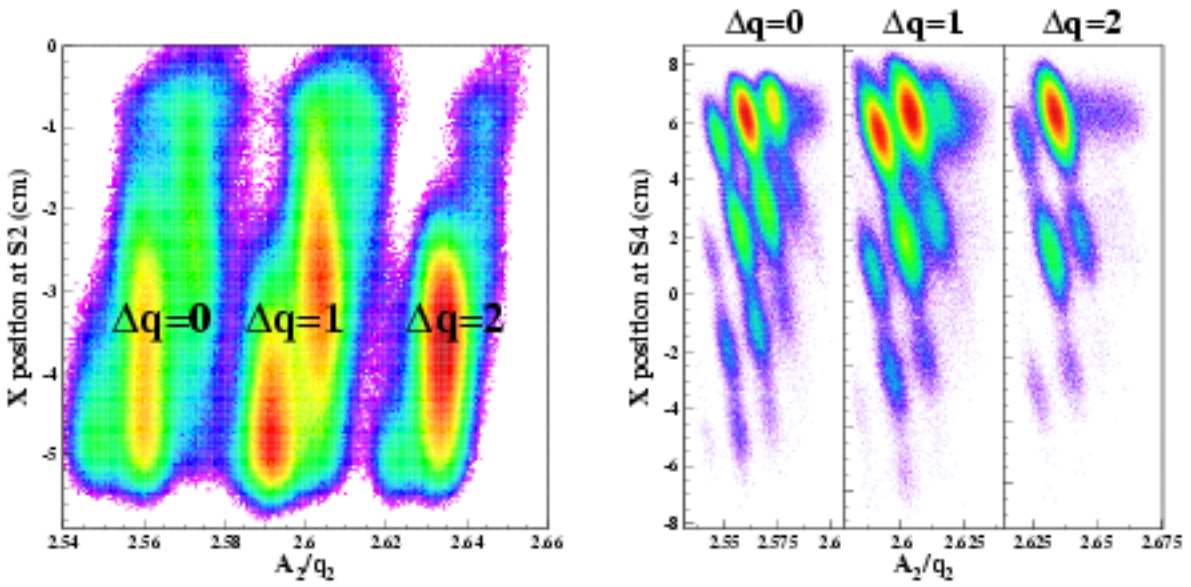

Figure 3.9: This figure represents the charge loss of the fragments between the first and the second stage of the spectrometer.

3.4.4 The isotopic identification

After selection of projectile fragments and proper charge state difference Δq, the isotopes can be clearly identified using the correlated position at S4 versus A/q ratio spectrum (see e.g. Fig. 3.10). Actually, the different "islands" represent different nuclides. Each island can be associated to one nuclide with definite A and Z. Each nuclide is identified on the basis

of its A/q ratio and, in case of fully stripped ions, on its position relative to the centered isotope. The nuclide association is verified by known γ-ray transitions in some isotopes.

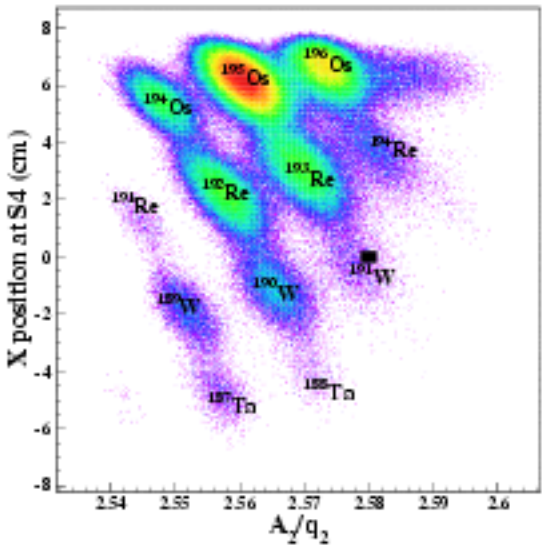

Figure 3.10: Dispersion of the different isotopes at the final focal plane after selecting a particular charge state difference (here, Δq=0 setting on ^{191}W). One can notice that ^{191}W which should be the central isotope is correctly centered with respect to x position and its mean A/q ratio is close to the calculated value of 2.58108

3.4.5 Charge state contaminants

Ambiguities in the magnetic analysis occur if the fragmentation products are not fully stripped. These fragments will appear at positions different from the fully ionized fragments of the same mass and nuclear charge, and they may overlap in position with other fragments. Therefore, each isotope ^{A}Z was contaminated by fragments $^{A-5}$(Z-1) which came through both stages of the FRS as H-like ions (q=Z-1 but Δq=0) and thus could not be separated from fully stripped ions. Although typically the production cross section for such a contaminant is larger than that of the isotope of interest by a factor of 5, only 2% of the contaminant is produced as a H-like ion. Finally, the contamination due to H-like ions amounted to less than 5%.

This fraction of incompletely stripped ions may complicate the isotopic identification of

the reaction products. In such cases, a new elaborate procedure, developed by J. Benlliure et al. [41], was used to identify the ionic-charge changing processes and secondary reactions.

The charge identification was provided by twofold energy-loss measurements.

First, the magnetic rigidities $B\rho_1$ and $B\rho_2$ in the two sections of the spectrometer were used to determine the quantity :

$$(\Delta E_{degrader}/q)_{nominal} = e[B\rho_1/\beta_1 - B\rho_2/\beta_2].$$

While β_2 is directly given by the measured time-of-flight, β_1 was deduced from $B\rho_1$ and A_2/q_2 by assuming A_1/q_1=A_2/q_2=A/q as determined by the formula :

$$\frac{A}{q} = B\rho_2\frac{e}{u\cdot\beta_2\cdot\gamma_2} = B\rho_1\frac{e}{u\cdot\beta_1\cdot\gamma_1}$$

Consequently, we found :

$$\beta_1 = \frac{c}{u}\cdot\frac{B\rho_1}{A_1/q_1} = \frac{c}{u}\cdot\frac{B\rho_1}{A/q}$$

and

$$(\Delta E_{degrader}/q) = u[\frac{A_1}{q_1}\cdot\gamma_1 - \frac{A_2}{q_2}\cdot\gamma_2] = u\cdot\frac{A}{q}[\gamma_1 - \gamma_2].$$

Second, the signal of the MUSIC chamber placed at the exit of the FRS was used. By combining this signal with the nominal energy loss in the intermediate degrader ($\Delta E_{degrader}/q$), incompletely stripped ions and secondary reactions in the layers of matter placed at the intermediate focal plane are discriminated as shown in Fig. 3.11. While the MUSIC provides a Z information with good resolution, the quantity $(\Delta E_{degrader}/q)_{nominal}$ is modified strongly if $q_1 \neq q_2$. But also fragments $^{A-5}$(Z-1) coming as H-like ions in both stages can be identified.

In Figure 3.11, the energy loss in the intermediate degrader is plotted versus the energy loss in the MUSIC chamber. While the band $0e^-$ corresponds to ions which pass the two sections of the FRS completely stripped, the ions in the two upper bands captured one or two electrons respectively and the ions in the lower band lost one electron in the intermediate focal plane. The weak side peaks shifted to lower ΔE_{MUSIC} values below the $0e^-$ band are generated by ions which traversed both sections of the FRS with one electron. Events in between and below these bands correspond to secondary reactions in the energy degrader.

This method was complementary of the method described in section 3.4.3 to select the different charge states. Most of the time, the charge state spectrum (section 3.4.3) is sufficient and this method was used during the final analysis in order to suppress as many contaminants

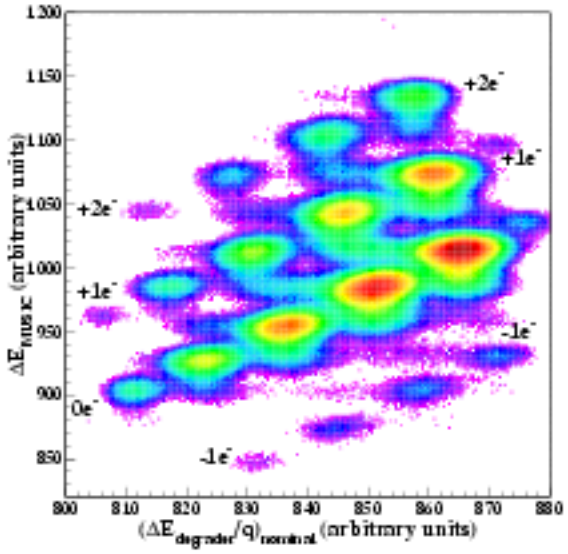

Figure 3.11: Two-dimensional plot of the energy loss in the intermediate degrader versus energy loss in the MUSIC chamber.

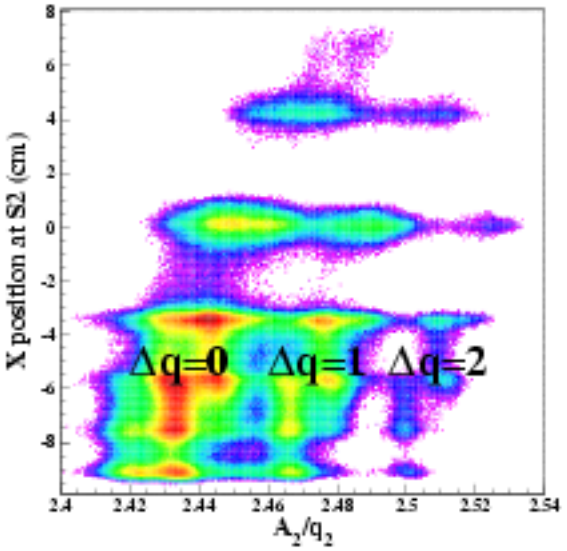

Figure 3.12: Two-dimensional plot of the A/q ratio in the second FRS stage versus position of fragment at S2 (^{180}Ta setting).

as possible and especially to get rid of fragments coming as H-like in both stages. However, in some cases, the charge state selection could not be done in a proper way and this procedure was thus of first importance to distinguish between charge states. The ^{180}Ta setting illustrates the difficulties of charge state selection (see Fig. 3.12). For this setting, the charge state spectrum is not sufficient to select accurately the different charge states and the energy loss spectrum is used instead (Fig. 3.11).

3.5 Gamma-ray spectroscopy of identified fragments

3.5.1 Prompt atomic background and gamma-ray multiplicity

As already mentioned (see section 2.4), the fragments reach the stopper with an energy of 50 to 100 Mev/nucleon. Consequently, they produce a large number of reactions in the catcher. Therefore, the main part of prompt gamma-ray background is mainly due to atomic reactions producing X-rays and bremsstrahlung as well as , for a minor part, to nuclear interactions, i.e. secondary fragmentation and Coulomb excitation taking place in the catcher. As a result, a large prompt gamma-ray background is observed with energy mainly between 0

and 200 keV.

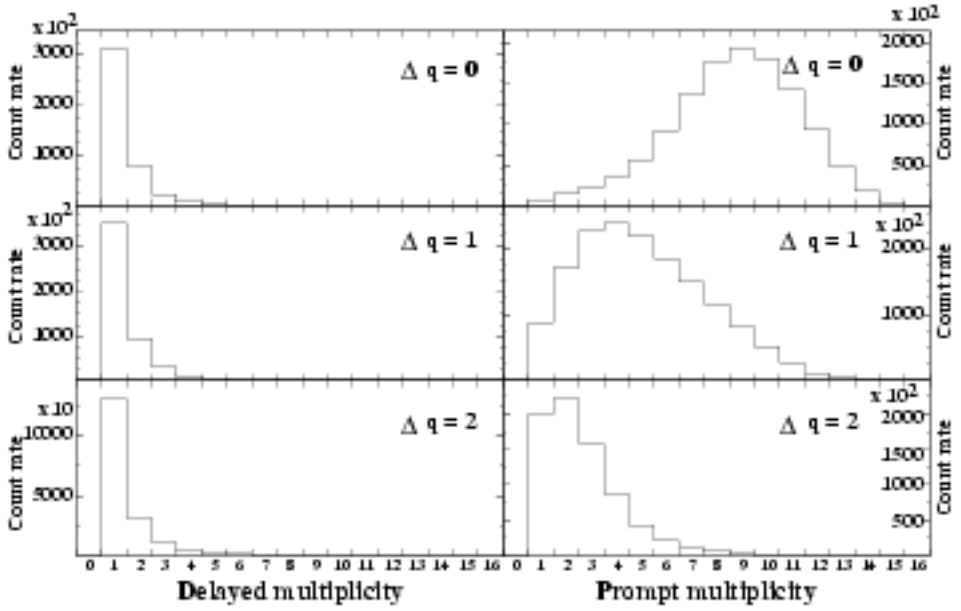

Figure 3.13: The prompt and delayed gamma-ray multiplicity is represented for fully stripped ions (Δq=0), H-like ions (Δq=1) and He-like ions (Δq=2).

The large number of reactions in the catcher gave rise to a large number of prompt gamma-rays. These gamma-rays were detected by the Ge-detectors and eventually blocked the corresponding detector acquisition until the next event (i.e. next fragment) happened. As a result, the prompt multiplicity of each event was very large (an average of 9 out of 16 detectors fired) whereas the multiplicity of delayed gamma-rays was assumed to be 1 (see Figure 3.13) and many delayed gamma-rays associated with isomers probably escaped the detection set-up. Therefore, the gamma-ray efficiency was also affected and reduced by a factor of 4. In addition, this problem made gamma-gamma coincidences study nearly impossible except for very short-lived isomers.

One can notice on figure 3.13 that the prompt multiplicity decreases when the charge state increases. This can be explained as follows : the fully stripped ions hit the catcher with a higher energy than that of the H-like and He-like ions and consequently they produce more prompt reactions and thus γ-rays. This effect is not related to the charge state itself but rather to the fragment mass. As a matter of fact, the velocity of the fragments decreases when their mass increases and they are much more slowed down in the different media they traversed. Consequently, the heavier fragments will hit the catcher with a lower energy and

will produce less γ-rays.

3.5.2 Delayed gamma-rays associated with identified fragments

The procedure used to analyse data coming from the Segmented Clover Array can be described as follows (see Fig. 3.15 as well). After selecting one nuclide, time-energy matrices in two different time ranges were plotted and some gamma-rays could be identified (see Fig. 3.14). The widening of the matrix in the low energy part ($E_\gamma \leq 200$ keV) reflects the high intensity, the time walk effect due to the larger intrinsic resolution at low energy (20 ns instead of 8 ns) and the reduced resolution of the detectors.

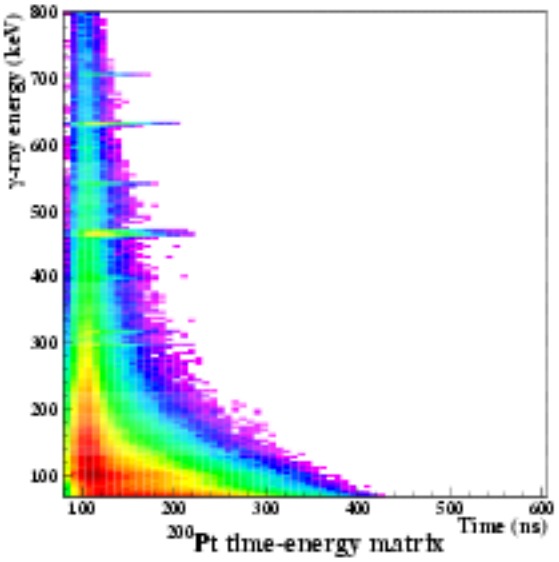

Figure 3.14: Typical time-energy matrix obtained during our experiment.

Then a time window is defined to select the isomeric decay and reduce as much as possible the gamma-ray background. The time-gamma matrix is projected corresponding to this time window along the energy axis and gives the gamma-ray energy spectrum. Random coincidences were neglected since the rate was kept below 1 kHz to avoid pile-up. Gamma-ray lines are selected and corresponding time decay is projected along the time axis within the chosen time window. In addition, background spectrum with the same number of channels as the γ-ray transition window is selected on the sides of the peaks and coresponding time decay curve is projected along the time axis within the previously defined time window.

Finally the decay time spectrum of background is substracted from the decay time spectrum of the γ-ray transitions and the resulting curve corresponds to the decay curve of the isomer. Isomer half-life can then be deduced by fitting this curve.

In principle, the gamma-ray analysis corresponds to the previously mentioned procedure. However, the time-gamma matrix is most of the time not sufficient to conclude about the presence of any isomeric decay due to too low count rates. In such cases, we can only apply different time windows and check the energy projection to see if gamma-ray lines can be seen. Thus the time window is chosen as large as possible with respect to the prompt peak and then reduced in order to get rid of the largest amount of background.

In summary, the analysis procedure can be described as follows. First of all, the fragments of interest are identified mainly according to their positions at each focal plane as well as to their A/q ratio in the second half of the spectrometer. Then they are selected and, from this selection, the gamma-spectroscopy information can be obtained for each fragment with a low probability of contamination by neighboring nuclides. The next chapter will develop the results obtained from the gamma-spectroscopic observations of a few nuclides from the ^{208}Pb fragmentation reaction.

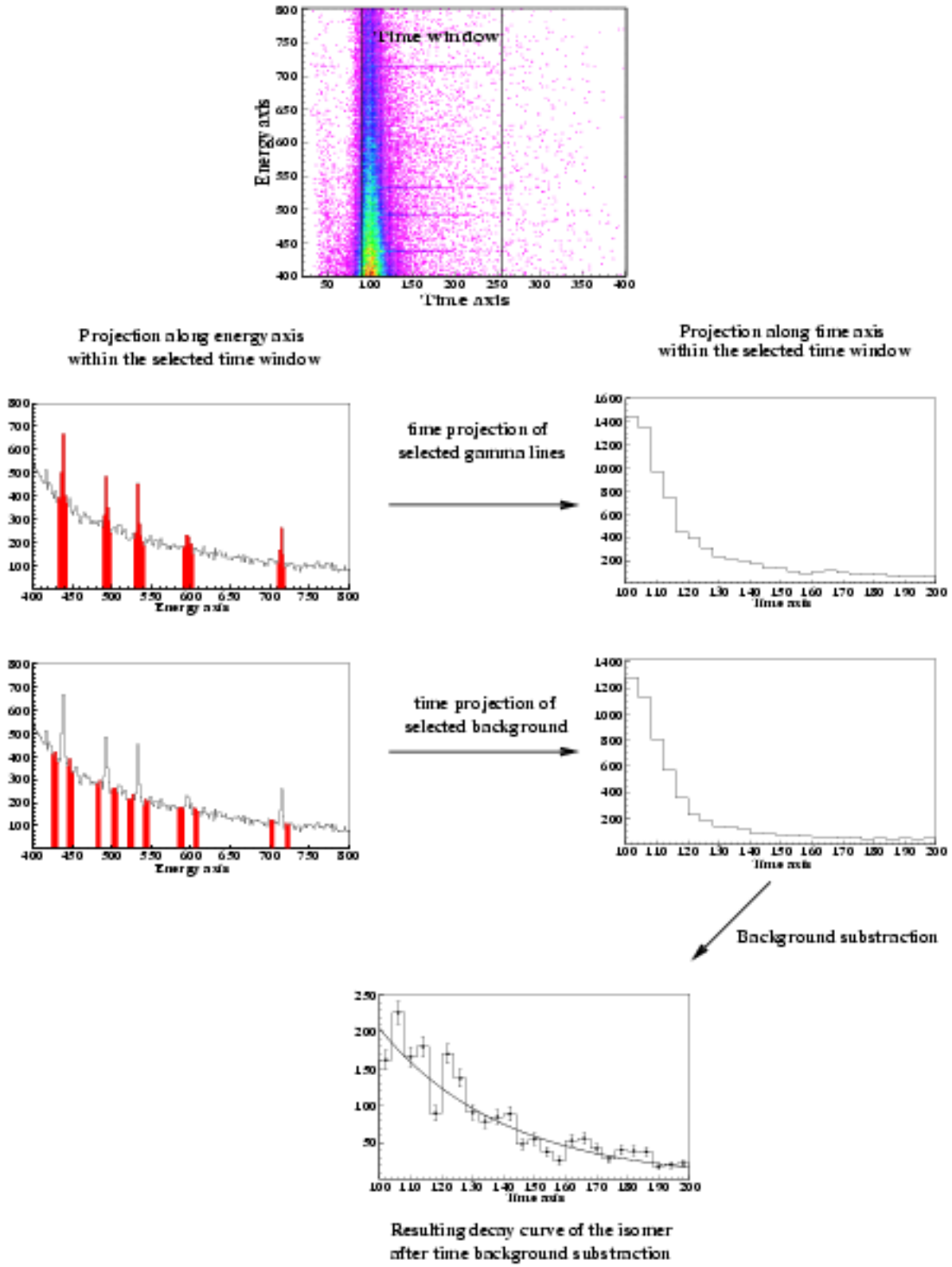

Figure 3.15: Procedure of gamma-ray analysis for lifetime determination (delayed γ-rays).

4 Results and interpretation

The spectroscopic results obtained from the experiment are detailed in this chapter.

4.1 Population of high spin states

The first main result of this experiment is related to the production of high angular momentum states via projectile fragmentation reactions. It has been mentioned in section 2.2.2 that the abrasion-ablation model describing the fragmentation process predicts population probability for different angular momentum states of the fragment.

Population probabilities are discussed in references [42, 43, 44] for the fragmentation of ^{92}Mo, ^{112}Sn and ^{86}Kr beams at energy of about 60 MeV/nucleon. For projectile energies above 100 MeV/nucleon, much less information is known. Prior to the current experiment, the only reported results are the isomeric ratios of a few μs isomers identified among the fragmentation products of a ^{238}U beam at 1 GeV/nucleon [45].

4.1.1 Method

By measuring the γ decays of selected well known fragments, one can calculate the experimental isomeric ratio and compare it to the predicted one. We define the isomeric ratio R by the ratio of the number of ions which have been produced in an isomeric state to the total number of ions created for a given isotope in the reaction. Hence known transitions have been observed in many nuclei and experimental isomeric ratios have been extracted. The method used to extract isomeric ratios from the experimental data are described in an exhaustive way by M. Pfützner et al. [46]. We try here to give a brief summary of this method. According to the definition, we have :

$$R = \frac{N^{isomer}(target)}{N^{ions}(target)}.$$

The total number of ions produced at the target $N^{ions}(target)$ as well as the number of ions produced in an isomeric state $N^{isomer}(target)$ are accessible from the experimental data measured at the final focal plane S4. Therefore the transmission from the target to S4 $T_{target-S4}$ and the in-flight decay of the isomer F have to be considered :

$$N^{ions}(target) = \frac{N^{ions}(S4)}{T_{target-S4}} ,$$

and in a similar expression taking into account the in-flight decay F:

$$N^{isomer}(target) = \frac{N^{isomer}(S4)}{T_{target-S4} \cdot F} .$$

Thus R can be written as :

$$R = \frac{N^{isomer}(target)}{N^{ions}(target)} = \frac{N^{isomer}(S4)}{F \cdot N^{ions}(S4)}$$

The factor F is calculated from :

$$F = exp\left[-\left(\lambda^{q1}\frac{TOF_1}{\gamma_1} + \lambda^{q2}\frac{TOF_2}{\gamma_2}\right)\right] ,$$

where TOF_1 (respectively TOF_2) is the time of flight through the first (respectively the second) stage of the FRS, γ_1 (respectively γ_2) is the corresponding Lorentz factor and λ^{q1} (respectively λ^{q2}) is the decay constant of the ion in the charge state q_1 (respectively q_2). Since only TOF_2 was measured in the experiment, TOF_1 and γ_1 were calculated with the ion-optical code MOCADI [47]. The number of ions at S4 $N^{ions}(S4)$ is obtained from the identification plot (see for example Figure 4.6). The number of ions in an isomeric state is determined from the number of counts in the γ-ray transition depopulating the isomer of interest. This number depends on the total conversion coefficient for this transition α_{tot}, on the efficiency of the Segmented Clover Array corrected for multiplicity ϵ_{eff} and on the absolute branching ratio of the transition considered b_γ. This dependence is expressed as follows :

$$N^{isomer}_{S4} = \frac{N_\gamma(1+\alpha_{tot})}{G \cdot \epsilon_{eff} b_\gamma}.$$

The correction factor G accounts for the finite time window of the γ-ray detection set-up and is equal to :

$$G = [exp(-\lambda t_i) - exp(-\lambda t_f)] ,$$

where t_i and t_f are the limits of the time window set in the off-line analysis to produce the γ-ray spectrum and λ is the decay constant of the neutral atom. Many other factors have

to be taken into account to calculate the isomeric ratio like the number of γ-ray transitions depopulating an isomeric state as well as the number of isomers in the same nucleus. As a result, the determination of the isomeric ratio is a rather complicated task. In this work, we have concentrated on results illustrating the ability of projectile fragmentation to populate high spin states.

4.1.2 Population of high spin states in the ^{177}Ta setting

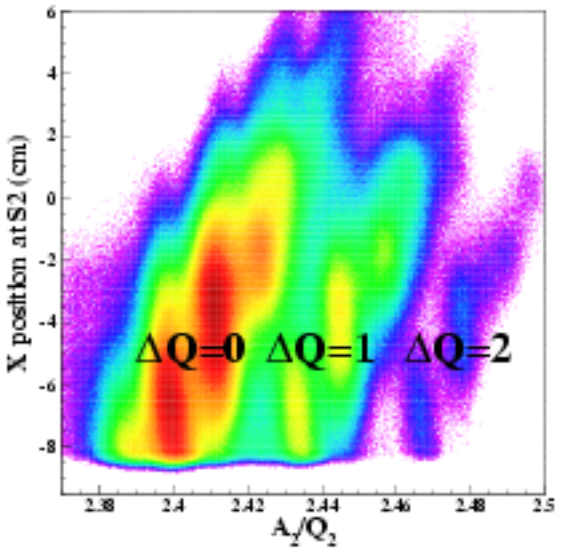

Figure 4.1: Different charge states of the ^{177}Ta setting.

One example for the population of a high-spin state is the known $K^{\pi}=35/2^{-}$ isomer with a half-life of 750 ns in ^{179}W previously measured by Walker et al. [48]. In the spectrum (Fig.4.2), γ transitions of the ground state band are seen up to the transition $31/2^{-} \rightarrow 27/2^{-}$. All observed γ-ray lines are shown in the partial level scheme in Fig. 4.2.

The feeding transition from the $K^{\pi}=35/2^{-}$ isomer into the $K^{\pi}=31/2^{-}$ state of the gs-band was observed at 610 keV. Beside this isomer, another state with $K^{\pi}=21/2^{+}$ and a half-life of 390 ns was populated. In contrast to the $K^{\pi}=35/2^{-}$ isomer, this state decays first to the $K^{\pi}=9/2^{+}$ side band and then to the ground state band. The observed intensities of the γ-ray lines originating from the decay of the $K^{\pi}=21/2^{+}$ isomer are significantly lower than these from the decay of the $K^{\pi}=35/2^{-}$. The decay from this isomer to the $I^{\pi}=17/2^{+}$

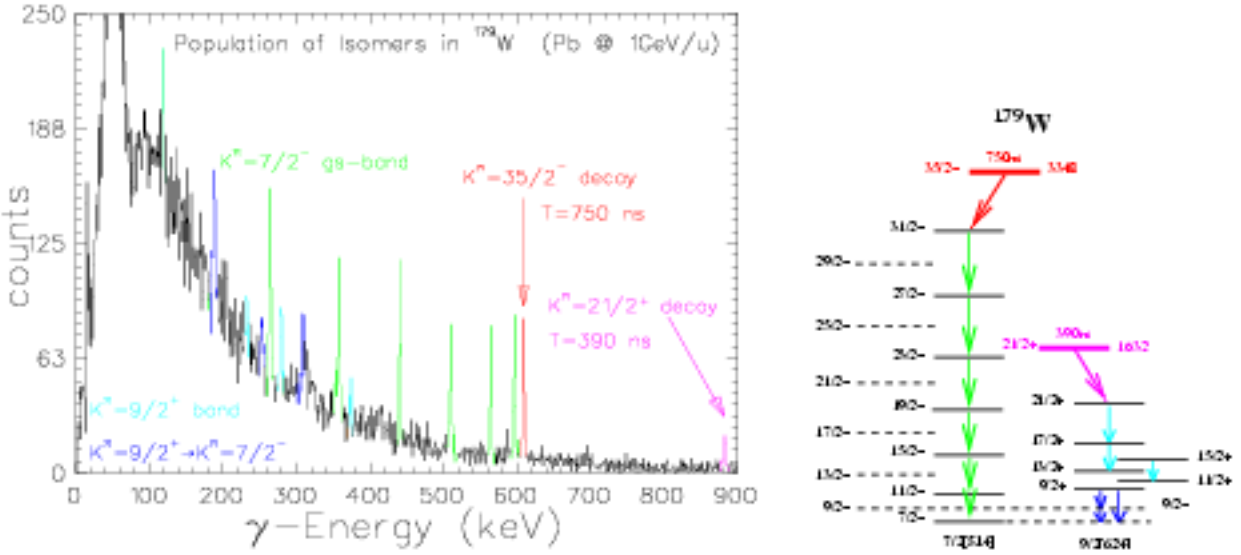

Figure 4.2: Gamma-ray spectrum of ^{179}W observed in this experiment (fragmentation of ^{208}Pb at 1 GeV/u) and partial level scheme of ^{179}W taken from [48].

state of the $K^{\pi}=9/2^{+}$ band is clearly seen in the spectrum at 884 keV. The $K^{\pi}=9/2^{+}$ band decays with a half-life of 1.6 ns to the gs-band. Due to this feeding one can observe the $9/2^{-} \rightarrow 7/2^{-}$ transition in the gs-band at 119 keV.

Figure 4.3 shows excitation energies as a function of the angular momentum for ^{179}W with known K-isomers taken from [48].

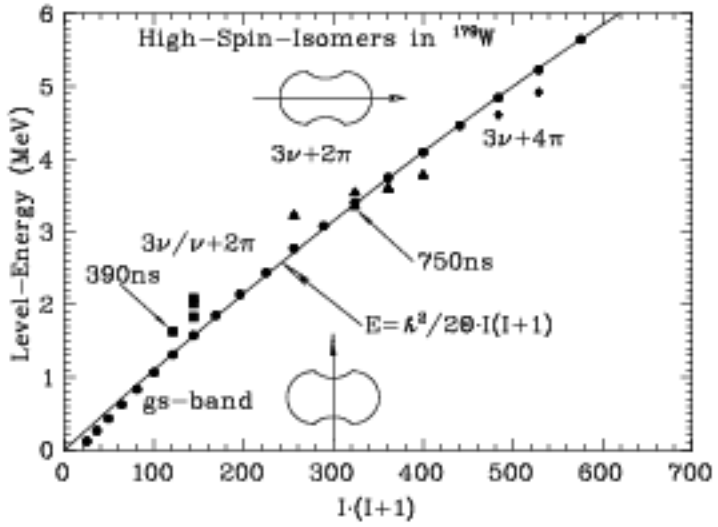

Figure 4.3: Ground state rotational band and known K-isomers in ^{179}W [48].

The ground state band collective states are given up to spin 47/2 $\hbar$. It should be noted that in the current experiment the ground state band was only observed up to the $35/2^-$-state since the population of an isomeric state was required to observe delayed γ-rays. The solid line shows a fit using the rigid rotor formula including the high spin levels. In addition all known quasiparticle isomers are shown. Transitions from isomers marked by arrows were observed in the experiment. The other isomers have half-lifes which are outside the time range observable in this experiment.

From the distribution shown in Fig. 4.4, a population probability for a spin of $\frac{21}{2}\hbar$ and $\frac{35}{2}\hbar$ is predicted to be 25.7% and 2.4%, respectively. Actually, assuming that these spin states are fed from all states with higher spin, one obtains this probability by integrating the angular momentum distribution (given in section 2.2.2) over angular momenta greater than $\frac{21}{2}\hbar$ and $\frac{35}{2}\hbar$ respectively. In the experiment, we obtain a ratio of 2.7(5)% for the

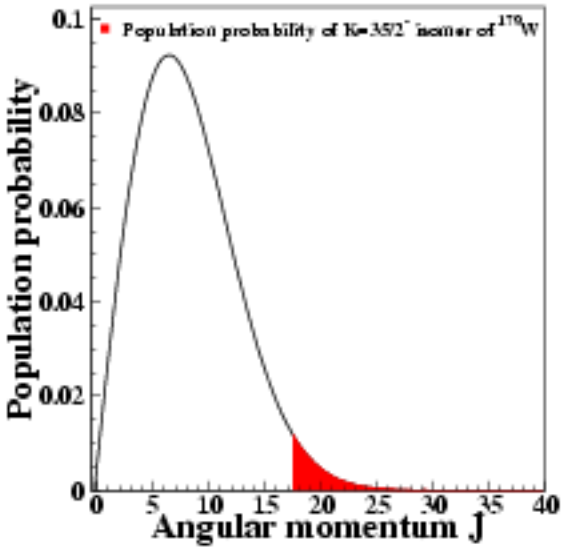

Figure 4.4: Distribution of the angular momentum which can be populated in a fragmentation process for the case of ^{179}W (using the prescription outlined in [31]).

$K^\pi=35/2^-$ isomer, which indicates that this isomer was populated in the expected ratio of 2.4%. The explanation is the yrast location of the $K^\pi=35/2^-$ state. It therefore acts as an yrast trap which is fed from all states with higher spin. The $K^\pi=21/2^+$ state in contrast to the $K^\pi=35/2^-$ isomer has an experimental ratio of 6(1)%, which is only a quarter of the predicted value of 25.7%. The reason is that the $K^\pi=21/2^+$ state is not yrast but lies by

509 keV above the yrast line. Therefore it is not fed so significantly by higher spin states and do not collect the full population flux.
In addition to these two isomers observed in ^{179}W, other isomeric states are populated by fragmentation of a ^{208}Pb beam in nuclei with mass ranging from A=136 to A=206. Corresponding isomeric ratios have been measured [46]. These isomers cover a wide range of angular momenta (from $\frac{5}{2}\hbar$ to $\frac{35}{2}\hbar$, see reference [46]) and the measurement results show that the theoretical predictions of the abrasion-ablation model correspond to an upper limit for the measured isomeric ratios.

4.2 New spectroscopic observations

Using several exotic settings of the FRS a number of new isotopes in the mass 180-200 region were discovered. The main observations outlined in the following sections have been obtained from one magnetic rigidity setting optimised to select fully stripped nuclei centred on ^{191}W. These observations are summarized in table 4.1. Some of these new isomers, namely ^{201,202}Pt, are not discussed here and will be found in reference [56].

Nuclide	^{190}W	^{192}Re	^{193}Re	^{196}Os	
Half-life	$390^{52}_{266}\,\mu$s	120.1(63.9) μs	86.3(69.8) μs	37.1(5.2) ns	
Δq	0	0	0	0	
Nuclide	^{197}Ir	^{198}Ir	^{201}Pt	^{202}Pt	^{203}Au
Half-life	34.4(7.6) μs	82.9(3.4) ns	22.3(0.3) ns	53(38) μs	64.9(53.4) μs
Δq	1	1	1	1	2

Table 4.1: New isomers observed in the ^{191}W setting.

Because the magnetic rigidity setting on ^{191}W was located quite close to the beam, the intensities of the different charge states are quite similar ($I_{\Delta q=0} = 31\%, I_{\Delta q=1} = 43\%, I_{\Delta q=2} = 26\%$, Fig. 4.5) . In fact, the production cross-sections at the primary target of the fragments seen as Δq=1 and Δq=2 fragments in the second half of the spectrometer are much higher than those of the Δq=0 fragments so that, even if the transmission of those fragments is low in the second half of the FRS, a large number of such fragments is still selected and can compete with the fully stripped fragments.

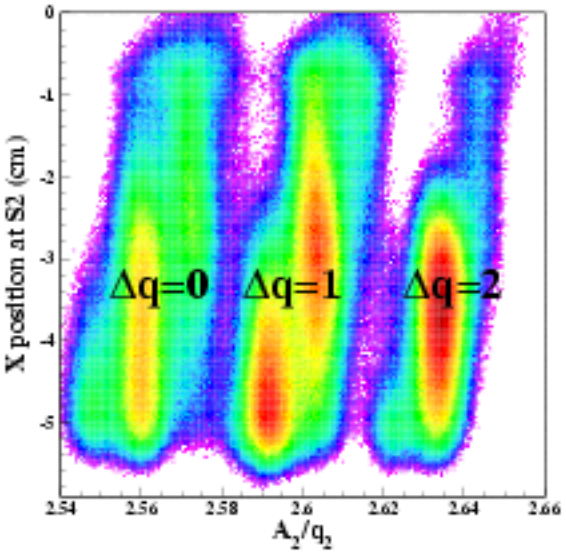

Figure 4.5: Different charge states of the ^{191}W setting.

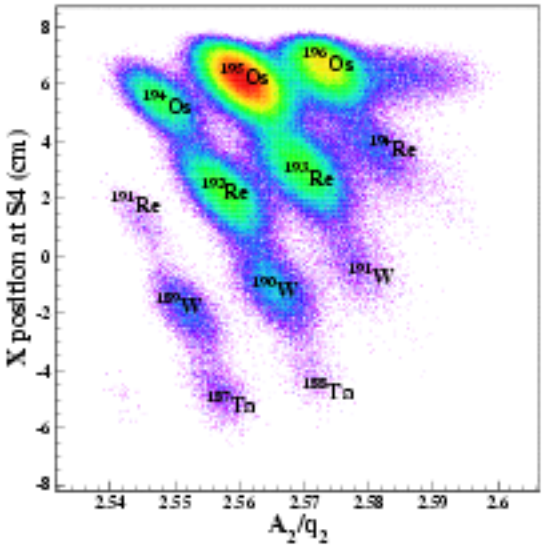

Figure 4.6: Identification plot of the Δq=0 fragments of the ^{191}W setting.

4.2.1 Fully stripped fragments

- ^{190}W

The population of the previously unknown ground state band in ^{190}W is shown in Fig.4.7. The results obtained from this experiment for this nucleus have been recently published: Zs. Podolyák et al. [49]. Let us summarize the observed level scheme.

Five γ-rays have been observed and have the same intensity when corrected for detection efficiency. The systematics of this deformed region conforted by the identical intensities measured for these transitions strongly suggest that these γ-rays form a rotational cascade, built on the ground-state of ^{190}W (see Fig. 4.7). The mean lifetime for the isomeric state was determined to be $\tau = 390^{\infty}_{200}\mu$s. An upper limit of 4.5 ms for the mean lifetime can be obtained from the absolute γ-ray intensities, assuming that all the ^{190}W nuclei are produced in the isomeric state. A ground-state deformation of β_2=0.17 has been estimated based on the energy of the 2^+ yrast state [50]. A simple analysis of the ground state band using the Harris parametrisation [51] cannot reproduce the proposed level ordering. ^{190}W seems not to be a prolate rotor like ^{182}W but rather shows some degree of triaxiality. From our data, we cannot distinguish between γ-soft and γ-rigid behaviour. The proposed level scheme of ^{190}W is consistent with the level-energy systematics of the lighter W-isotopes. If the level energies

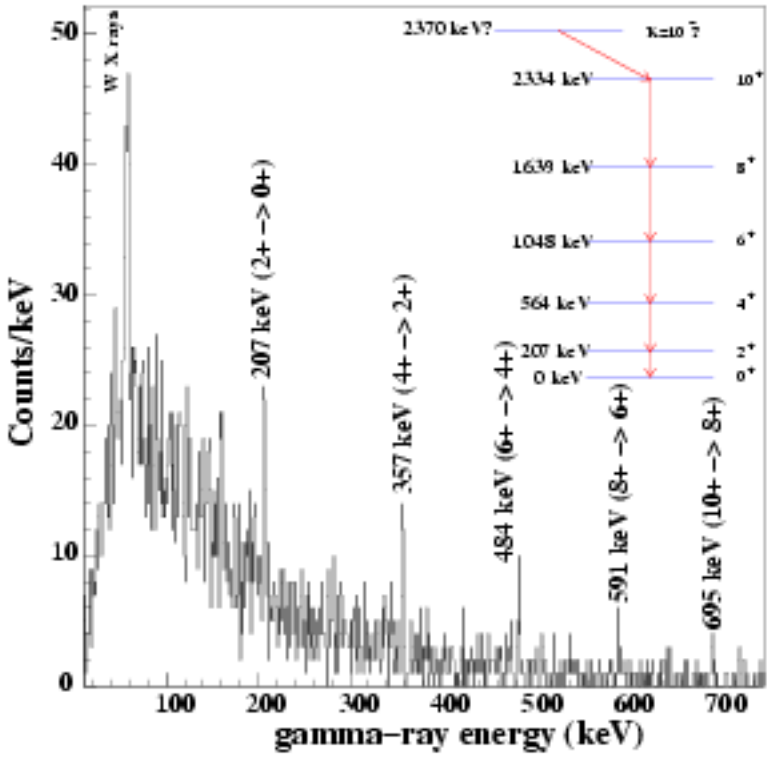

Figure 4.7: Gamma-ray spectrum of ^{190}W.

are normalized to the 2^+ energy, a strong deviation from the I·(I+1) law is observed (Fig.4.8) for light and heavy W isotopes. The deviation at the neutron rich side is quite dramatic. For the 6^+ and the 8^+ gs-levels of ^{188}W energies are taken from [52] although the spins of these levels are still not definitely assigned. If we compare the behaviour of the first excited 2^+ states with other isotopic chains (Hg, Pt and Os chains in Fig.4.9), we note a sharp increase of the energy of 2^+ W state on the n-rich side, which is more gradual for the Os-isotopes but comparable with the Pt-chain behaviour. Using the triaxial rotor model (see section 1.1.1) we can see (Fig.4.10) that ^{190}W behaves like a γ-deformed rotor. The normalized level energies observed are compatible with the theoretical sequence calculated for a γ=30° triaxiality factor. In contrast, ^{186}W corresponds to a weak triaxial deformation ($\gamma \approx 15°$). In terms of the interacting boson model, the limit $\gamma = 30°$ corresponds to the limiting case of the O(6) symmetry. So far, only in ^{196}Pt [16] this symmetry has been recognized explicitely.

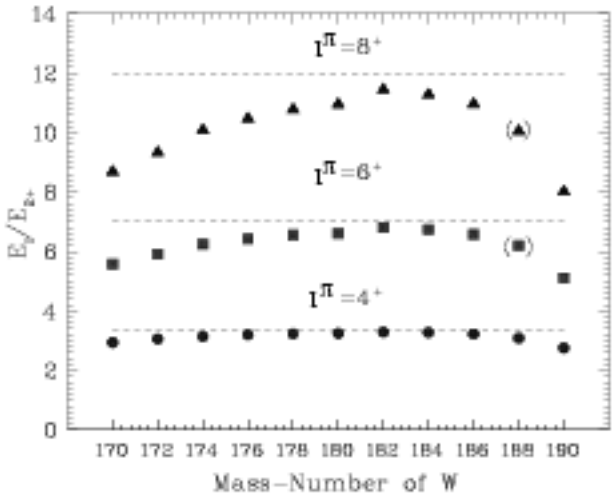

Figure 4.8: Level-energies of the W isotopes normalized to the 2^+ gs level.

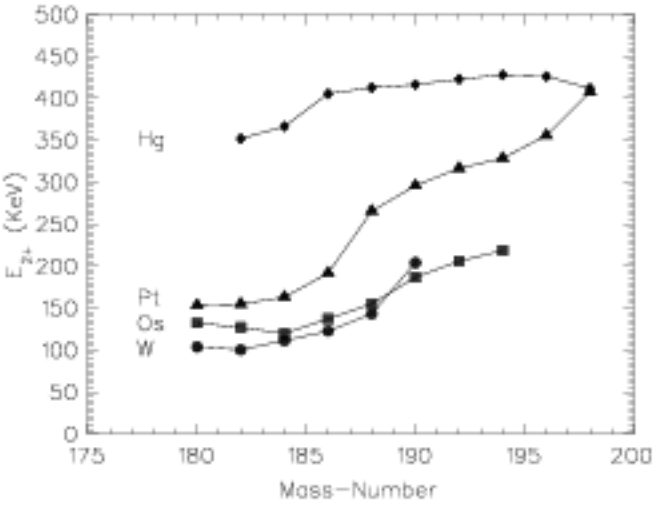

Figure 4.9: 2^+ level-energies versus mass number for W, Os, Pt and Hg isotopes.

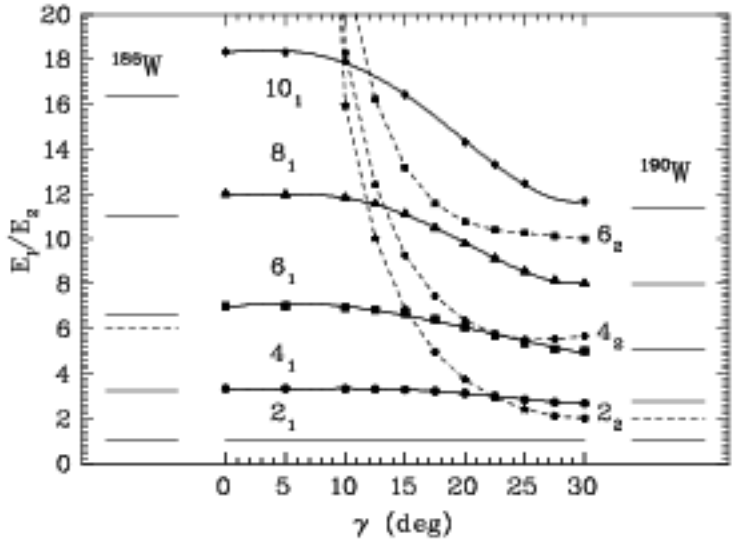

Figure 4.10: Normalized gs-level energies as a function of the triaxial deformation parameter γ in comparison with the level schemes of ^{186}W and ^{190}W.

• **Re isotopes**

Prior to this work, no spectroscopic information were known for ^{192,193}Re nuclei. In odd-odd ^{192}Re, a γ-ray line was observed at 159.4 $\pm$ 1.4 keV with a half-life of 120.1 $\pm$ 63.9 μs. In odd-even ^{193}Re, a γ-ray line was observed at 145.0 $\pm$ 1.0 keV with a half-life of 86.3 $\pm$ 69.8 μs. In both cases, K_α and K_β X-rays are clearly seen. X-rays are even more prominent in ^{193}Re than in ^{192}Re. Looking at neighboring Re isotopes, we can try to interpret these observations.

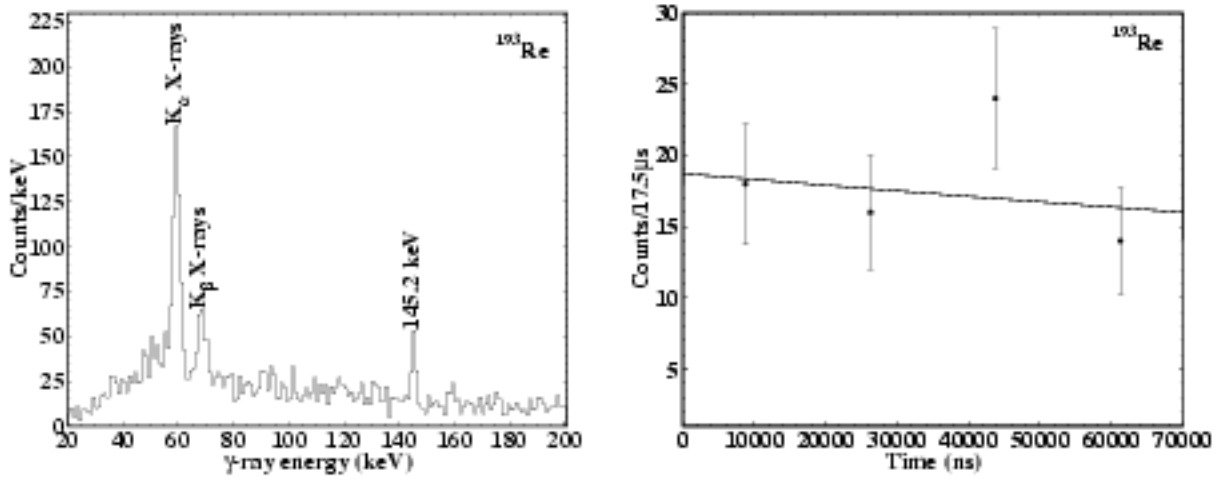

Figure 4.11: Gamma-ray spectrum of ^{193}Re and corresponding decay time spectrum.

In the case of odd-even Re isotopes, no γ-rays were observed in ^{191}Re and the level structure was obtained from transfer reactions. In particular, a $9/2^-[514]$ band whose $9/2^-$ bandhead is located 145 keV above the ground state was determined. This bandhead is located 125 keV above the ground state in ^{189}Re and 206 keV above ground state in ^{187}Re. In the latter nucleus, two γ decay branches have already been observed from the $9/2^-$ state to the ground state band : one decay of 72 keV γ-ray energy from the $9/2^-$ state to the $7/2^+$ first excited state and one decay from the $9/2^-$ state to the $5/2^+$ ground state with a half-life of 555.3 ns (see Fig. 4.12). Furthermore, the ground state bands of ^{187,189}Re have a $5/2^+[402]$ configuration while the ground state band of ^{191}Re was found to have a $1/2^+[411]$ configuration and a ground state spin-parity of either $3/2^+$ or $1/2^+$. Therefore, we suggest that the transition observed in ^{193}Re (see Fig. 4.11) may be similar to the one observed in ^{187}Re, e. g. the $9/2^-$ state located at 145.0 $\pm$ 1.0 keV above the ground-state decays with a

half-life of 86.3 ± 63.9 μs to the ground-state. In addition, the half-life which is longer than the one observed in ^{187}Re could be explained by having a $1/2^+[411]$ configuration for the ground state band with a particular spin-parity of either $3/2^+$ or $1/2^+$ for the ground state. We also suggest that the isomeric state may decay to an intermediate level which then decay to the ground-state. This low energy transition would be highly converted and this would explain why X-rays can be clearly seen in the γ-decay spectrum. Thus the isomeric state would be located at an excitation energy of 145(1)+x keV above the ground-state as shown in Fig. 4.12.

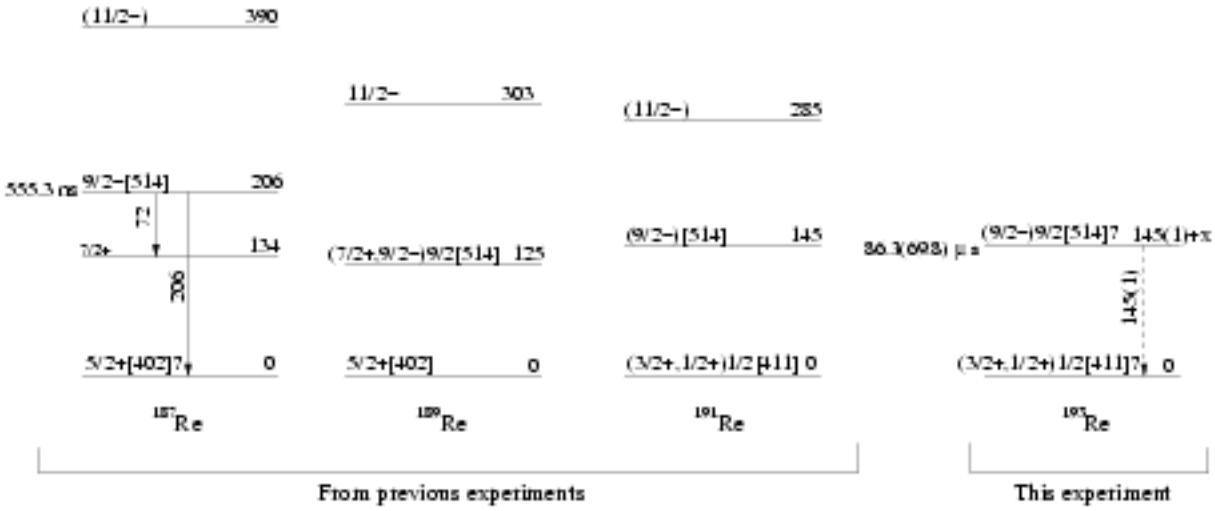

Figure 4.12: Systematics of the level structure from different odd-even Re isotopes leading to the proposed configuration of the isomeric state observed in ^{193}Re during the current experiment.

In the case of odd-odd Re nuclei, depending on the isotope, different configurations and level structures have been proposed. In these nuclei, the single proton and neutron interact with each other and it is rather difficult to explain our observations. For example, in ^{190}Re [53], an isomeric state with a half-life of 3.2 hours has been proposed with a spin-parity of 6^- by similarity with ^{188}Re [54] where a 6^- isomeric state with a half-life of 18.6 m has been identified at an excitation energy of 172 keV. As well, in ^{194}Ir [55] (which has the same number of neutrons as ^{192}Re but 2 additional protons), an isomeric state with a half-life of 31.85 ms has been proposed at an excitation energy of at least 112.3 keV whereas the spin-parity has not been clearly identified (spin : 4, 5 or 6 - parity : unknown). Therefore the isomeric γ decay we observe (see Fig. 4.13) is located at an excitation energy of at

least 159.4 ± 1.4 keV and has a half-life of 120.1 ± 63.9 μs. We suggest that its spin-parity is possibly 6^- similar to ^{188}Re. With the same argument used for ^{193}Re, we propose the possible existence of an intermediate state between the isomer and the ground state which would explain the observation of strong K_α and K_β X-rays.

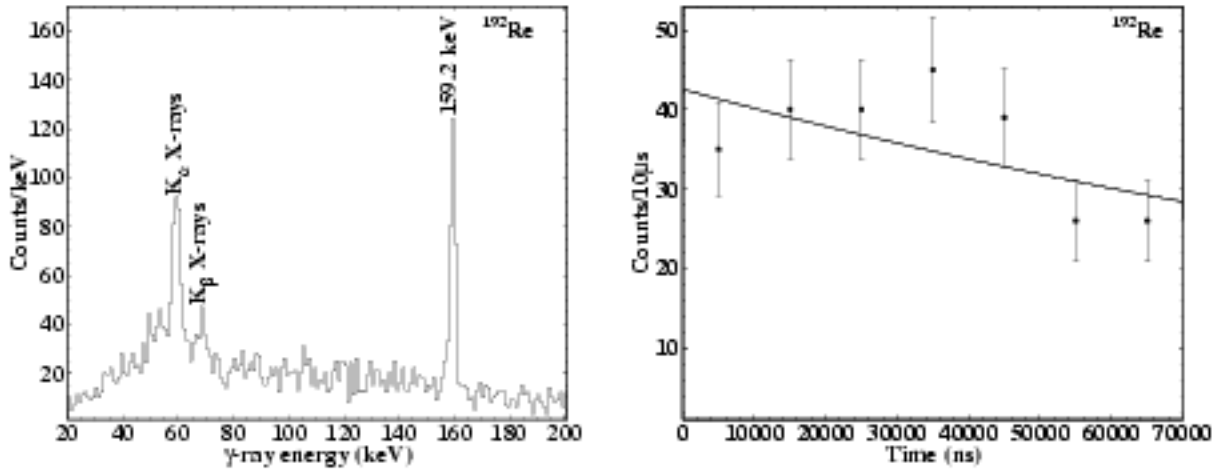

Figure 4.13: Gamma-ray spectrum of ^{192}Re and corresponding decay time spectrum.

- **^{196}Os**

A short-lived isomer whose half-life is 37.1 ± 5.2 ns has been observed in even-odd ^{196}Os. In neighboring nuclei, no isomeric states at high excitation energy have ever been observed in this region within the same time range. However, we suggest that the short-lived isomer decays to the ground-state band through collective excited states as observed in the γ-ray spectrum for ^{195}Os nucleus (see Fig. 4.14). Details can be found in reference [56].

4.2.2 Hydrogen-like fragments

A gate on ^{200}Pt projected on the time-γ matrix (see Fig. 4.16) confirms the identification of H-like fragments. Actually a previously reported 7^- isomer [57] with half-life of 14.3 ns has been observed. Such a short-lived state should not be observed in this experiment since its half-life is much shorter than the time of flight through the spectrometer (about 300 ns). We propose that it does survive because the transition energy from the isomeric state to the lower 5^- state is smaller than the K-shell binding energy in platinum (78 keV).

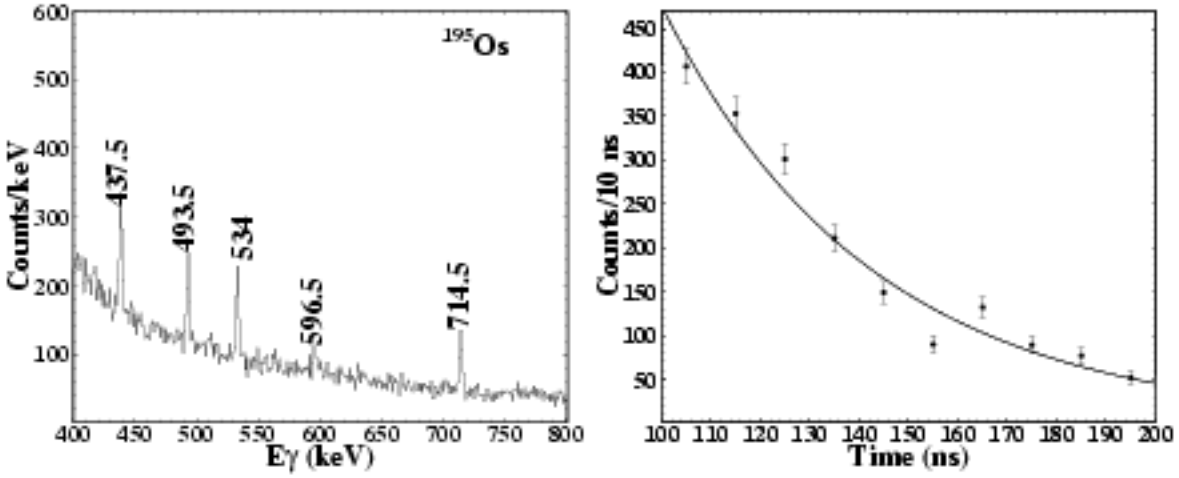

Figure 4.14: Gamma-ray spectrum of ^{195}Os and decay time of ^{195}Os.

Thus it is only when the fragment is implanted in the catcher that the isomeric state can be depopulated by electron conversion and attain its natural atomic half-life.

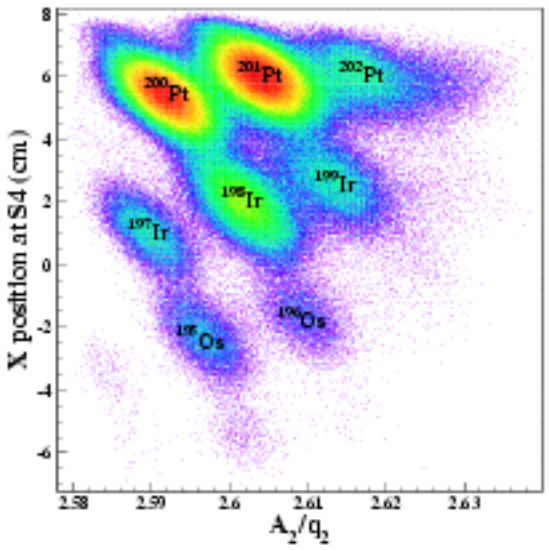

Figure 4.15: Identification plot of the ΔQ=1 fragments of the ^{191}W setting.

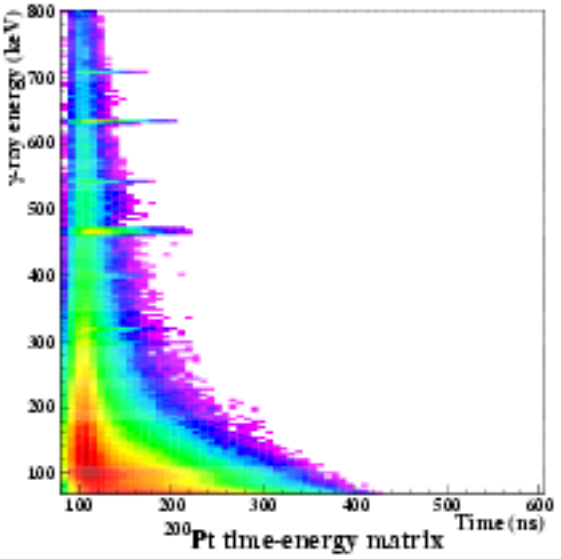

Figure 4.16: Time-γ matrix obtained by a gate on ^{200}Pt.

• Ir isotopes

The first spectroscopic information about ^{197}Ir was obtained by J. Cizewski et al. in 1982 [58]. This work allowed to determine the level structure of low-lying states up to 1 MeV in this nucleus. The interacting boson fermion model [13] was tentatively used to explain the

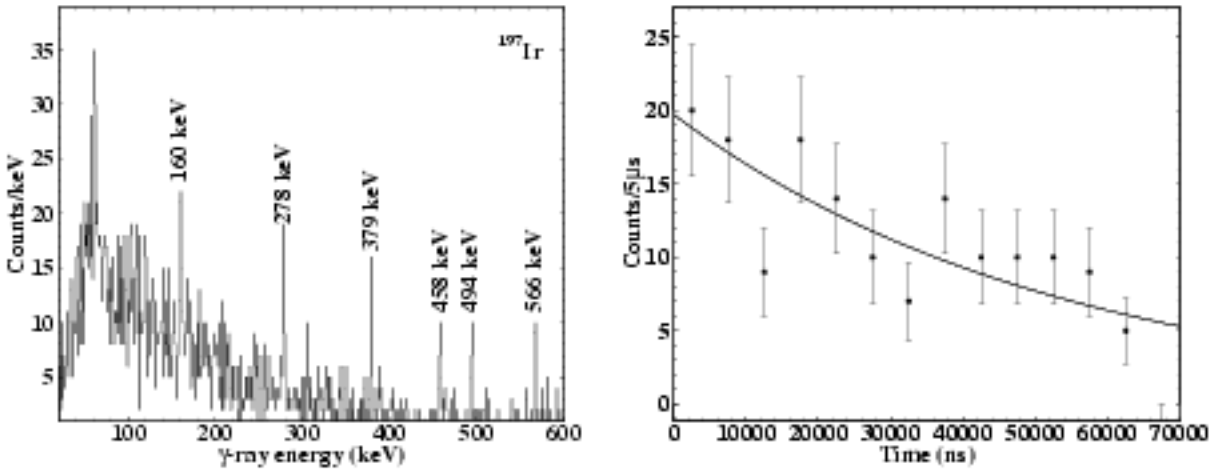

Figure 4.17: Gamma-ray spectrum of ^{197}Ir and corresponding decay time spectrum.

structure of ^{193,195,197}Ir. If this model encountered some success in explaining the structure of ^{193}Ir, it failed in reproducing correctly the structure of ^{195,197}Ir. Considering the case of ^{197}Ir, it was found that the ground state has a spin-parity of $3/2^+$, the first excited state at 52(5) keV a spin-parity of $1/2^+$ and the second excited state at 115(5) keV a spin-parity of $11/2^-$. In addition, a previous work [59] allowed to determine that this $11/2^-$ state is isomeric and decays preferentially by β decay. It decays also by a M4 transition to the $3/2^+$ ground state with a half-life of 8.9 min. The ground state configuration of ^{197}Ir was considered to be $3/2^+[402]$ similarly to ^{193,195}Ir [58]. Using this configuration, it is not possible to reproduce correctly the level structure of ^{197}Ir using the Nilsson model. A calculation based on the Nilsson model using the configuration $3/2^+[501]$ as the ground state and a parameter of deformation β_2=0.26 managed to reproduce correctly the level structure of ^{197}Ir as it was observed by J. Cizewski et al.. In particular, such a configuration would explain why the $11/2^-$ state comes so close to the ground state, since configurations with smaller deformations do not reproduce the correct ordering of the levels. Actually, a similar calculation using the $3/2^+[402]$ state as the ground state placed the $11/2^-[505]$ state at the same energy or even

below the $3/2^+[402]$ ground state. Therefore we suggest that the $3/2^+$ ground state of ^{197}Ir is not a pure $3/2^+[402]$ configuration but rather a mixture of different $3/2^+$ configurations.

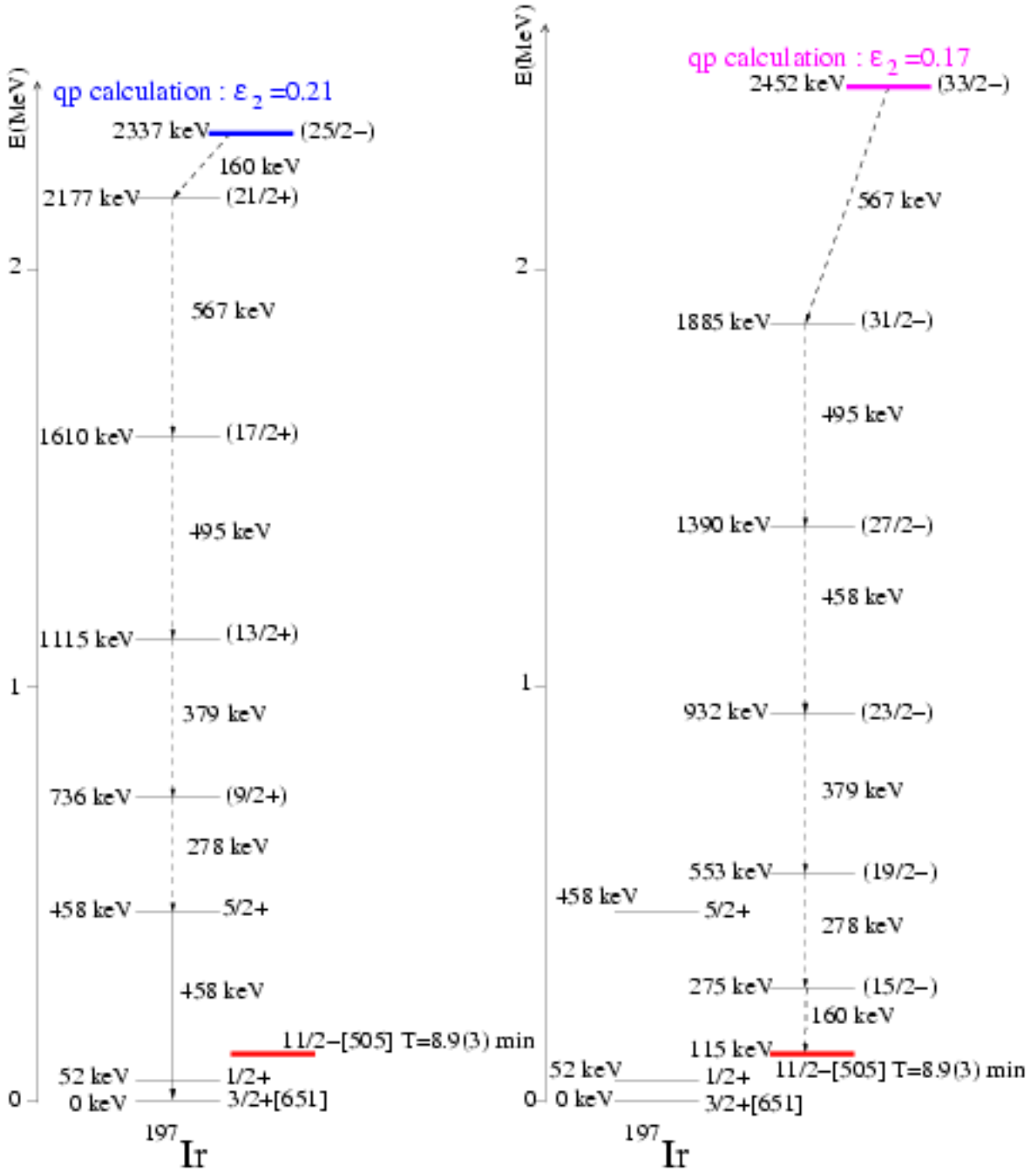

Figure 4.18: Proposed level schemes and possible isomeric states as they are given by blocked BCS multi quasiparticle calculations.

No further spectroscopic study was done on ^{197}Ir since 1982 and our experiment achieved the first observation of γ-ray transitions of ^{197}Ir.

Hence, ^{197}Ir exhibits a newly observed isomer with a half-life of 34.4 ± 7.6 μs decaying into six γ-ray transitions which can be interpreted as follows.

We propose that the six observed lines could be members of a rotational cascade located above either the $11/2^-[505]$ state or the $5/2^+$ state of the ground-state band (see proposed level schemes in Fig 4.18). Actually, the intensities, corrected for position and conversion electron, are equal within the statistical errors. However, the actual ordering of the levels can not be determined from this experiment. A measurement of the isomeric ratio gives a value of 1.2(4)% depending on the energy and on the multipolarity of the transition feeding the rotational band. This value is very small and strongly suggests that the state feeding the cascade is a high spin state.

Therefore the newly observed isomer could be a broken pair of neutrons, probably $i_{13/2} \otimes h_{9/2}$ on top of the 11/2 proton state. This isomer then may decay through collective states - corresponding to the observed γ-rays - built on the $11/2^-$ state. A blocked BCS quasiparticle calculation [60] using a deformation parameter ϵ_2 of 0.17 shows a $33/2^+$ isomer at 2.2 MeV above the ground-state, corresponding to a broken neutron pair of $i_{13/2} \otimes h_{9/2}$ coupled to the $11/2^-$ proton. The $i_{13/2}$ orbital contributes 13/2 from the 13/2[606] orbit while the $h_{9/2}$ contributes 9/2 from the 9/2[505] orbit. Considering that the two neutrons and the proton are fully aligned : $13/2 + 9/2 = 11$ and 11 (2 neutrons) + 11/2 (one proton) = 33/2.

At larger deformation (ϵ_2=0.21), other configurations still built on $11/2^-$ state are found in addition at excitation energies of 1.8 to 2 MeV as shown in Fig. 4.19.

Another possibility is a configuration built on the $3/2^+$ positive parity state. Since the 458 keV transition, observed in this experiment, may be the transition from the $5/2^+$ excited state to the $3/2^+$ ground state, observed in reference [58], the cascade may come from a high spin isomeric state above the ground-state. A quasiparticle calculation [60] using a deformation parameter ϵ_2 of 0.21 shows a $25/2^-$ isomer at 2.5 MeV above the ground-state, corresponding to a broken neutron pair of $i_{13/2} \otimes h_{9/2}$ coupled to the $5/2^+$ proton. The $i_{13/2}$ orbital contributes 11/2 from the 11/2[615] orbit while the $h_{9/2}$ contributes 9/2 from the 9/2[505] orbit. Considering that the two neutrons and the proton are fully aligned : $11/2 + 9/2 = 10$ and 10 (2 neutrons) + 5/2 (one proton) = 25/2.

Though excitation energies can be wrong by a few hundreds of keV, configurations with three quasiparticles are strongly favoured. On the contrary, a configuration with one quasi-

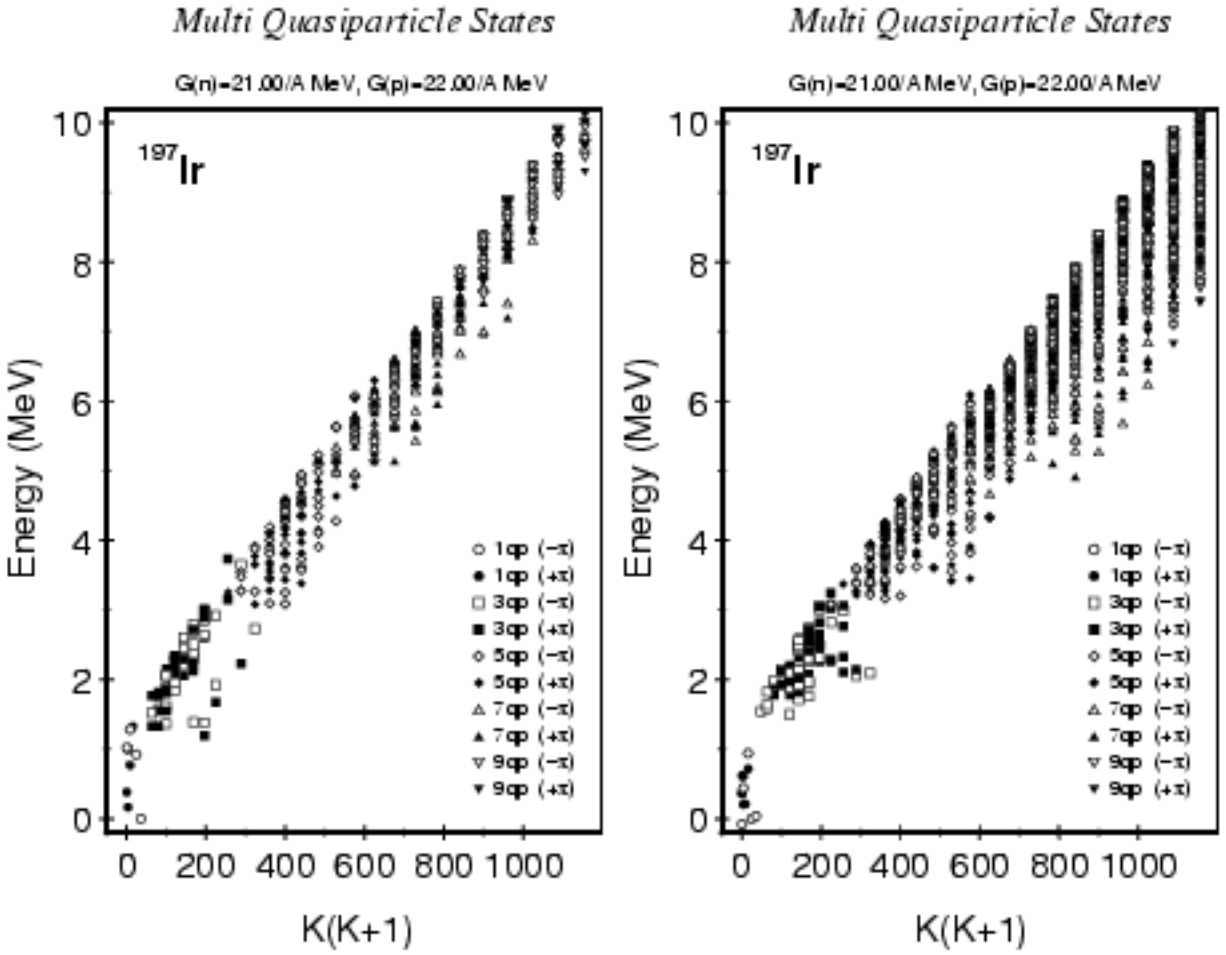

Figure 4.19: Multi quasi-particles states calculated for two different deformation parameters for ^{197}Ir: ϵ_2=0.17 (left) and ϵ_2=0.2 (right).

particle is quite improbable since such states are observed at both low energy and low spin. Therefore such configurations could not possibly produce the observed γ-ray transitions.

One transition is still under question : it is the 458 keV transition. We know from previous work [58] that ^{197}Ir exhibits a $5/2^+$ excited state at 460(5) keV above the ground-state. Furthermore, the decay curve of this transition gives a half-life of 19.1 $\pm$ 6.1 μs. It indicates that this transition may be fed from a different isomer. However, due to the low statistics, this result is within the experimental errors and can as well be part of the cascade described above. Consequently, the 458 keV transition is placed either at 458 keV above the ground-state or in the γ-ray cascade, as shown in Fig. 4.18.

Unfortunately, without γ-ray coincidences data, it is difficult to assign firmly this transition sequence. Theoretical calculations could, however, help to confirm these results.

Due to the lack of information in this region - the nearest neighbors are more or less unknown from a nuclear structure point of view -, it seems extremely difficult to interprete without any other information. Thus more detailed theoretical studies and the information from γ transitions in coincidence are necessary for further investigation.

A short-lived isomer has also been observed in ^{198}Ir. One γ-decay transition of 115.4 $\pm$ 1.4 keV was seen. A half-life of 82.9 $\pm$ 3.4 ns has been deduced from the corresponding decay curve. In neighboring nuclei, no isomers were observed in a similar time range. Only isomers with half-life between 241 y (^{192}Ir [61]) and 13.6 s (^{199}Pt [62]) have been found.

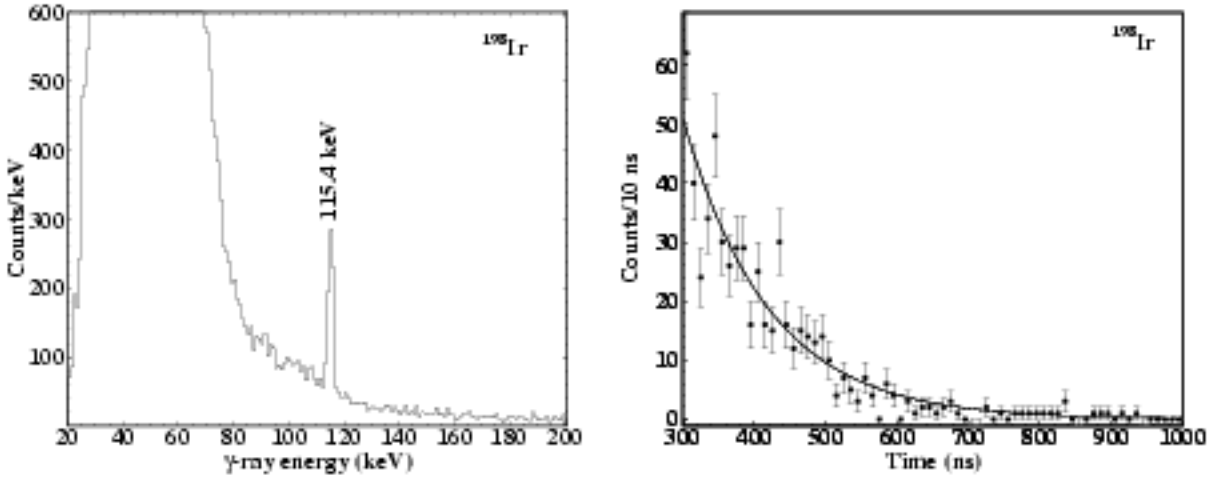

Figure 4.20: Gamma-ray spectrum of ^{198}Ir and corresponding decay time spectrum.

4.2.3 Helium-like fragments

A gate on ^{206}Hg projected on the γ-ray energy confirms the identification of He-like fragments. Actually, the projection of γ-ray energy within a time gate from 500 ns to 8 μs (see Fig. 4.22) shows the decay of the previously reported 2.15 μs $K^{\pi}=5^{-}$ isomer to the ground-state through two known γ-ray transitions : the 1034.0 keV γ-ray transition from the 5^{-} state to the 2^{+} state and the 1068.5 keV transition from the 2^{+} state to the 0^{+} ground state.

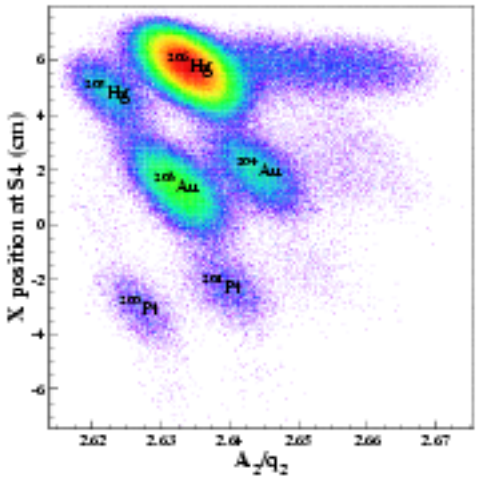

Figure 4.21: Identification plot of the $\Delta q=2$ fragments of the ^{191}W setting.

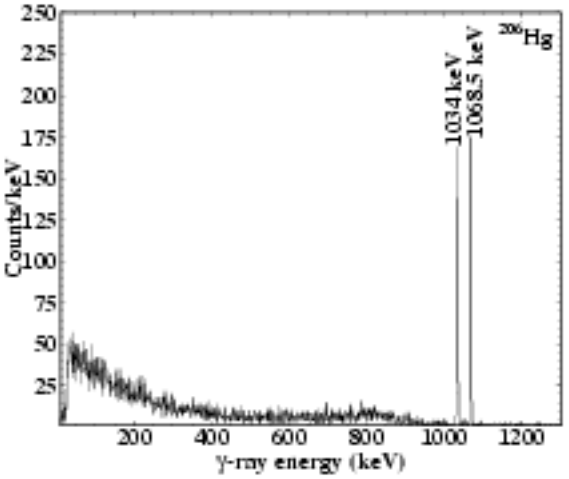

Figure 4.22: Gamma-ray spectrum of ^{206}Hg.

- ^{203}Au

One γ-ray transition has been clearly identified at 564.0 $\pm$ 2.0 keV. An isomeric state with a half-life of 64.9 $\pm$ 53.4 μs has been deduced. In neighboring odd-even Au nuclei (see Fig. 4.24), a $11/2^-$ isomeric state has been observed with half-life varying from 30.5 s in ^{195}Au [63] to 0.44 ms in ^{199}Au [62]. A state with spin-parity $11/2^-$ has also been observed in ^{201}Au [64] but its half-life has not been determined. Thus we suggest the observed transition corresponds to the decay of the $11/2^-$ isomeric state measured in neighboring Au isotopes and located at an energy of at least 564(2) keV above the ground-state. Due to the persisting γ-ray background at low energy, we also suggest that the isomer may decay to the ground-state through an intermediate state by a low energy transition.

To summarize, the ability of relativistic projectile fragmentation to populate high spin states has been demonstrated by the observation of isomeric states with spin as high as $\frac{35}{2}\hbar$. In addition, the study of the delayed γ-rays associated to the ^{191}W setting products of the ^{208}Pb fragmentation has lead to the identification of new isomeric states in ^{190}W, ^{192,193}Re, ^{195}Os, ^{197,198}Ir and ^{203}Au. In particular, K-isomeric states have been observed in ^{190}W, ^{195}Os and ^{197}Ir for the first time.

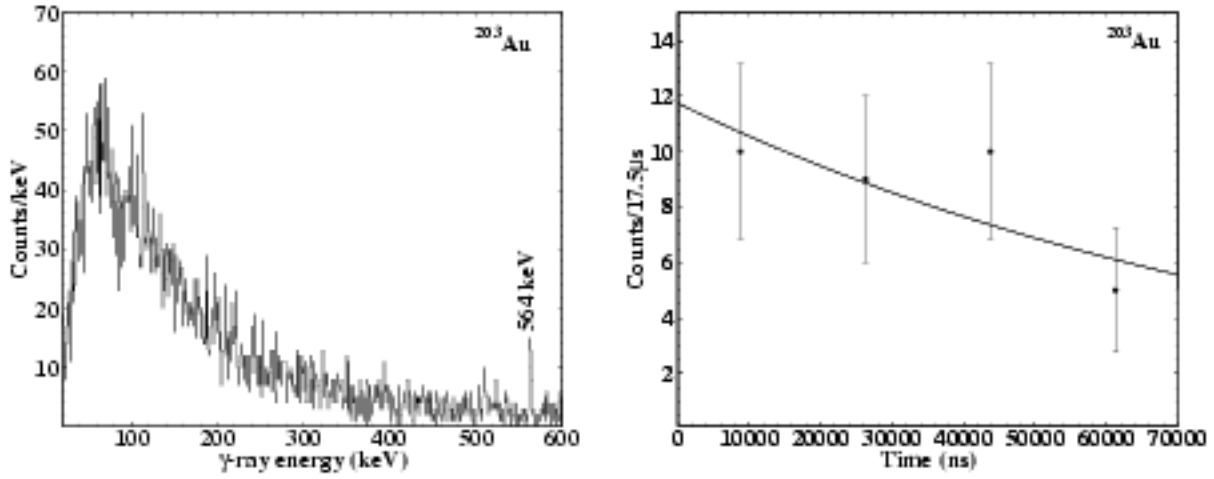

Figure 4.23: Gamma-ray spectrum of ^{203}Au and corresponding decay time spectrum..

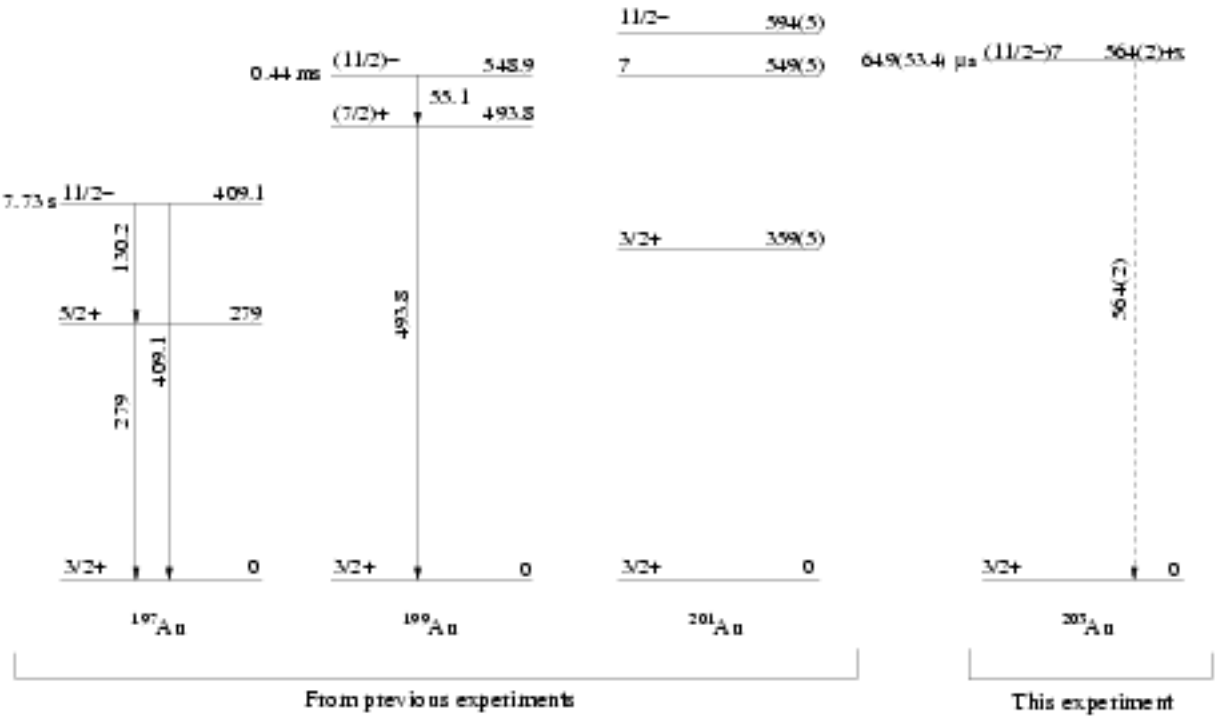

Figure 4.24: Systematics of the level structure from different odd-even Au isotopes leading to the proposed configuration of the isomeric state observed in ^{203}Au during the current experiment.

5 Conclusion (English)

5.1 New method

The work presented here reports about the first experiment using projectile fragmentation to study the nuclear structure of nuclei in the A=180-200 transitional mass region. The ability of this reaction mechanism to populate high spin states has been demonstrated by the successful observation of isomeric states with spin ranging from 5/2 to 35/2 in more than 20 known nuclei and the predictions made by the abrasion-ablation model have been confirmed by the measurements of the corresponding isomeric ratios. Furthermore, new spectroscopic information has been established, namely concerning the existence of numerous isomeric states in the unknown neutron-rich transitional region. The results exposed here thus constitute the first pioneering step in a better knowledge of the nuclear structure of this transitional region.

5.2 Perspectives

The triaxial and oblate shapes in this region are of great interest and the study of odd-A nuclei will be a key element in establishing just what shapes the nuclei are adopting - by pinning down the single-particle orbitals involved, and their rotational properties. Although most of the "exotic" data do not yet answer these questions, they provide an important stepping stone. Having found several isomeric γ-rays, it will be possible to use these with, for example, deep-inelastic reactions, to build up further spectroscopic information. Whenever there is more than one γ-ray in cascade, the transitions can be used as prompt tags, as well as delayed tags, in future experiments. The half-life is such that states above the isomer can be identified, as well as the states above the "ground state".

Furthermore, improving this new technique by using new electronics able to separate

prompt decays from delayed ones, similar experiments can be performed with γ-γ coincidence data giving further information about these nuclei. Thus the successful results of this experiment gave birth to a new project employing the FRagment Separator together with an improved Ge detector array to make new experiments using the fragmentation/fission products as secondary radioactive nuclear beams. This project called RISING (Rare Isotope Spectroscopic INvestigation at GSI) will employ fragmentation/fission products impinging on a target located at the FRS final focal plane to produce very exotic nuclei by different kind of reactions.

6 Conclusion (Français)

6.1 Nouvelle méthode

Le travail présenté ici relate la première expérience utilisant la fragmentation de projectile afin d'étudier la structure nucléaire de noyaux de masse A=180-200. La capacité de ce mécanisme de réaction à peupler des états de haut spin a été démontré grâce à l'observation d'états isomériques de spin variant entre 5/2 et 35/2 dans plus de 20 noyaux connus et les prédictions faites par le modèle d'abrasion-ablation ont été confirmées par la mesure des taux d'isomères correspondants. En outre, de nouvelles informations spectroscopiques ont été établies, notamment concernant l'existence de nombreux états isomériques dans les noyaux riches en neutrons de la région de transition. Les résultats exposés ici constituent ainsi la première étape dans la connaissance de la structure nucléaire de cette région de transition.

6.2 Perspectives

Les formes triaxiales et aplaties ("oblate") attendues dans cette région sont de première importance et l'étude des noyaux de nombre de masse impaire seront un élément clé afin d'établir les formes que les noyaux adoptent - en bloquant les orbitales des particules non appariées - ainsi que leurs propriétés en matière de rotation. Bien que la plupart des données obtenues ici ne répond pas à ces questions, elles fournissent cependant un point de départ. En effet, grâce à la mise en évidence de nombreuses décroissances γ isomériques, il sera possible lors, par exemple, de réactions profondément inélastiques, d'utiliser ces décroissances désormais connues afin d'obtenir de plus amples informations sur le noyau considéré. Lorsque plusieurs décroissances sont observées en cascade, les transitions, tant promptes que retardées, peuvent être utilisées pour signer le noyau lors de futures expériences.

En outre, en améliorant cette nouvelle technique par l'utilisation d'une électronique capable de mieux séparer les décroissances promptes de celles retardées, des expériences similaires peuvent être réalisées dont les données en coïncidence $\gamma - \gamma$ donneront de plus amples informations sur les noyaux considérés. Ainsi les résultats fructueux de cette expérience ont donné naissance à un nouveau projet employant le Séparateur de FRagments en conjonction avec un dispositif de spectroscopie γ amélioré afin de réaliser de nouvelles expériences utilisant les produits de fragmentation/fission comme faisceaux radioactifs secondaires. Ce projet intitulé RISING (pour Rare Isotope Spectroscopic INvestigation at GSI) projettera les produits de fragmentation/fission sur une cible située au plan focal final du FRS afin de produire des noyaux très exotiques par différentes réactions secondaires.

... et facta est lux. (Vulgate, Genèse, Chapitre I, 3)

Bibliography

[1] R.F. Casten, Nuclear Structure from a Simple Perspective (2nd edition), Oxford University Press, Oxford, 2001.

[2] D. L. Hill and J. Wheeler, Phys. Rev. **89** (1953) 1102.

[3] A.S. Davydov and G.F. Filippov, Nuc. Phys. 8 (1958) 237.

[4] S. G. Nilsson, K. Dan. Vidensk. Selsk. Mat. Fys. Medd. **29** (1955) no 16.

[5] O. Haxel, D. Jensen and H.E. Suess, Phys. Rev. **75** (1949) 1766.

[6] J. N. Ginocchio and M. W. Kirson, Phys. Rev. Lett. **44** (1980) 1744.

[7] A. E. Dieperink, O. Scholten and F. Iachello, Phys. Rev. Lett. **44** 1747.

[8] A. Arima and F. Iachello, Ann. Phys. **99** (1976) 253 and 111 (1978) 201 and **123** (1979) 468.

[9] F. Iachello, The Interacting Boson Model, PhD. Thesis, Massachusetts Institute of Technology, Cambridge, 1969.

[10] H. Feshbach and F. Iachello, Phys. Lett. **B45** (1973) 7.

[11] H. Feshbach and F. Iachello, Ann. Phys. **84** (1974) 211.

[12] D. Jansen, R. V. Jolos and F. Dönau, Nucl. Phys. **A224** (1974) 93.

[13] F. Iachello and O. Scholten, Phys. Rev. Lett. **43** (1979) 679.

[14] S Brant, V. Paar and D. Vretenar, Z. Phys. **A319** (1984) 355.

[15] T Hubsch and V. Paar, Z. Phys. **A319** (1984) 111.

[16] J. Cizewski et al., Phys. Rev. Lett. 40 (1978) 167.

[17] P. M. Walker and G. Dracoulis, Nature **399** (1999) 35.

[18] K. Jain et al. Nucl. Phys. **A591** (1995) 61.

[19] J. Pedersen et al., Phys. Scripta **T5** (1983) 162.

[20] P.M. Walker et al., Phys. Rev. Lett. **67** (1991) 433.

[21] C. Wheldon, Ph. D. thesis, University of Surrey, June 1999.

[22] J. Bardeen, L.N. Cooper and J.R. Schrieffer, Phys. Rev. 108 (1957) 1175.

[23] A. Bohr, B.R. Mottelson and D. Pines, Phys. Rev. 110 (1958) 936.

[24] R. D'Alarcao et al. Phys. Rev. **C59** (1999) R1227.

[25] C. Wheldon et al., Phys. Lett. **B425** (1998) 239.

[26] H. Geissel et al., Nucl. Instr. and Meth. **B** 70 (1992) 286.

[27] H. Geissel et al., Nucl. Phys. **A616** (1997) 316c.

[28] J.-J. Gaimard and K.-H. Schmidt, Nucl. Phys. **A531** (1991) 709.

[29] A.S. Goldhaber, Phys. Lett. **B53** (1974) 306.

[30] M. de Jong, Ph. D. thesis, TU Darmstadt (1998).

[31] M. de Jong et al., Nucl. Phys. **A613** (1997) 435.

[32] E. Hanelt et al., GSI Scientific Report 1989, 90-1.

[33] J. Weckenmann et al., GSI Scientific Report 1990, 91-1.

[34] B. Voss et al., Nucl. Instr. and Meth. **A364** (1995) 150.

[35] M. Pfützner et al., Nucl. Instr. and Meth. **B86** (1994) 213.

[36] H. Stelzer, Nucl. Instr. and Meth. **A310** (1991) 103.

[37] J. Kantele, Handbook of nuclear spectrometry, Academic Press, 1995.

[38] J. Gerl, Nucl. Instr. and Meth. **A442** (2000) 238.

[39] CERN Program Library Long Writeup Q121, PAW-Physics Analysis. Workstation, An Introductory Tutorial, CERN, Geneva, Switzerland, 1995.

[40] M. de Jong et al., Nucl. Phys. **A628** (1998) 479.

[41] J. Benlliure et al. Nucl. Phys. **A660** (1999) 87.

[42] C. Chandler et al., Phys. Rev. **C61** (2000) 044309.

[43] R. Grzywacz et al., Phys. Lett. **B355** (1995) 439.

[44] J.-M. Daugas, Ph. D. thesis, Université de Caen (1999).

[45] M. Pfützner et al., Phys. Lett. **B444** (1998) 32.

[46] M. Pfützner et al., submitted to Phys. Rev. C (2001).

[47] N. Iwasa et al., Nucl. Instr. Meth. **B126** (1997) 284.

[48] P.M. Walker et al., Nucl. Phys. **A568** (1994) 397.

[49] Z. Podolyák et al., Phys. Lett. **B491** (2000) 225.

[50] L. Grodzins, Phys. Lett. **2** (1962) 88.

[51] e.g. P. Reiter et al., Phys. Rev. Lett. **82** (1999) 509.

[52] R.B. Firestone, Table of Isotopes, John Wiley & Sons, Inc. (1996).

[53] compiled by B. Singh, Nuc. Data Sheets **61** (1990) 243.

[54] compiled by B. Singh, Nuc. Data Sheets **59** (1990) 133.

[55] compiled by E. Browne and B. Singh, Nuc. Data Sheets **79** (1996) 277.

[56] M. Caamaño, Ph. D. thesis, University of Surrey.

[57] S.M. Yates et al., Phys. Rev. **C37** (1988) 1889.

[58] J.A. Cizewski et al., Phys. Rev. **C27** (1983) 1040.

[59] R.F. Petry et al., Bull. Am. Phys. Soc. 23, No 7, 945, DD7 (1978).

[60] P.M. Walker, private communication.

[61] compiled by C.M. Baglin, Nuc. Data Sheets **84** (19898) 717.

[62] compiled by M.R. Schmorak, Nuc. Data Sheets **53** (1988) 331.

[63] compiled by Z. Chunmei, Nuc. Data Sheets **86** (1999) 645.

[64] compiled by S. Rab, Nuc. Data Sheets 71 (1994) 421.

Abstract

The neutron-rich nuclei of the A$\sim$180-200 transitional region presents many interests for nuclear physicists. In particular, the best examples of K-isomerism, which can be found in the A$\sim$180-200 region, are predicted to occur on the neutron-rich side of the valley of stability and are thus barely populated by standard nuclear reactions. In addition, the γ-decay studies of K-isomers provide critical information about the evolution of the nuclear structure from prolate to spherical shape in the transitional region. Projectile fragmentation has proven to be an efficient method for populating heavy neutron-rich isotopes with cross-sections sufficient to perform γ-ray spectroscopy. Thus, the FRagment Separator (FRS) associated with γ-ray spectroscopy techniques has been successfully used at GSI to search for K-isomers with lifetimes ranging from nano- to milliseconds in the mass region around A$\sim$190-200.

These isomers were produced following the fragmentation of a 1 GeV/nucleon ^{208}Pb beam impinging on a 1.6 g/cm^2 Be target. The fragments were separated by the FRS working in achromatic mode and identified using the Bρ-ΔE-TOF method. Ions were stopped in a 4 mm thick Al catcher covering an implantation area of 3 $\times$ 16 cm^2. Prompt and delayed γ-rays in coincidence with implanted ions of interest were measured using a Segmented Clover Ge Array whose efficiency was about 6% at 1.33 MeV for the central position of the catcher.

Establishing a new experimental technique, this thesis focuses on the observation of several new isomers in neutron-rich A=190-200 nuclei providing the first nuclear structure information from successive γ decay cascades, with special emphasis on ^{190}W and ^{197}Ir new data where K-isomeric states were identified.

Moreover, the ability of this novel method to reach high spin states has been demonstrated by populating K=$\frac{35}{2}^-$ isomeric state in ^{175}Hf, ^{179}W and ^{181}Re. This state corresponds to the highest spin value ever observed in projectile fragmentation.

Résumé

Les noyaux riches en neutrons de la région de transition A$\sim$180-200 présentent de nombreux intérêts pour les physiciens nucléaires. Les meilleurs exemples d'isomérisme K sont prédits pour les noyaux situés du côté riche en neutrons de la vallée de stabilité. Ces noyaux sont par contre difficilement peuplés par des réactions nucléaires classiques. L'étude des décroissances γ de ces isomères K fournit des informations de première importance sur l'évolution de la structure du noyau de la forme prolate à la forme sphérique dans la région de transition. La fragmentation du projectile s'est avérée une méthode puissante pour peupler des isotopes de noyaux lourds riches en neutrons, ceci avec des sections efficaces suffisantes pour pouvoir en faire la spectroscopie γ. Les techniques de spectroscopie γ utilisées auprès du Séparateur de FRagments (FRS) du GSI ont permis d'étudier les états isomériques K de noyaux de la région de masse A$\sim$190-200 dont les temps de vie s'étendent de quelques nanosecondes à quelques millisecondes.

Ces isomères sont produits par fragmentation d'un faisceau de ^{208}Pb à une énergie de 1 GeV/nucléon sur une cible de ^{9}Be d'une épaisseur de 1.6 g/cm^2. Les fragments sont séparés par le FRS fonctionnant en mode achromatique et identifiés grâce à la méthode Bρ-ΔE-TOF. Les ions sont ensuite arrêtés par un stoppeur en aluminium. Les rayonnements γ prompts et retardés émis en coïncidence avec les ions implantés sont détectés par un dispositif composé de 4 détecteurs germanium trèfle segmentés d'efficacité photopic totale 6%.

Utilisant cette nouvelle technique expérimentale, ce travail a permis d'étudier de nouveaux isomères dans les noyaux riches en neutrons de la région de masse A=190-200. De nouveaux états isomériques K ont été identifiés dans les noyaux ^{190}W et ^{197}Ir. L'étude de leur décroissance a permis d'obtenir des informations nouvelles sur leur structure.

Ce travail a aussi démontré l'efficacité de cette nouvelle méthode pour atteindre des états de haut spin : les états isomériques K=35/2$^-$ ont été peuplés dans les noyaux de ^{175}Hf, ^{179}W et ^{181}Re. Les spins de ces états correspondent à la plus haute valeur jamais observée dans des réactions de fragmentation du projectile.